# STUDY OF INCORPORATING CESIUM INTO HEXACYANOFERRATE FRAMEWORK AND DOPED MATERIALS FOR WATER SPLITTING BY DENSITY FUNCTIONAL THEORY CALCULATION

By

XIMENG WANG

A DISSERTATION PRESENTED TO THE GRADUATE SCHOOL
OF THE UNIVERSITY OF FLORIDA IN PARTIAL FULFILLMENT
OF THE REQUIREMENTS FOR THE DEGREE OF
DOCTOR OF PHILOSOPHY

UNIVERSITY OF FLORIDA

2023

To my family and friends

ACKNOWLEDGMENTS

Although it is far from enough to thank the people in an acknowledgement, I would firstly like to take this opportunity to express my heartfelt gratitude to my advisor, Prof. Simon R. Phillpot. He has serious scientific attitude, rigorous academic spirit and broad knowledge which give me extremely strong support during my graduate time. His ideas can always inspire me to solve all kinds of difficulties during graduate study. His great sense of humor always makes me feel relaxed during the busy and hard study hours. He always put student's health into the first priority and helps me get over the badly dark time during COVID pandemic in 2021. His passion for science and life encourages me all the time and will continue to motivate me in future study and work. I couldn't have asked for a better advisor than him.

I would like to thank Dr. Juan C. Nino and Dr. Jonathan R. Scheffe. They are experts in perovskite and pyrochlore materials. Their solid ideas and suggestions helped me to find better candidates for water splitting applications. I would thank Dr. Stephan Lany and Dr. Anuj Goyal for their solid knowledge in density functional theory. Their suggestions always make me think about the physical and chemical meaning behind the calculated data and have a better understanding of the property of materials. Also, I want to thank Elizabeth Gager and Dylan McCord for their active collaboration.

I would also like to thank my committee, Dr. Richard Hennig, Dr. Katerina E. Aifantis. I'm grateful to Dr. Katerina E. Aifantis to teach me much fundamental knowledge about batteries and energy materials and I'm also grateful to Dr. Hennig to teach me machine learning method in computational materials science which are very important for my current and future study in this filed.

I would like to thank the members of the FLAMES group, for their constant support and warm friendship. In particular, I would like to thank Dr. Linyuan Shi for mentoring me when I

joined the FLAMES community. I would like to thank Dr. Shubham Pandey for helping me all the time with VASP and GAUSSIAN bugs and valuable discussion on nuclear waste sequestration project. I would like to thank Dr. Fullarton for her mentoring on charged defect calculations, kindness, caring attitude and delicious cakes. I would like to thank Dr. Eugene Ragasa for interesting discussion on scientific topics and offering his house for Chinese hotpot party. I would thank Dr. An Tien Ta for listening to my ideas all the time and helping me learning many interesting American cultures. I would like to thank Yuan Liu and Seaton Ullberg for valuable discussions on all of my research projects. It's an honor and a luck to work with all of you in the past years.

I would like to thank to my friends, Yuchen Sun, Beining Jin, Yiping Ma, Xiangkai Zeng, Zhou Jiang, Zhilin Jia, Zhongxin Li, Zhan Gao, Chen Liang, Yifei Fu, Ziqi Jia, Yingjingjie, Zeng, Chunfeng Li, Erxuan Xu and Wanying Liu. I would also like to thank my badminton group. I want to say thank you Hangxuan, Binru, Jimmy, Tianyuan, Zihao, Zhongzheng, Jason, Shibo and Kun Shi. I cannot arrive here without your company and support. Thank you for playing with me and recharging me to have more power to work every day.

I would like to thank my girlfriend and soul mate, Qianchen Liu, for her warm support during my Ph.D. study. You have become one of the most important parts of my life. Thank you for sharing, no matter good or bad news, with me and making me happy every second during this journey. My study became much easier because of you.

Finally, I would like to express my thanks to my mom and dad. I can't make it without your selfless support and love. Thank you for respecting my every decision and plan and always giving me a strong foundation to achieve my goals and ambitions. Your constant support is invaluable and precious to me. This dissertation is dedicated to them for their sacrifices.

TABLE OF CONTENTS

page

LIST OF TABLES

LIST OF FIGURES

## LIST OF ABBREVIATIONS

| | |
|---|---|
| AFM | Anti-Ferromagnetism |
| Cu-HCF | Copper Hexacyanoferrate |
| DFT | Density Functional Theory |
| FERE | Fitted Element-Phase Reference Energies |
| FM | Ferromagnetism |
| GGA | Generalized Gradient Approximation |
| MC | Monte Carlo |
| MD | Molecular Dynamics |
| PBE | Perdew-Burke-Ernzerhof |
| PEC | Photoelectrochemical Water Splitting |
| STCH | Solar Thermochemical hydrogen |
| VASP | Vienna ab initio Simulation Package |

Abstract of Dissertation Presented to the Graduate School
of the University of Florida in Partial Fulfillment of the
Requirements for the Degree of Doctor of Philosophy

# STUDY OF INCORPORATING CESIUM INTO HEXACYANOFERRATE FRAMEWORK AND DOPED MATERIALS FOR WATER SPLITTING BY DENSITY FUNCTIONAL THEORY CALCULATION

By

Ximeng Wang

August 2023

Chair: Simon R. Phillpot
Major: Materials Science and Engineering

Copper hexacyanoferrate (Cu-HCF), a Prussian blue analog, has the ability to incorporate $Cs^+$ ions into its structure; it is thus a candidate to selectively extract radioactive $Cs^+$ from water and to sequester it. We use density functional theory calculations to probe the incorporation of $Cs^+$, $K^+$, and $Na^+$ ions into non-hydrated Cu-HCF. Specifically, we determine their incorporation energies, energies for the exchange of alkali ions, lattice stabilities, and the strengths of the bonds between the transition metal and CN ligand. We find that all of these are more favorable for $Cs^+$ than for either $Na^+$ or $K^+$. In addition, we analyze the electronic structure to explain the favorability of $Cs^+$ incorporation. Cu-HCF is found to switch from a ferromagnetic structure to an antiferromagnetic structure as the number of incorporated alkali ions increases.

Hydrated Cu-HCF is also studied. The distribution of zeolitic water molecules (water does not coordinate to any lattice atoms) and coordinated water molecules (water coordinated with lattice Copper) is given by this research. The impact of water molecules on alkali ions incorporation energy and exchange energy are also studied. From this part of research, we determine the maximum number of water molecules is 18. Zeolitic water will first form. When zeolitic water fills the center of the framework, coordinated water starts to form. In addition, the

binding between water and copper ions are weak and similar to the bond strength between water-water binding. Energetic calculation indicates that water molecules lower down the alkali ion incorporation energy but make Cs-Alkali exchange energy higher.

Perovskite materials are good candidates for solar thermochemical water splitting to produce hydrogen gas. Based on the orthorhombic $LaMnO_3$ supercell, we substitute Li Na K Rb Mg Ca Sr Ba on the A-sites (La sites) and Al Ga in Mg Zn on the B-sites (Mn sites) at a concentration of 37.5%. The following criteria are applied to select candidates from all substituted compositions. First, the range of temperature and oxygen partial pressure at which each composition is stable is predicted. For those compositions that are stable in relevant temperature and pressure ranges, the oxygen vacancy formation energies are determined for all of the oxygen vacancy site positions available in the computational supercell. Several candidate compositions are identified using these two filters and are tested by experiments which are found to be of interest.

Pyrochlore compositions ($A_2B_2O_7$) are also screened for water splitting applications. Based on pyrochlore primitive cells, 25% A-sites ions are substituted with Li Na K Rb Mg Ca Sr Ba or In. The same to $LaMnO_3$ study, the same criteria are applied. several pyrochlore candidates for water splitting application are identified.

# CHAPTER 1
# INTRODUCTION

## 1.1 Background and Motivation of Problems

### 1.1.1 Energy Issues Around the World

Fossil fuel resources, including natural gas, oil has been utilized by human beings for more than 100 years and coal (both hard and brown coals), have been utilized for centuries. However, these unsustainable energy resources are incapable of indefinitely meeting the energy demands of our planet. On the one hand, at current production levels, documented reserves of oil, natural gas, and coal will be sufficient for 51, 53, and 153 years of operation, respectively. [1] On the other hand, traditional energy sources have a significant impact on our environment. The extraction, processing, and combustion of fossil fuels, such as coal, oil, and natural gas, result in various environmental consequences:

1. **Air Pollution:** Burning fossil fuels releases pollutants into the atmosphere, including greenhouse gases (such as carbon dioxide and methane) and particulate matter. These emissions contribute to air pollution, smog formation, and respiratory problems.
2. **Climate Change:** Fossil fuel combustion is a major contributor to the increase in greenhouse gas concentrations in the atmosphere. The release of carbon dioxide and other greenhouse gases traps heat, leading to global warming and climate change. This phenomenon has far-reaching consequences, including rising sea levels, extreme weather events, and disruptions to ecosystems.
3. **Water Pollution:** Extracting and processing fossil fuels can lead to water pollution. Spills and leaks from oil and gas drilling, transportation, and storage can contaminate water sources, affecting aquatic ecosystems and posing risks to human health.

4. **Land and Habitat Destruction:** Mining coal and extracting oil and gas often require significant land disruption. This can result in habitat loss, deforestation, and the displacement of wildlife populations. Additionally, infrastructure development, such as pipelines and power plants, can fragment ecosystems and disrupt natural habitats.

5 **Waste Generation:** Traditional energy sources produce waste throughout their life cycles. Coal ash, for example, contains toxic elements and needs proper management to prevent water contamination. Oil spills and leaks from pipelines can have devastating effects on ecosystems and marine life.

Urgent efforts are required to foster the development of new green energy sources. In recent years, significant advancements have been made in various sustainable energy technologies. These include solar power, wind power, geothermal energy, wave energy, biofuels, hydrogen energy, and nuclear energy. Among these, nuclear energy and hydrogen energy stand out as particularly promising options.

### 1.1.2 Nuclear Waste Management

Nuclear power plants produce virtually no direct greenhouse gas emissions during their operation. They do not release carbon dioxide ($CO_2$) or other air pollutants that contribute to climate change and air pollution, unlike fossil fuel-based power plants. Also, nuclear power plants produce negligible quantities of waste compared to other energy sources. [2] However, they produce high-level nuclear waste that has several undesirable characteristics and environmental risks. [2] Some of problematic elements are listed below:

**Strontium-90 (Sr-90):** With a half-life of around 29 years, Sr-90 can accumulate in bones and teeth, posing potential health risks.

**Cesium-137 (Cs-137):** Cs-137 has a half-life of around 30 years and emits highly penetrating gamma radiation. It can contaminate the environment and pose health risks if ingested or inhaled.

**Iodine-129 (I-129):** I-129 has a long half-life of around 15.7 million years and can potentially contaminate water sources, posing risks to human health due to its accumulation in the thyroid gland.

**Technetium-99 (Tc-99):** Tc-99 has a half-life of around 210,000 years and poses challenges for waste management due to its long-lived nature.

**Plutonium-239 (Pu-239):** Pu-239 is a fissile material and has a half-life of around 24,000 years.

**Neptunium-237 (Np-237):** Np-237 has a half-life of around 2.1 million years and is produced as a byproduct of uranium fuel irradiation.

**Americium-241 (Am-241):** Am-241 is produced through the decay of plutonium-241 and has a half-life of around 432 years. It emits alpha particles and poses radiological hazards.

Figure 1-1 [3] shows the activity of high-level waste from one tonne of used nuclear fuel.

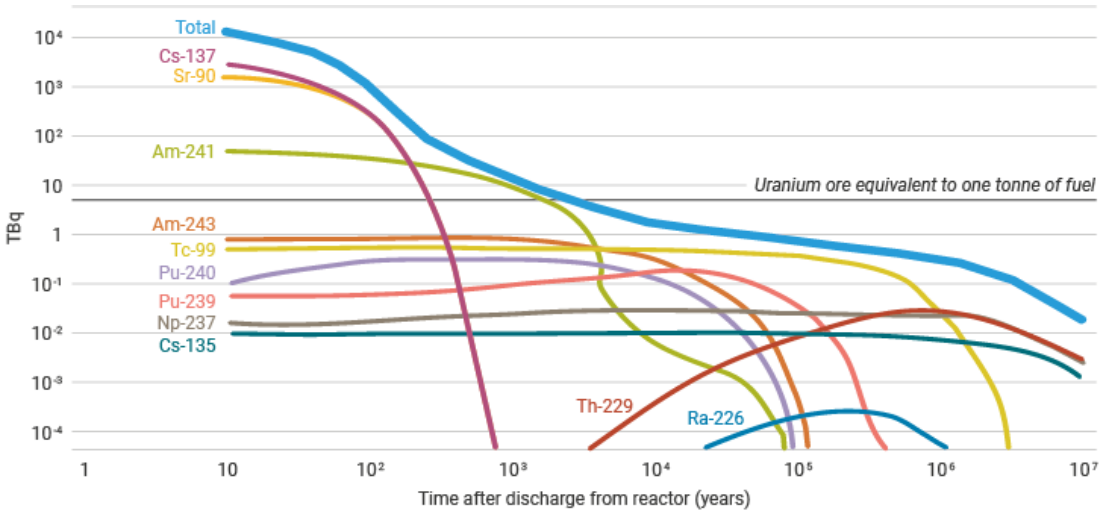


Figure 1-1. Activity of high-level waste from one tonne of used nuclear fuel [3]

We can see from Figure 1-1 that It takes a few thousand years for a ton of fuel to be no more radioactive than a ton of uranium ore. Among the fission products of uranium, cesium

isotopes are among the most abundant. The gamma emitters $^{137}Cs$, with half-lives of 30 years, are the most prevalent. [4–6] On March 11th, 2011, a catastrophic tsunami hit the Fukushima nuclear power plant, resulting in the release of a significant amount of contaminated water containing radioactive cesium-137 ($^{137}Cs$). The extraction of cesium has since become a pressing concern. [7] We focus on radioactive Cs which is one of the most problematic elements of the nuclear cycle. Initially, nuclear waste is often stored in on-site or centralized interim storage facilities. These facilities provide a secure location until a final disposal solution is implemented. Interim storage ensures that waste is kept in controlled environments, preventing potential environmental contamination. Methods and materials are required to prevent Cs from contaminating water environments prior to storage. Experiment has shown that copper hexacyanoferrate (Cu-HCF) can effectively sequester radioactive Cs. [8,9] However, the thermodynamics of this process remain unclear. Therefore, this study aims to provide insights by calculating the $Cs^+$-alkali ion exchange energy, $Cs^+$ incorporation energy, Cu-HCF lattice distortion, bond strength, and electronic structure of Cu-HCF both before and after $Cs^+$ incorporation. These calculations will help explain why $Cs^+$ sequestration is favored by Cu-HCF.

### 1.1.3 New Materials for Water Splitting Application

Hydrogen energy has indeed emerged as an important energy source for human beings. Compared to other fossil energy sources, the combustion of hydrogen gas has a significant advantage: it only produces water vapor ($H_2O$) as a byproduct. This emission of water vapor instead of greenhouse gases contributes to mitigating global warming and reducing the carbon footprint associated with energy production. However, one of the challenges associated with hydrogen as an energy source is that it is not readily available as a primary source. Instead, it needs to be produced using energy from another source and transported for future use. While hydrogen is the third most abundant element in the Earth, it is typically found in compound form,

requiring extraction from other substances through processes such as heating or electrolysis, which often involve the use of electricity and heating. This additional step in the production and distribution of hydrogen adds complexity to its implementation as an energy source. Currently, significant amounts of hydrogen are produced from fossil fuels through processes like steam reforming of natural gas and partial oxidation of coal or heavy hydrocarbons [10]. In the short and medium term, these methods are the most cost-effective and reliable for meeting the demands of large-scale hydrogen production. However, it is clear that relying solely on these methods for hydrogen production are unsustainable in the long run. Therefore, alternative and more sustainable methods need to be developed to ensure efficient production of hydrogen. Water splitting is one method that may be able to achieve sustainable hydrogen production. There are various approaches to water splitting depending on the energy sources used in the process:

**Electrolysis water splitting:** This method uses electricity to split water molecules into hydrogen and oxygen. It can utilize renewable energy sources such as solar or wind power, making it a sustainable option for hydrogen production. Electrolysis can be scaled up or down to meet varying demand for hydrogen, making it suitable for both small-scale and large-scale applications. It offers flexibility in terms of production capacity and can be deployed in diverse locations. Also, electrolysis can be used as a form of energy storage, converting excess electricity generated from intermittent renewable sources into hydrogen. The stored hydrogen can later be used to generate electricity or provide energy in times of high demand. Lastly, electrolysis can produce high-purity hydrogen, suitable for various applications, including fuel cells and industrial processes. However, electrolysis has a number of limitations. First, electrolysis has relatively low energy efficiency compared to other hydrogen production methods; the conversion of electricity into hydrogen involves energy losses during the

electrolysis process. Second, he cost of electrolysis equipment and infrastructure can be high, especially for large-scale production. Third, the scalability of electrolysis systems is currently limited, and the production rate may not match the demands of certain high-volume applications.

**Photoelectrochemical Water Splitting (PEC):** PEC water splitting utilizes sunlight as the energy source, making it a sustainable and renewable method for hydrogen production. It can harness solar energy, which is abundant and widely available. It enables direct conversion of solar energy into hydrogen fuel without the need for external electricity. This eliminates the need for additional energy inputs, reducing overall energy requirements. PEC systems can be scaled up to meet varying hydrogen demands, making them suitable for both small-scale and large-scale applications. The scalability of PEC technology allows for flexible deployment in different settings. However, there are also disadvantages for this methodology. First, current PEC systems face challenges in achieving high energy conversion efficiencies. Factors such as the efficiency of light absorption, charge separation, and catalytic reactions can limit the overall efficiency of the process. Second, PEC devices require specialized materials, such as semiconductors or photoactive materials, which can be costly and challenging to manufacture. The development of efficient and stable materials for PEC applications remains an area of active research. Third, PEC water splitting systems involve multiple components, including light absorbers, catalysts, and membranes. The integration and optimization of these components can be complex, leading to higher system complexity and potential maintenance challenges. Fourth, PEC systems often faces issues related to durability and stability, particularly concerning the materials used and the corrosion of components. Long-term stability and durability of PEC devices need to be addressed for commercial viability. Finally, PEC

water splitting technology can be expensive, mainly due to the specialized materials and manufacturing processes involved. Cost reduction efforts and advancements in materials and manufacturing techniques are necessary to make PEC systems more economically competitive.

**Thermochemical Water Splitting**: This method utilizes heat from sources like nuclear reactors or concentrated solar power to drive chemical reactions that separate water into hydrogen and oxygen. It has the potential for high energy conversion efficiency, especially when coupled with high-temperature heat sources such as concentrated solar power or nuclear reactors. This can result in effective utilization of input energy. TWS can operate continuously, unlike some other hydrogen production methods that rely on intermittent energy sources. This continuous operation allows for consistent hydrogen production to meet demand. It can be compatible with various fuels, including fossil fuels or biomass, depending on the specific thermochemical cycle employed. This flexibility allows for the utilization of different feedstocks for hydrogen production. However, it too has disadvantages. First, thermochemical water splitting involves complex chemical reactions and multiple process steps, which can increase system complexity. This complexity can lead to challenges in system design, integration, and operation. Second, it requires high operating temperatures, which can lead to increased material requirements and corrosion issues. Materials capable of withstanding high temperatures and corrosive environments need to be carefully selected and maintained. Third, thermochemical water splitting is still in the research and development phase, and commercial-scale implementations are relatively limited. Scaling up and commercializing thermochemical processes requires further technological advancements and cost reductions.

In this work, we focus on thermochemical water splitting. The most used methodology is two-step solar thermochemical hydrogen (STCH) water splitting. It can be divided into thermal

reduction steps and oxidation steps. As is shown in Figure 1-2 ($CeO_2$ is shown here as an example) [11], during the reduction process, the material undergoes a reduction reaction, leading to the formation of oxygen vacancies within the material structure. This reduction results in the release of oxygen gas. Conversely, in the oxidation process, the defective material reacts with water molecules, initiating an oxidation reaction that generates hydrogen gas. Equation 1-1 and 1-2 shows the reduction and oxidation process respectively.

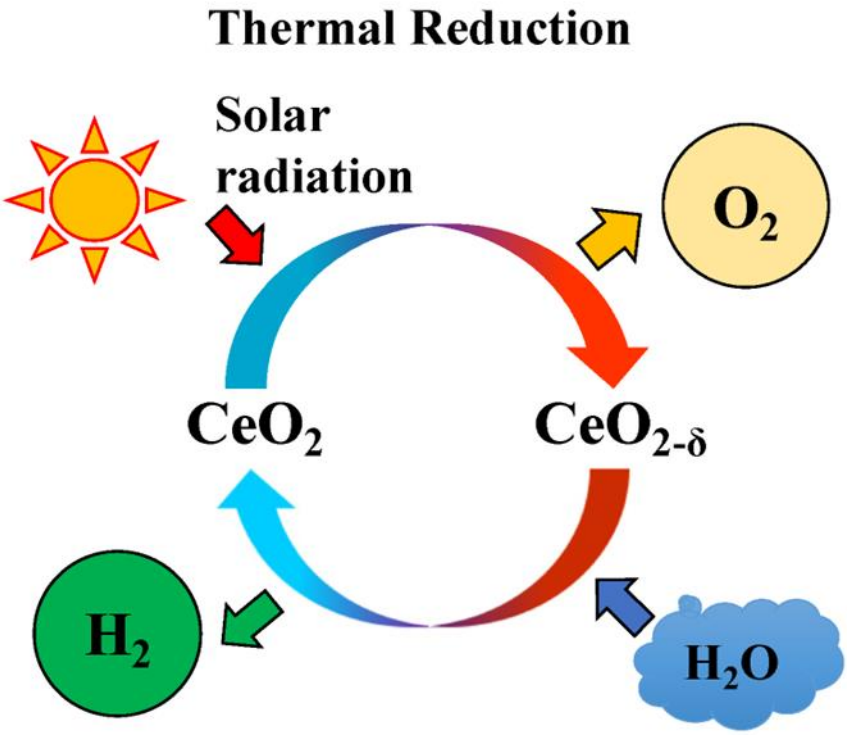


Figure 1-2. Two-step thermal water splitting.

$$CeO_2 \rightarrow CeO_{2-\delta_{red}} + \frac{\delta_{red}}{2} O_2 \quad (1\text{-}1)$$

$$CeO_{2-\delta_{red}} + \delta_{red} H_2O \rightarrow CeO_2 + \delta_{red} H_2 \quad (1\text{-}2)$$

$\delta_{red}$ is the number of oxygen vacancies generated in the thermal reduction process.

Traditionally, $CeO_2$ is used in this process.[11] However, it requires very high reduction temperature, up to 2000 K.[12] Doped perovskite materials have been demonstrated to enhance

the efficiency of hydrogen production in thermal water splitting processes. [12–15]. Additionally, other materials, such as pyrochlore materials, may also be potential candidates for STCH water splitting. In this study, drawing inspiration from doped perovskite materials $La_{0.6}Sr_{0.4}MnO_3$ reported by Scheffe et al. [12], we investigate the suitability of doped $LaMnO_3$ and pyrochlore compositions for water splitting applications. The analysis includes examining the formation energy of oxygen vacancies and evaluating the stability of these doped compositions to identify suitable candidates.

### 1.2 Computational Materials Science

High-performance computing (HPC) has significantly contributed to the advancement of science and technology. Its impact can be observed in various areas. Computational materials science is one of the most rapidly developing and exciting fields in materials science, made possible by the revolutionary advances that have been made in computer processing speed and memory capacity. This emerging field has far-reaching implications and the potential to revolutionize virtually every aspect of materials science and engineering. It provides a framework for understanding the detailed role of individual aspects, such as composition, surface structure and chemistry, microstructure, nature of defects and their distribution in materials synthesis, processing and properties. Different levels of simulation can be applied to address the issues outlined in Figure 1-3. [16] The foundational level is Ab initio modeling, which relies on quantum mechanics. This method operates within length scales of 0.1-10 nm and time scales of 0.1-100 ps. Moving up, we have atomistic scale simulations, which encompass Monte Carlo (MC) and molecular dynamics (MD) methods. These simulations operate within length scales of 1-1000 nm and time scales of 1 ps-10 ns. The subsequent simulation scale is mesoscale methodology, encompassing techniques like phase-field methods and dislocation dynamics. This level operates within length scales of 10 nm–10 μm and time scales of 1 ns–100 ns. We will

apply density functional theory (DFT), one of the most widely used techniques within ab initio modeling for all the simulations from Chapter 3 to Chapter 6.

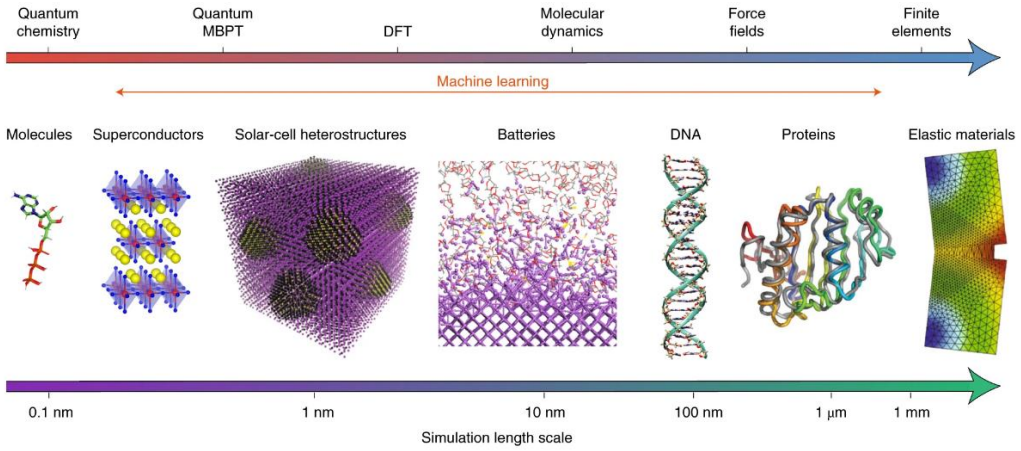


Figure 1-3. Different simulation scales. [16]

# CHAPTER 2
# SIMULATION METHODOLOGY

## 2.1 Density Functional Theory (DFT)

Finding the ground state of a set of atoms is the primary objective when tackling the many-particle problem in solids. In principle, the Schrödinger equation can be employed to solve this problem, considering both the physical structure and electronic structure of the system. The physical structure of a solid refers to its arrangement of atoms in space. It encompasses factors such as crystal symmetry, lattice parameters, and the positions of individual atoms within the crystal lattice. The physical structure plays a vital role in determining the solid's macroscopic properties, including its mechanical, thermal, and optical characteristics. Understanding the physical structure is essential for analyzing how atoms interact with one another in a solid and how these interactions influence its overall behavior. On the other hand, the electronic structure of a solid concerns the arrangement and behavior of electrons within the solid. This includes the distribution of electrons among energy levels or bands and their corresponding momentum states. The electronic structure heavily influences the solid's electrical, magnetic, and optical properties. To determine the electronic structure, one must consider quantum mechanical principles and solve the Schrödinger equation for the many-electron system. The wave function is written below:

$$\widehat{H}\varphi(\{r_i\},\{R_I\}) = E\varphi(\{r_i\},\{R_I\}) \tag{2-1}$$

$$\widehat{H} = \widehat{T} + \widehat{V} \tag{2-2}$$

$$\widehat{T} = -\frac{\hbar}{2m}\sum_{i=1}^{N}\nabla_i^2 \tag{2-3}$$

$$\widehat{V} = \frac{q_i q_j}{|\vec{r_i}-\vec{r_j}|} \tag{2-4}$$

$\{r_i\}$ is the coordinate of the electron i and $\{R_I\}$ is the nuclei positions. $\widehat{H}$ is the

Hamiltonian operator and it consists of kinetic energy operator $\hat{T}$ and Columbic energy operator $\hat{V}$ which is obtained from the Columbic interaction between two charged particles. $m$ is the electron mass, $\hbar$ is Planck constant. The Schrodinger equation can only be solved exactly for a very few problems; in particular, it cannot be solved for systems of more than two particles. Thus, for real materials systems, which contain many nuclei and electrons, approximations are required. The masses of the nuclei are much larger than the electrons so the dynamics of atomic nuclei and electrons can be separated to slow (nuclei) and fast (electron). Based on that, the wavefunction can be decoupled into the wavefunctions of the nuclei $\phi_N$ and the electrons $\phi_e$:

$$\varphi(\{r_i\},\{R_I\}) \rightarrow \varphi_N(\{R_I\}) * \varphi_e(\{r_{i0}\}) \quad (2\text{-}4)$$

This is called the Born-Oppenheimer approximation. From this approximation, we can fix the atomic nuclei and the key problem is to solve the ground state of the electrons by solving the Schrodinger equation for electrons:

$$\hat{H}\varphi(r_1, r_2, r_{3\ldots}r_N) = E\varphi(r_1, r_2, r_{3\ldots}r_N) \quad (2\text{-}5)$$

The Hamiltonian operator consists of three terms: the kinetic energy of the electron (first term), the potential energy for the interaction with another electron (second term) and the potential energy from electron-nuclei interaction (third term):

$$\hat{H} = -\frac{h^2}{2m_e}\sum_i^{N_e}\nabla_i^2 + \sum_i^{N_e} V_{ext}(r_i) + \sum_{i=1}^{N_e}\sum_{j>1} U\,(r_i, r_j) \quad (2\text{-}6)$$

Although the Born-Oppenheimer approximation fixes the nuclei, the system is still large. For example, a simple $CO_2$ molecule will have 22 electrons (6 from C, 8 from each O) and each electron`s position has three spatial coordinates; the final Schrodinger equation is thus a 66-dimensional problem. We can do some approximation to simplify this problem as follows; first define the electron density n(r) to convert the 3N dimension problem to a 3-dimensional problem:

$$n(r) = \varphi^*(r_1, r_2, r_{3\ldots} r_N)\varphi(r_1, r_2, r_{3\ldots} r_N) \quad (2\text{-}7)$$

Then, treat a single electron as a point charge in the field of all the other electrons to simplify the many-electron problem to a many-single electron problem

$$\varphi(r_1, r_2, r_{3\ldots} r_N) = \varphi_1(r_1) * \varphi_2(r_2) * \varphi_3(r_3) * \ldots * \varphi_N(r_N) \quad (2\text{-}8)$$

The electron density can be defined in terms of individual wavefunctions:

$$n(r) = 2\sum_i \varphi_i^*(r) * \varphi_i(r) \quad (2\text{-}9)$$

According to the Hohenberg-Kohn theorem [17], the ground state energy E is a unique function of the electron density:

$$E = E[n(r)] \quad (2\text{-}10)$$

And the electron density that minimizes the energy of the function is the true ground state electron density:

$$E[n(r)] > E_0[n_0(r)] \quad (2\text{-}11)$$

Based on the above theorems, the energy functional can be written as:

$$E[n(r)] = T_0[n(r)] + E_c[n(r)] + E_{ext}[n(r)] + E_{xc}n(r) \quad (2\text{-}12)$$

$T_0[n(r)]$ is the kinetic energy term, $E_c[n(r)]$ is the Coulombic energy term due to mutual electron Coulombic interaction, $E_{ext}[n(r)]$ is the energy term of ionic interactions between electrons and nuclei and $E_{xc}n(r)$ is the many body exchange-correlation energy term. The first three terms can be computed exactly. However, the $E_{xc}n(r)$ term can only be approximated. In DFT, the hierarchy of functionals refers to the different levels or approximations used to describe the exchange-correlation energy, a key component of the total energy of a system. The exchange-correlation energy accounts for the quantum-mechanical effects arising from the interactions between electrons. The hierarchy of functionals can be categorized into different levels of sophistication and accuracy. At the lowest level, we have the local density approximation (LDA),

which assumes that the exchange-correlation energy depends only on the local electron density at each point in space. The LDA provides a simple and computationally efficient approximation but may not accurately capture the spatial variations in the electron density. Moving up the hierarchy, we have the generalized gradient approximation (GGA). The GGA takes into account not only the local electron density but also its spatial gradient, leading to improved accuracy in describing systems with varying electron densities. GGAs provide a more accurate description of molecular systems and bulk properties than the LDA. Beyond GGAs, there are higher-level approximations known as meta-GGAs, hybrid functionals, and range-separated functionals. Meta-GGAs go beyond the local electron density and its gradient, incorporating additional information such as the kinetic energy density or Laplacian of the density. Hybrid functionals combine a fraction of exact exchange (derived from Hartree-Fock theory, a wave function based method) with a GGA or meta-GGA, providing better accuracy for a wide range of systems. Range-separated functionals split the exchange-correlation energy into short-range and long-range components, treating them separately and improving the description of different types of interactions. Each level of the hierarchy offers a trade-off between accuracy and computational cost. Higher-level functionals tend to provide better accuracy but are computationally more demanding. Therefore, the choice of functional depends on the specific system being studied and the computational resources available. The DFT method with GGA-PBE (Perdew-Burke-Ernzerhof) level is used in all the simulations from Chapter 3 to Chapter 6. Vienna ab initio Simulation Package (VASP) is applied. [18,19]

### 2.2 Fitted Elemental-Phase Reference Energies (FERE) Method

Despite the considerable success of theoretical approaches based on density functional theory in describing the properties of solid compounds, accurately predicting the enthalpy of formation for insulating and semiconducting solids continues to be a challenging task. [20,21] This

difficulty primarily stems from the incomplete error cancellation that occurs when calculating the total energy differences between the compound's total energy and the total energies of its elemental constituents.[22] The concept of FERE method is to increase that error cancellation to get more accurate enthalpy of formation value than the traditional method. To use the FERE method, we should firstly fit the FERE chemical potentials for the elemental constituents. The FERE chemical potentials are obtained by Equation 2-13 which is by solving the linear least-squares problem.

$$\Delta H_f{}^{exp}\left(A_{n_1}B_{n_2}\ldots\right) = E_{total}^{GGA+U}\left(A_{n_1}B_{n_2}\ldots\right)\text{-}\sum_i n_i\mu_i^{FERE} \quad (2\text{-}13)$$

$\Delta H_f{}^{exp}\left(A_{n_1}B_{n_2}\ldots\right)$ is the experimental enthalpy of formation. For the elemental-phase energies $\mu_i^{FERE}$ that optimally cancel total-energy errors with the compound energies $E_{total}^{GGA+U}$, which are computed using the experimental crystal structures with GGA+U optimized lattice vectors and atomic positions. The U-J values are 3 eV for all the transition metals except for Cu and Ag which have U-J=5 eV. The FERE energies can be expressed as an energy shift $\delta\mu_i^{FERE}$ compared to DFT calculated elemental total energies $\mu_i^{GGA+U}$ as it is shown in Equation 2-14:

$$\mu_i^{FERE} = \mu_i^{GGA+U} + \delta\mu_i^{FERE} \quad (2\text{-}14)$$

Then, the enthalpy of formation of a compound $A_{n_1}B_{n_2}$ ... can be calculated by FERE method as it is shown in Equation 2-15:

$$\Delta H_f{}^{FERE}\left(A_{n_1}B_{n_2}\ldots\right) = \Delta H_f^{GGA+U}\left(A_{n_1}B_{n_2}\ldots\right)\text{-}\sum_i n_i\delta\mu_i^{FERE} \quad (2\text{-}15)$$

From Equation 2-15 we can know that $\delta\mu_i^{FERE}$ is not expected to improve the accuracy of absolute total energies for the elemental phases. It optimizes the systematic error cancellation with the total energies of the compounds. The FERE method is used for stability analysis in Chapter 5 and Chapter 6.

## 2.3 PYLADA DEFECT

PYLADA DEFECT is a PYTHON based DFT calculation package to perform defects formation energy calculation in target materials, the workflow can be shown in Figure 2-1[23]: Figure 2-1 (a) shows the workflow to perform defect calculations, and Figure 2-1 (b) shows the Voronoi tessellation-based algorithm to find interstitial sites in a given structure (example shown: ZnO)

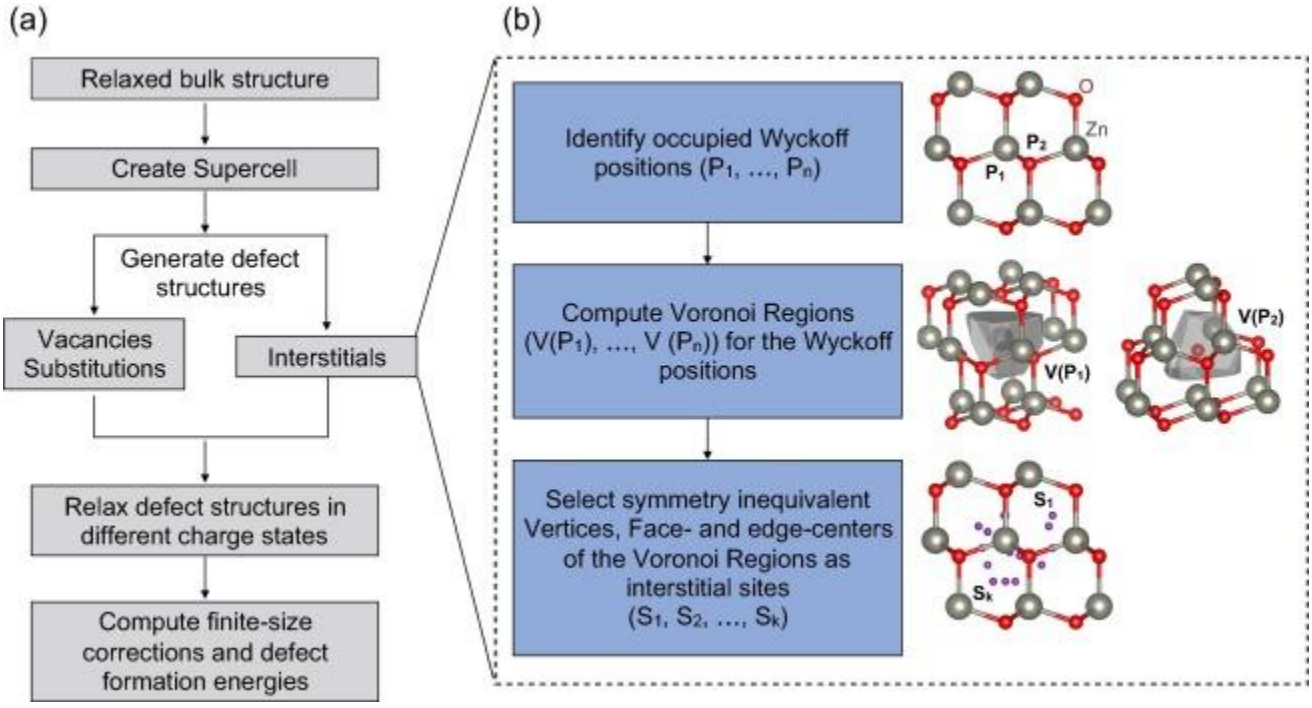


Figure. 2-1 Workflow of PYLADA DEFECT.[23]

The vacancy formation energy calculations involve several steps in the PYLADA DEFECT package. Firstly, a volume relaxation is performed on the target structures. Subsequently, supercells are generated based on the relaxed target structures. These supercells are used to identify different vacancy sites, taking into account the structural symmetry. Once the vacancy sites are identified, vacancies are created at those specific sites. To ensure accurate representation of non-symmetric defect configurations, the first nearest-neighbor atoms to the

vacancy are randomly displaced by 0.1Å. This displacement breaks the underlying site symmetry, effectively capturing the non-symmetric nature of the defects. The PYLADA DEFECT package is employed for calculating the formation energy of oxygen vacancies. This methodology is utilized in both Chapter 5 and Chapter 6 of the research work.

# CHAPTER 3
# INCORPORATION OF RADIOACTIVE CESIUM INTO COPPER HEXACYANOFERRATE BY DENSITY FUNCTIONAL THEORY CALCULATIONS*

## 3.1 Background

Sequestering Cs isotopes is a significant challenge, particularly because Cs is an alkali metal like Na, and thus often water soluble. Hierarchical materials have recently gained attention as potential waste forms. Figure 3-1 shows the different types of hierarchical structures. [24] A hierarchical structure can be defined as a material that encompasses structural motifs at different length scales, which collectively contribute to the formation of a larger and cohesive structure or framework. This definition highlights the practicality and simplicity of understanding hierarchical structures.[25] As one of the hierarchical materials, metal hexacyanoferrates (Metal-HCFs), of which the best known is Prussian Blue, have been shown to be effective $Cs^+$ sorbents. [26–30] These Prussian Blue Analogs (PBAs) have a crystalline structure with well-defined nanopores, which can selectively trap Cs ions, even in the presence of high c of concentrations of competing ions. [7] Among all the PBAs, Cu-HCF is a particularly promising candidate due to its high selectivity towards $Cs^+$. [31–36]

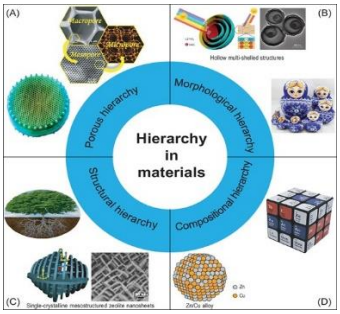


Figure 3-1. The classifications of hierarchy in materials and the representative natural and synthetic materials. [24]

* The work described in this chapter has been published in Wang, X.; Pandey, S.; Fullarton, M.; Phillpot, S. R. Study of Incorporating Cesium into Copper Hexacyanoferrate by Density Functional Theory Calculations. The Journal of Physical Chemistry C 2021, 125 (43), 24273–24283. https://doi.org/10.1021/acs.jpcc.1c08702.

In this chapter, we use density functional theory calculations to characterize the lattice distortion, incorporation energy, ion exchange energy and electronic structure of perfect and defected Cu-HCF when $Cs^+$, $Na^+$, and $K^+$, are inserted into the structure. The results indicate that the incorporation of Cs+ is energetically favored over the incorporation of $Na^+$ or $K^+$. The reasons for this preference are identified. This energy preference opens the possibility of utilizing ion exchange processes to effectively sequester $Cs^+$ in Cu-HCF.

## 3.2 Structures and Computational Setups

### 3.2.1 Structure of Copper Hexacyanoferrate

Copper hexacyanoferrate, $CuFe(CN)_6$, has an FCC structure with a space group of $Fm\bar{3}m$. The conventional unit cell shown in Fig. 3-2 left contains four formula units, with the Cu atom (blue) at (0,0,0) and an Fe atom (brown) at (0,0,1/2). A CN ligand lies between them, with the Cu coordinating with the N side and the Fe coordinating with the C side. While Fe(III) does not have any electrons in $e_g$ orbitals, Cu(II) does have electrons in $e_g$ orbitals when they form the Cu-HCF framework. This means that the Fe coordinates with C in this structure are in a strong crystal field with a low spin state (LS) [37]. In contrast, the Cu coordinates with N in a weak crystal field with a high spin state (HS). The left side of the Figure 3-2 shows the perfect structure of Cu-HCF and the right side shows the defected structure. Blue: copper, brown: iron; white: nitrogen; black: carbon.

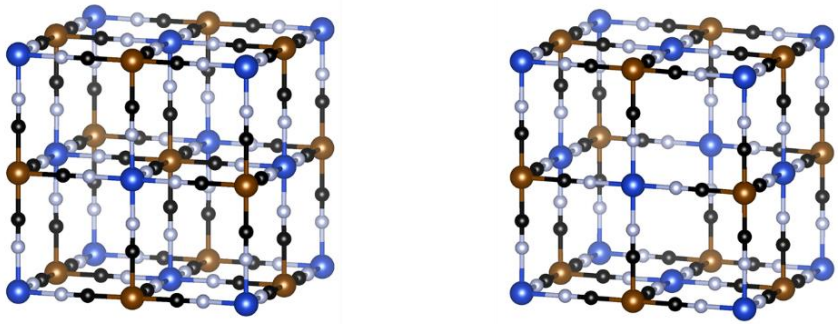

Figure 3-2. Cu-HCF conventional unit cell of perfect structure and defected structure

Cu-HCF is commonly synthesized with a defected structure in which an iron cyanide, $Fe(CN)_6$, vacancy is present at the center of the unit cell, as depicted in the right image of Fig 3-2 [38–40]. Alkali ions can be incorporated into both the ideal and defected structures. As multivalent transition metals, the oxidation states of Cu and Fe can change as various numbers of alkali ions are incorporated.

Neither the perfect nor defected structures of Cu-HCF is charge-neutral, even if Fe and Cu ions are in their highest oxidation state: +3 and +2, respectively. When alkali atoms are added to the structure, the valence of Cu and Fe ions changes to maintain a charge-neutral environment. Tables 1-1 illustrate the oxidation states of Fe and Cu as well as the overall charge of the structure as the number of alkali ions increases from 0 to 8 in both the perfect (upper) and defected (lower) structures. Magnetic moment analysis supports these oxidation state assignments.

Table 3-1. Oxidation states (OS) of Cu and Fe ions and charge state of perfect Cu-HCF structure and defected Cu-HCF

| **#of alkali atoms** | **0** | **1** | **2** | **3** | **4** | **5** | **6** | **7** | **8** |
|---|---|---|---|---|---|---|---|---|---|
| OS of Cu ions | +2 | +2 | +2 | +2 | +2 | +2 | +2 | +2 | +2 |
| OS of Fe ions | +3 | +3 | +3 | +3 | +3 | +3, +2 | +3, +2 | +3, +2 | +2 |
| total charge | −4 | −3 | −2 | −1 | 0 | 0 | 0 | 0 | 0 |

| **#of alkali atoms** | **0** | **1** | **2** | **3** | **4** | **5** | **6** | **7** | **8** |
|---|---|---|---|---|---|---|---|---|---|
| OS of Cu ions | +2 | +2 | +2 | +2 | +2 | +2, +1 | +2, +1 | +2, +1 | +1 |
| OS of Fe ions | +3 | +3, +2 | +3, +2 | +3, +2 | +2 | +2 | +2 | +2 | +2 |
| total charge | −1 | 0 | 0 | 0 | 0 | 0 | 0 | 0 | 0 |

### 3.2.2 Density Functional Theory Calculations

The lattice stabilities, alkali ion incorporating energies, alkali ion exchange energies and bond strengths are calculated using density functional theory (DFT) in the VASP [18,19] with projector augmented waves (PAW) pseudopotentials [41,42]. The electrons considered are Cu

$^{3}d^{10}4s^{1}$, Fe $3d^{6}4s^{2}$, C $2s^{2}2p^{2}$, N $2s^{2}2p^{3}$, Cs $5s^{2}5p^{6}$ $6s^{1}$, K $3p^{6}4s^{1}$, and Na $3s^{1}$; that is 11, 8, 4, 5, 9, 7 and 1 electrons respectively. The generalized gradient approximation (GGA) is chosen to approximate the exchange-correlation energy with the Perdew-Burke-Ernzerhoff (PBE) functional [43,44]. The GGA+U method is applied to deal with the localization of d-electrons in the transition metals. U-J values of 1 eV for Fe and 3 eV for Cu, are used, which, are the same as used by Targholi et al. [44]for the same chemical composition. The cutoff energy is set to be 500 eV for all calculations. A 4 x 4 x 4 Monkhorst-Pack k-point mesh is used for structural relaxation and a 6 x 6 x 6 mesh for the density of states (DOS) calculations. [44] Spin polarizations are also applied to all of the calculations below. As mentioned above, for the empty Cu-HCF framework, neither the perfect nor defected structure is charge neutral even if Fe and Cu ions are in the highest oxidation state. However, Cu-HCF is a metal, as has been confirmed by previous calculations; [44] the appropriate treatment of such systems is well established and implemented in VASP by the addition of a compensating background charge so as to make the overall system charge neutral.

### 3.2.3 Alkali Ion Incorporating Energy

Efficient extraction of cesium from solution requires the incorporation process into Cu-HCF to be thermodynamically favorable, while kinetic factors may also play a crucial role. The previous research shows the kinetic barrier for K diffusion in Cu-HCF structure is just 1.0 eV [44]. Therefore, we are not worried about kinetic favorability of alkali ions. We will focus on thermodynamic favorability calculations of alkali ions in perfect and defected Cu-HCF frameworks. In this context, we have determined the incorporation energy of Cs+ in Cu-HCF and examined the effects of concentration. Specifically, we incorporated 1, 2, 3, 4, and 8 Cs+ ions into a single Cu-HCF unit cell and calculated the incorporation energies, which are normalized to the value for one added atom.

The incorporation energy is:

$$E_{incorporation} = \left(\frac{1}{N}\right)\{E_f(N) - E_0 - NE_{ref(A)}\} \quad (3\text{-}1)$$

$E_f(N)$ is the energy of structure after insertion of the N alkali ions, A=$Cs^+$, $K^+$ or $Na^+$; $E_0$ is the energy of Cu-HCF without any alkali atoms. The alkali atom(s) are inserted at 8c sites, as shown in Figure 3-3 ($K^+$ :purple; $Cs^+$: green);

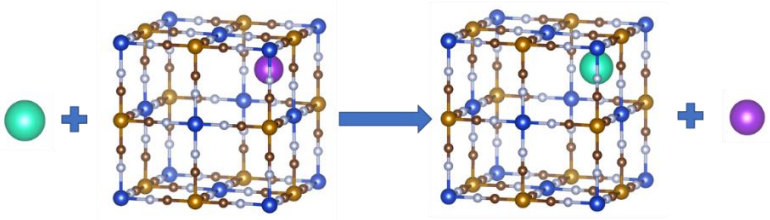

Figure 3-3. Ion exchange of $K^+$ for $Cs^+$ in the defected lattice.

the structure and energy are then allowed to equilibrate. $E_{ref}$ is the reference energy for the alkali atoms. The values for $Cs^+$ ions are compared with the corresponding values for $K^+$ and $Na^+$ calculated in the same way. For the physically realistic scenario of the alkali atom being in a hydrated environment, the reference states of alkali ions will be the difference in the energy of a "droplet" of n water molecules containing an alkali ion and a water droplet without an alkali atom:

$$E_{ref(A)} = \{[A(H_2O)_n]^+ - \mathrm{E}(n_{H_2O})\}. \quad (3\text{-}2)$$

For n=0, this would simply correspond to the energy of a single alkali ion in vacuum. Mähler and Persson showed that the number of nearest neighbor coordinating water molecules for $Cs^+$ is in the range 6 to 9; $K^+$ and $Na^+$ are smaller ions, so have 4 to 6 and 4 to 8 nearest neighbor coordinating water molecules, respectively. [45] We calculate the n-dependence (number of water molecules) of the water-alkali binding energy as a function of the number of water molecules, n, for all three alkali ions, comparing our results with previous studies where available. This approach to construct ion-water complex was used by Pandey et al. to study hydrated ions; [46] the details are provided in the

Section 3.3.2. Water may also be incorporated into the Cu-HCF structure to form a Cu-HCF-water hydrated structure. The effects of hydration is the subject of the Chapter 4.

### 3.2.4 Alkali Ion Exchange Energy

To determine the energetics of ion exchange in Cu-HCF, we analyze the change in energy when a $K^+$ or Na+ ion in the 8c body center of the structure is replaced by $Cs^+$. Figure 3-3 depicts this process. The alkali atom that is not in the Cu-HCF is hydrated. The energy for exchanging N K+ or Na+ ions with N Cs+ ions is then calculated as: [46]

$$E_{exchange}(N) = \left(E_{Cs}(N) - E_{K/Na}(N)\right) - N(E_{ref(Cs)} - E_{ref(K/Na)}) \quad (3\text{-}3)$$

$E_{Cs}(N)$ is the energy of the lattice with N $Cs^+$ ions; $E_{K/Na}(N)$ is the energy of the lattice with N $K^+$ or $Na^+$ ions; $E_{ref(Cs)}$, $E_{ref(K)}$ are the reference energies for $Cs^+$ and $K^+$ hydrated with n water molecules, respectively, as described above. The calculations are conducted for both perfect and defected structures of Cu-HCF. The ion exchange energy is calculated for 1, 4, and 8 Cs+ ions exchanging K+ or Na+, with the results normalized to the exchange of one ion.

### 3.2.5 Lattice Distortion of Incorporated Cu-HCF

The 8c sites of Cu-HCF have a radius of about 1.6 Å [47], which is larger than that of Na+ and K+ but very close to that of Cs+, as compared with the ionic radius of alkali ions [48]. In defected Cu-HCF, a large number of $Fe(CN)_6$ vacancies in the lattice create a region at the center of the unit cells with a diameter of ~5 Å (i.e., radius ~2.5 Å) [47]. This large open region tends to destabilize the framework and could even cause the entire structure to collapse during ion incorporation. We calculate the lattice parameters and unit cell angles in both perfect and defected structures with Na+, K+, and Cs+ ions inserted. As Na+ ions are small, we also consider their insertion into the smaller 24d site, which lies at <0.25, 0.25, 0>. The number of alkali ions in the structure is set to 1, 2, 3, 4, and 8.

### 3.2.6 Bonding Strength

To investigate the effect of Cs+ ions on bond strength in the Cu-HCF structure, charge density difference plots will be generated for both the perfect and defected structures. To generate the plot, the overall charge density of the structure is used to substrate the charge density of the constitute ions. We can read the charge density between different ions and know whether there is a charge accumulation or depletion between different ions. These plots will reveal changes in the charge density in the bonds between the transition metal ions and the cyanide ligand. An increase in charge density indicates stronger bonding. It is reasonable to expect that $Cs^+$ ions, being another alkali metal, will have a similar effect on bond strength as K+ ions, which were previously found to increase orbital overlap between metal and cyanide groups in Cu-HCF [44].

### 3.2.7 Electronic Structures

As the Cs+ sequestration process takes place, the electronic structure will undergo changes that reflect the alterations in bonding and magnetic properties. In order to investigate these changes, the density of states will be calculated for both the perfect and defected structures. Particular emphasis will be placed on analyzing alterations in the electronic structure and magnetic moment that arise as a result of the incorporation of alkali atoms.

### 3.2.8 Alkali Ion Sites

All the calculations presented above require alkali ions to be incorporated into the Cu-HCF structures. It is important to determine where they are located within the framework. For larger alkali ions, such as Cs and K, they are inserted into the 8c sites. For smaller Na ions, we follow Ling et al. [49] by also considering the 24d sites, which lie at (0.25, 0.25, 0). After careful calculations, we found that all three alkali ions occupy the 8c sites. The details will be discussed in Section 3.3.5. The Cu-HCF unit cell contains eight 8c sites, meaning there are different possible arrangements for the incorporation of more than one alkali ion. We have determined the energetics of various

configurations, as discussed in the Section 3.3.5, and found that the incorporation energies are essentially independent of the relative positions of the alkali ions in the unit cell.

## 3.3 Results and Discussions

### 3.3.1 Preliminary Calculations

The calculated lattice parameter of the perfect Cu-HCF framework is found to be 10.11Å, which is in agreement with the experimental value of 10.10Å [50]. Electronic structure calculations show that there is no band gap, indicating that Cu-HCF is a metal, consistent with previous calculations [51]. The enthalpy of formation $\Delta H_f$ for both the perfect and defected structures is calculated using the following equation:

$$\Delta H_f(A_{n_1}B_{n_2}\dots) = E_{total}^{GGA+U}(A_{n_1}B_{n_2}\dots) - \sum_i n_i\mu_i \quad (3\text{-}4)$$

$E_{total}^{GGA+U}(A_{n_1}B_{n_2}\dots)$ is the total energy of a compound $A_{n_1}B_{n_2}\dots$ given by DFT+U. $n_i$ is the elemental composition in the compound. $\mu_i$ is the chemical potential of the elemental phase in compound. We can get the $\mu_i$ value from the previous literature. [22] The calculation results give -0.48 eV/atom for perfect Cu-HCF and -0.41 eV/atom for defected Cu-HCF. It indicates that the empty perfect structure is slightly energetically favorable than the empty defected structure.

### 3.3.2 Hydration of Alkali Ions

The alkali ions that are incorporated into Cu-HCF come from aqueous solutions. To capture this, in our simulation the alkali ions are surrounded by water molecules. As illustrated by Figure 3-4 upper, we add n water molecules (n =1 to 10) around the alkali ion and then do a full structural relaxation of this complex. The water-alkali binding energy which indicates the energy change during alkali ion hydration process is also calculated with the following equation:

$$E_{binding} = E_{A^+} + nE_{H_2O} - E_{[A(H_2O)_n]^+} \quad (3\text{-}5)$$

$E_{A^+}$ is the energy of alkali ions, $nE_{H_2O}$ is the total energy of water molecules in hydrated system and $E_{[A(H_2O)_n]^+}$ is the energy of water alkali ion complex.

Figure 3-4 lower left shows the binding energy increasing with the number of hydrated water molecules. This is clearer in Figure 3-4 lower right, which shows that the binding energy per water molecule becomes more negative up to 5 or 6 water molecules, after which it is essentially constant. This corresponds to the completion of the first hydration shell around the ion. These findings are in good agreement with the suggested number of coordinated water molecules in the previous study. [45] Next, we determine the binding energy of a droplet of n water molecules droplet, $E_{binding}(n)$, defined as:

$$E_{binding}(n) = E_{droplet}(n) - nE_{H_2O} \quad (3\text{-}6)$$

Where $E_{droplet}(n)$ is the energy of a water droplet contains n water molecules and $nE_{H_2O}$ is the total energy of n isolated water molecules. As Figure 3-5 shows, this energy difference, the binding energy of the droplet, increases approximately linearly with the increasing number of water molecules. The average normalized water-water binding energy is about 0.40 eV which is very close to experimental water vaporization enthalpy. (0.42 eV) [52] This binding between water molecules is also present in the alkali ion-water complex which accounts for its use in calculating the incorporation energy.

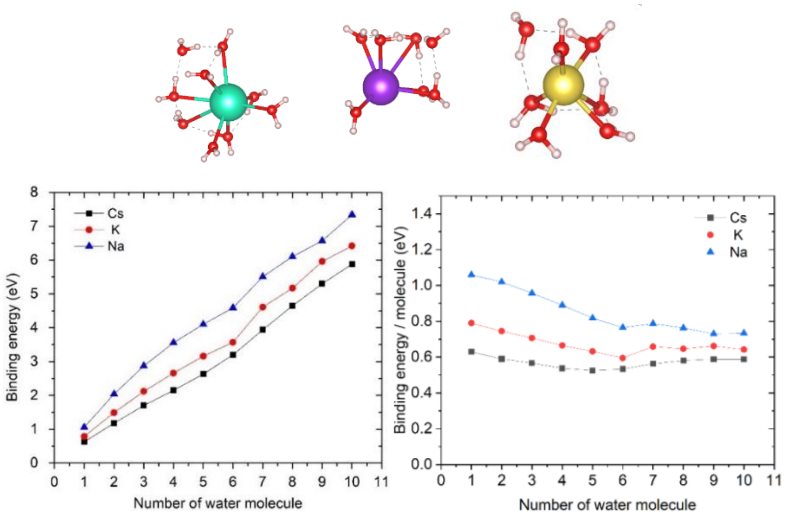


Figure 3-4. Optimized $[A(H_2O)_n]^+$ complex, Water-alkali binding energy as a function of number of hydrated water molecules and binding energy per water molecule.

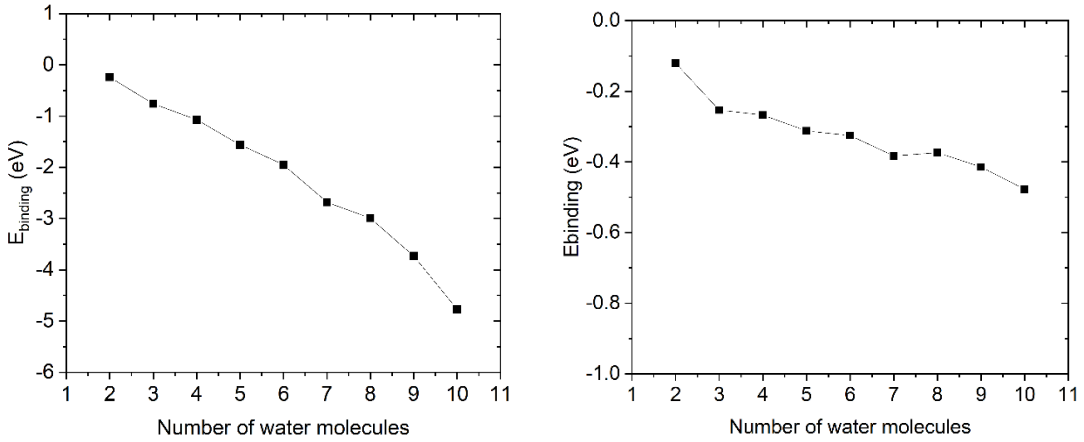


(a) (b)

Figure 3-5. Binding energy of water molecules in a droplet of n number of water molecules and binding energy of water normalized in one water molecule.

### 3.3.3 Alkali Ion Incorporation Energy

The Figure 3-6 shows the incorporation energies of Cs+, K+, and Na+ in both perfect and defected structures as a function of the number of water molecules in the droplet. Figure 3-6 (a) shows the incorporation energy of Na+, K+ and Cs+ in perfect structures; Figure 3-6 (b) shows the incorporation energy of Na+, K+ and Cs+ ions in the defected structures. The dotted lines are averages over n=3 to n=10. As previously mentioned, these results are for the high concentration limit, where the dimensions and shape of the Cu-HCF optimize to reach zero stress.

Figures 3-6 (a) and (b) illustrate the incorporation energy of 1, 4, and 8 alkali ions into both perfect and defected Cu-HCF structures, as a function of the number of water molecules in the droplet used to extract the alkali ion. All values are negative, indicating that it is energetically favorable for the alkali ion to be incorporated into the Cu-HCF structure. The incorporation energies remain nearly constant for three or more water molecules, and the average incorporation energies are indicated by dashed lines. For the incorporation of a single alkali ion, K+ has the most favorable incorporation energy, while Na+ has the least favorable. However, the K+ incorporation energy is almost independent of the number of ions, whereas the incorporation energy for Na+ becomes less

negative and the incorporation energy for Cs+ becomes more negative as the number of ions increases. Therefore, for the incorporation of 4 and 8 ions, Cs+ is the most energetically favorable. The trend in the defected structure is similar to that of the perfect structure. In all cases, Cs+ is weakly favored over K+, which is in turn weakly favored over Na+. The favorable incorporation of Cs+ is likely due to the stronger bonding between the more electropositive Cs+ ions and the Cu-HCF structure, as well as the near-perfect fit of the Cs+ ions into the 8c sites. These factors will be explored in more detail below.

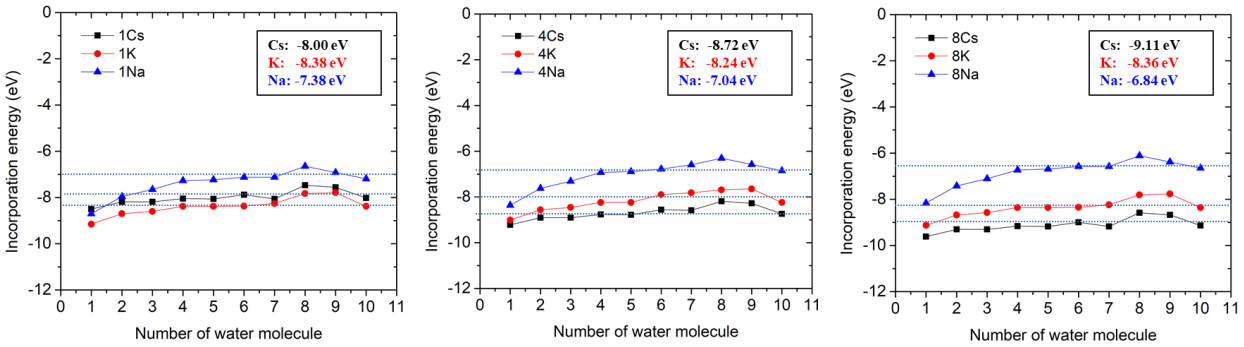


(a)

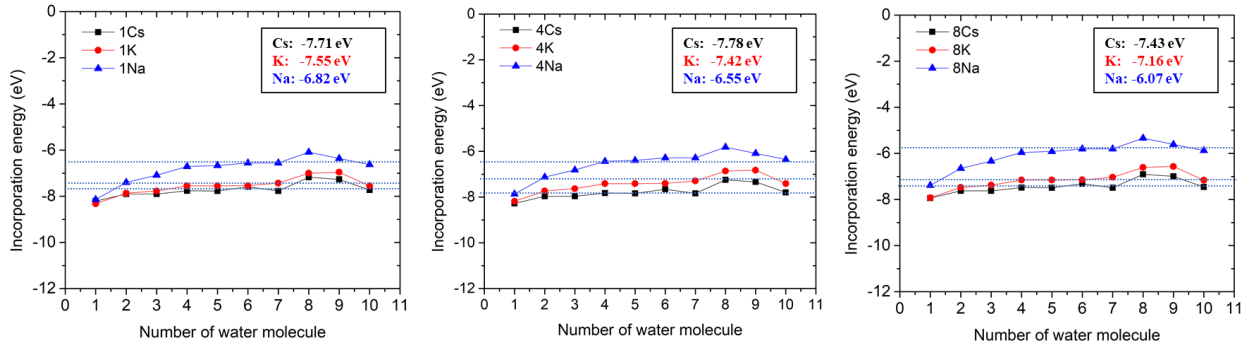


(b)

Figure 3-6. Incorporation energies of 1, 4 and 8 alkali ions as a function of the number of water molecules, n, hydrating water molecules in both perfect and defected structures.

### 3.3.4 Alkali Ion Exchange Energy

The exchange energy for replacing Na+ and K+ with Cs+ is computed using Equation 3-3 for 1, 4, and 8 Cs+ ions, which is simply the difference between the energies for the various alkali ions

shown in Figure 3-7. Figure 3-7 (a) displays the ion exchange energy for Cs+ replacing K+ and Na+ in the perfect structure as a function of the number of water molecules in the droplet. Negative values indicate that it is energetically favorable to replace K+ or Na+ with Cs+. Both in the perfect and defected structures, the ion exchange energy slightly decreases with an increasing number of hydrating water molecules, and eventually reaches convergence for 1, 4, and 8 water molecules. The exchange of Na+ by Cs+ is strongly energetically favorable in both cases, while the exchange of K+ by Cs+ is weakly energetically favorable. Figure 3-7 (b) illustrates the ion exchange energy in the defected Cu-HCF structure as a function of the number of hydrating water molecules. These exchange energies follow the same general trend as in the perfect structure. The exchange of K+ by Cs+ is slightly energetically favored, similar to that in the perfect structure, while the exchange of Na+ by Cs+ is also energetically favored, but to a lesser extent than in the perfect structure.

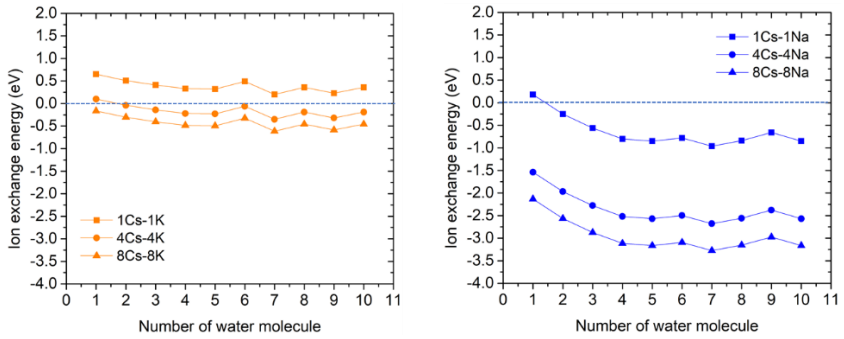


(a)

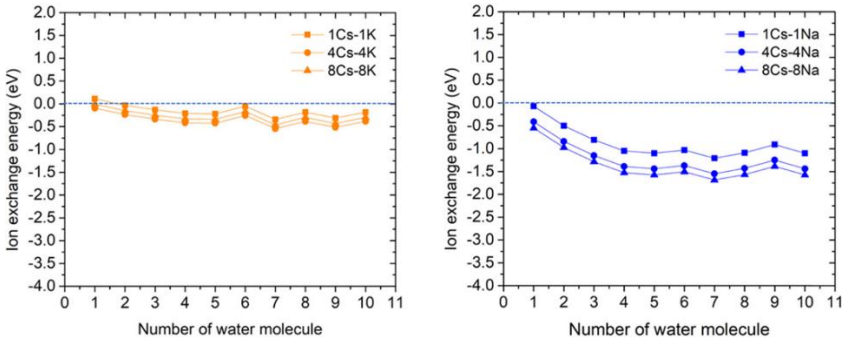


(b)

Figure 3-7. Ion exchange energy changes with the number of hydrating water molecules for the perfect structure

### 3.3.5 Configurations of Alkali Ions and Lattice Distortion

Previous calculations of Cu-HCF [49] have shown that the K+ and Cs+ ions are accommodated in the perfect structure at the 8c sites. In this work, we also initially place the Cs+ and K+ ions in 8c sites. After full relaxation, they remain in 8c sites. There are no previous calculations of Na+ in Cu-HCF structures. Interestingly, in the Fe-HCF structure, the calculations of Ling et al. [49,53] indicate that 24d is the most energetic favorable site for Na+. However, they did not perform a systematic study of how the favorable sites change as the number of Na ions increase from 1 to 8. To identify the energetically most favored location as a function of the number of Na+, we initially put the 1-8 Na+ ions in 24d sites and do a full relaxation to the structure. Then, we initially put Na+ ions in 8c sites and do a full relaxation. The 24d sites is 0.27eV energetically favored when there is only one Na+ ion in the structure; indeed, in this if a Na+ is initially placed in the 8c site it moves to a 24d during structural optimization. By contrast, the 8c site is energetically preferred when there is more than one Na+ ion in the structure. The energy favorability of the 8c site over the 24d site is 0.5eV, 1.3 eV, 1.6 eV and 1.99 eV for 2, 3, 4, 8 Na+ ions respectively. This shows that 8c sites is more and more favorable as more and more Na+ ions are added. Na+ has more space to move in the incorporation sites and thus can more easily move from the 8c point, thereby breaking the symmetry of the system. The final position of all three ions refer to the 8c sites (0.25+dx 0.25+dy 0.5+dz). For Na+ ions, the average values for dx, dy and dz are 0.022, 0.017 and 0.025. These are an order of magnitude times larger than the values for Cs+ and K+: Cs+ ions have an average dx, dy and dz of 0.0013, 0.0014 and 0.0013, while K+ ions have average displacements of 0.0013, 0.0013 and 0.0012. As we shall see below, this makes a significant difference to the overall structure.

The displacements for the defected structure are all substantially larger. For the smaller K+ and Na+ ions, the large iron cyanide vacancy in the defected structure provides more free space to move from the 8c sites to other vacant sites. The Na+ ions have average dx, dy and dx of 0.051,

0.069 and 0.068, more than twice as large as in the perfect structure. The Cs+ ions have average values of 0.018, 0.028 and 0.016; K+ has average values of about 0.025, 0.025 and 0.034; both are about ten times larger than in the undefected system.

There are eight 8c sites in the Cu-HCF framework, which indicates multiple possible arrangements for incorporating 2-6 Cs+ ions. To explore the most favored arrangement for Cs+ in Cu-HCF, we first examined the possible locations when there are two and three Cs+ in Cu-HCF structure. Figure 3-8 shows the crystallographically distinct arrangements for 2 and 3 Cs+ in Cu-HCF.

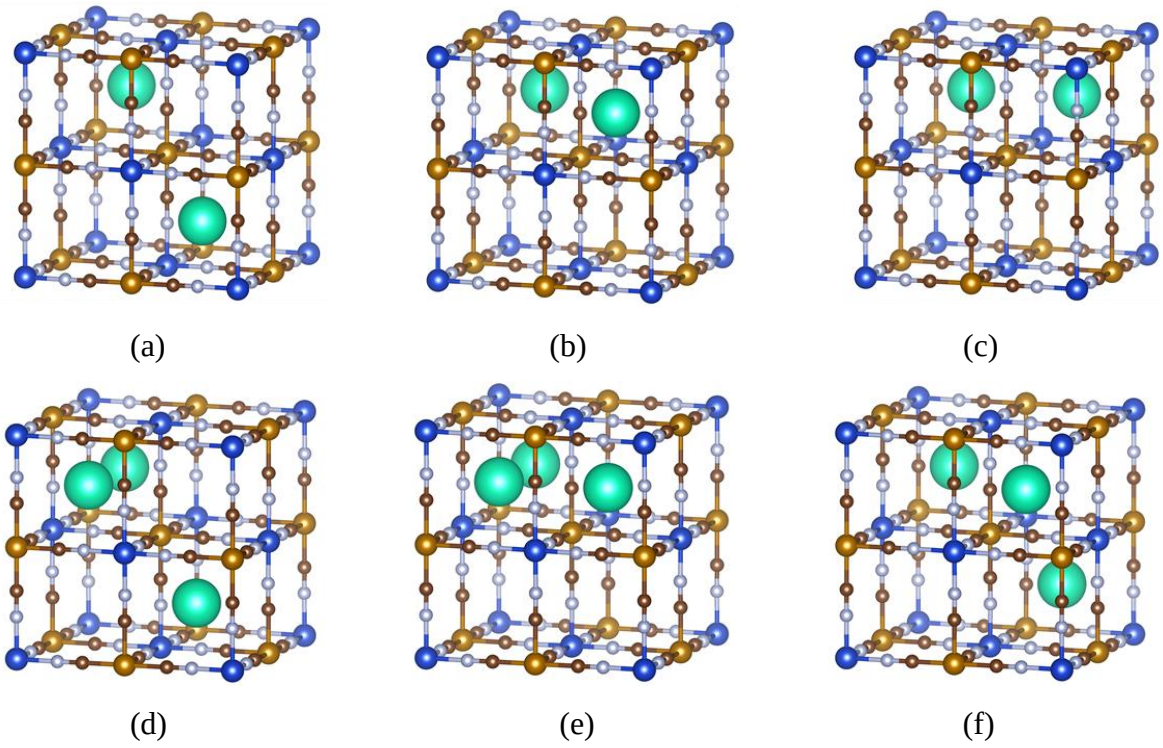


Figure 3-8. Crystallographically distinct combinations of sites for incorporation of 2 and 3 $Cs^{+}$.

For two Cs+ ions, in Figure 3-8(a) they are aligned along <111>, in 8(b) along <110>, and in 8(c) along <100>. Table 3-2 gives the energy of the various Cs+ arrangement in Figure 3-8 for the perfect cell and defected cell. For the incorporation of two Cs+ ions, the <100> arrangement of Cs+

ions in Fig. 3-8 (c) is the most energetically favored for both perfect and defected structures in both high and low concentration limits by between 0.05 eV and 0.37 eV. The structures in Fig. 3-8 (a) and 3-8 (b) have rather similar energies, except for the high concentration perfect crystal for which the <111> arrangement is strongly disfavored. For the incorporation of three ions, the structure with all three ions lying in a plane, Fig. 3-8 (e), is favored over the structure in Fig. 3-8 (d) by between 0.03 eV and 0.15 eV. The structure in Fig. 3-8 (f) is yet higher in energy by 0.16 eV to 0.58 eV.

The energy differences between different configurations are small, to save the computational cost, we choose the highest symmetry structure to do the calculations. We consider only the arrangement used in previous studies for 4 Cs+ ions: [53] that is, 4 Cs+ ions are as far as possible away from each other, as in Fig. 3-9. Based on the analysis of the 2 ion and 3 Cs+ ion cases, it likely that the energies of other arrangements are similar.

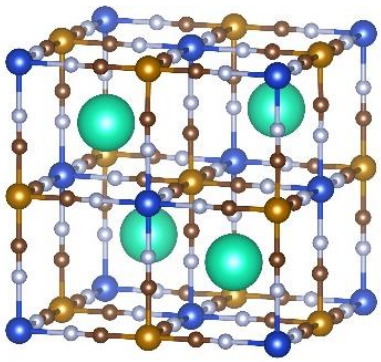

Figure 3-9. Arrangement of 4 $Cs^+$ in Cu-HCF.

In the high-concentration limit, we can determine the lattice parameters and crystallographic angles as a function of the number of alkali ions present in both perfect and defected structures. We conducted a comparison of all possible arrangements for two and three alkali ion cases and observed that the change in lattice parameter and crystallographic angles is consistent in all three directions. In

Figure. 3-10, we have plotted the change in lattice volume and crystallographic angle as a function of the number of alkali ions incorporated into the structure. Figure. 3-10 (a) shows the change of lattice volume for perfect (left) and defected (right) structures. Figure. 3-10 (b) shows the change of crystallographic angles for perfect (left) and defected (right) structures.

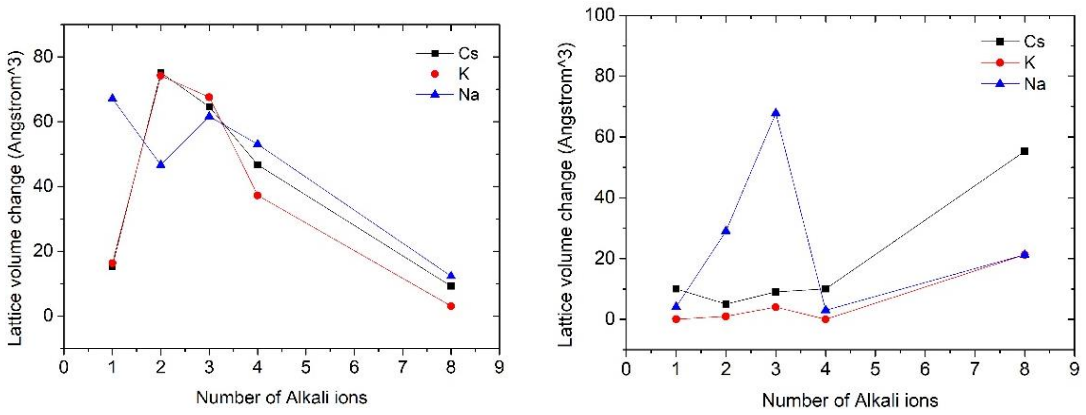


(a)

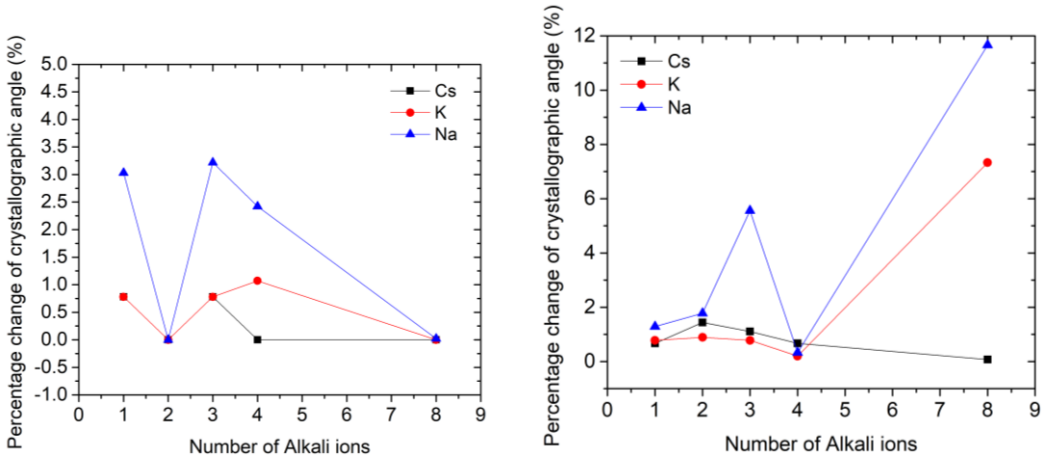


(b)

Figure 3-10. Change in the lattice volume and change of the crystallographic angles in perfect and defected structure as a function of number of alkali ions.

After relaxation, all ions in the perfect structure are located slightly away from the 8c sites. The inclusion of Cs+ ions can cause a maximum change of 80 $Å^3$ in the lattice volume, which represents a 7.7% change in the volume of 1033.4 $Å^3$. This is calculated based on the lattice parameter of 10.11Å, and a maximum change of 1.0% can occur in the lattice angle. The addition of

Na+ ions result in a decrease in symmetry, causing deviations from the initial cubic structure and breaking of the degeneracy of the lattice parameters due to large displacements from the 8c positions. Fig. 3-10 (a) shows that the system symmetry is higher when eight ions are added compared to when four are added. The incorporation of one or three alkali ions also leads to large changes in lattice parameters due to the low symmetry inside the framework.

In defected structures, Cs+ ions can cause a maximum change of 60 $Å^3$ in the lattice volume and a 1.0% change in the lattice angle. As the number of alkali ions increases to eight, the changes in crystallographic angles for K+ and Na+ are significant at 6% and 12%, respectively. This causes an overall distortion of the lattice. However, Cs+ ions create virtually no change in crystallographic angle due to their proximity to cyanide groups, which reduces their ability to move within the structure because of the CN-Cs+ attraction, despite the presence of a large void at the center. As a result, the symmetry of the structure is even lower than that in the perfect structure. In contrast to the trend observed in the perfect structure, the lattice distortion increases as the number of alkali ions increases from 4 to 8 in the defected system. This is because the presence of a large ion cyanide vacancy creates more space for the smaller K+ and Na+ ions to move and increases the asymmetry of the structure. Compared to the other two alkali ions, Cs+ leads to the smallest lattice distortion.

### 3.3.6 Charge Density and Structural Stabilization

To gain insight into the local bonding environments in the system, we analyzed charge density maps by plotting the charge density difference, $\Delta\rho(r)$. This is defined as the charge density in the system of interest minus the charge densities of single isolated atoms at the various lattice sites. This characterization allows us to observe how bonding in the system changes the local charge density environment. We presented the charge density difference plots for the (1 0 0) plane in Figure 3-11 for both the perfect and defected structures (Blue: copper, brown: iron; white: nitrogen; black: carbon.). The 8c sites are located 0.25a above and below these planes at the centers of the square

formed by the metal ions. Figure 3-12 shows the results. Figure 3-12 (a) (b) (c) shows the results in perfect structure without Cs+, with 4 Cs+ ions and with 8 Cs+ ions, respectively. Figure 3-12 (d) (e) (f) shows the results in defected structure without Cs+, with 4 Cs+ ions and with 8 Cs+ ions, respectively. For 4 Cs+ ions, the red and white denote above and below the plane. For 8 Cs+ ions, there are atoms below and above the plane in all four positions.

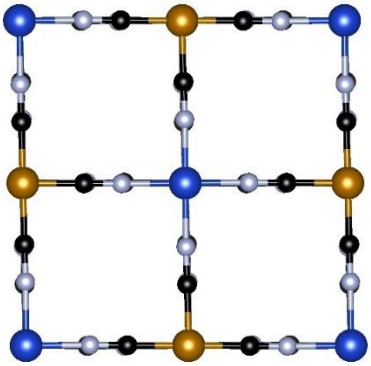

Figure 3-11. (1 0 0) plane of Cu-HCF structures.

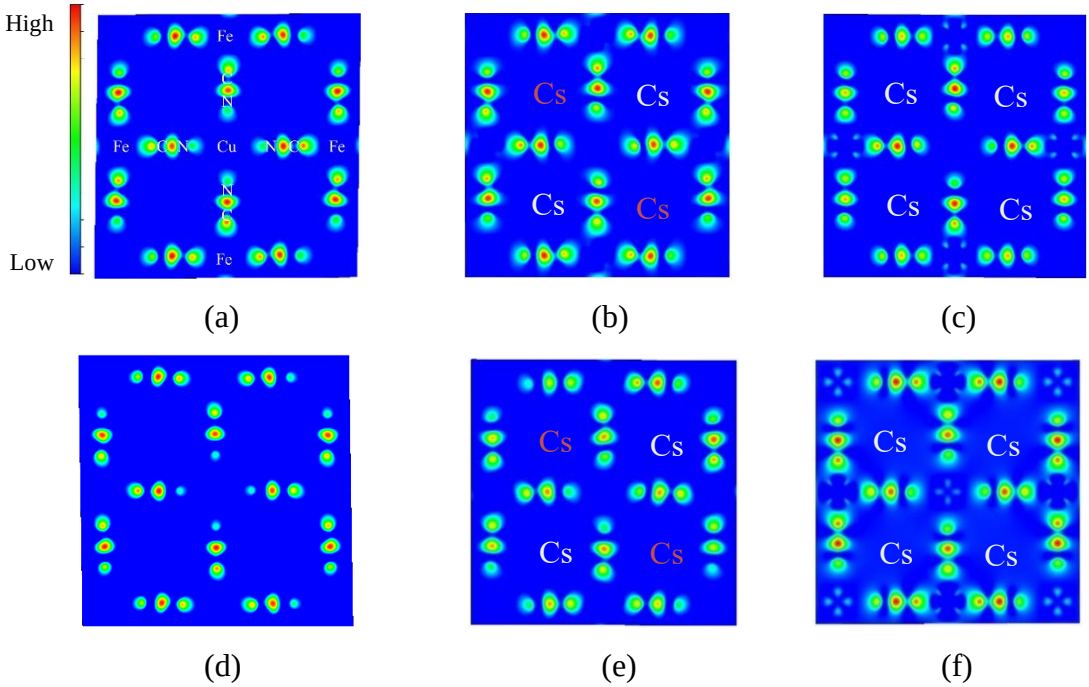


Figure 3-12. 2D charge density difference map of perfect Cu-HCF and defected Cu-HCF

Figure 3-12 displays significant charge accumulation between the transition metals and cyanide ligand, suggesting the presence of strong covalent bonds between them. Specifically, in Figure 3-12 (a), the green area between Fe-C, C-N and Cu-N indicates charge accumulation between these elements, while the red area between C and N denotes strong bonding between them. Comparing Figures 3-12 (a), (b), and (c), we observe that the green area between metal and cyanide ligand increases in size, indicating that the addition of Cs+ ions leads to more charge accumulation between Cu and N and between Fe and C. This strengthens the covalent bonds between these atoms.

Comparing the defected structure in Figure 3-13 (d) to the perfect structure in Figure 3-12 (a), we observe that the charge accumulation between the transition metal and cyanide ligand in the defected structure is significantly less than that in the perfect structure. This suggests that the presence of a large vacancy site decreases the stability of the structure.

After the incorporation of Cs+ in the defected structure, Figure 3-12 (e) and (f) reveal that the metal-ligand bond strength is increased, which compensates for the reduced stability caused by the vacancy. The addition of K+ and Na+ ions also reinforce the defected Cu-HCF structure. However, the results of K+ and Na+ incorporation in the defected structure differ from those of the perfect structure, as shown in Figure 3-13 (from left to right: 4 $K^+$, 8 $K^+$, 4$Na^+$, 8 $Na^+$). The large lattice distortion that occurs when 8 K+ or Na+ ions are added weakens the metal-cyanide interaction and reduces the overall stability of the structure.

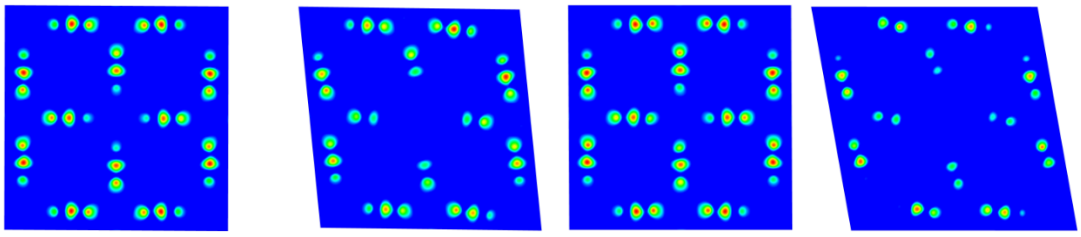

(a) (b) (c) (d)

Figure 3-13. 2D charge density difference map of defected Cu-HCF with 4 $K^+$ ions. 8 $K^+$ ions. 4 $Na^+$ ions. 8 $Na^+$ ions.

### 3.3.7 Electronic and Magnetic Structure

$Cs^+$ incorporation also results in changes in the electronic structures of both perfect and defected Cu-HCF. Figure 3-14 ( (a) no $Cs^+$ ion. (b) 4 $Cs^+$ ions. (c) 8 $Cs^+$ ions and defected Cu-HCF with (d) no $Cs^+$ ions. (e) 4 $Cs^+$ ions. (f) 8 $Cs^+$ ions.) shows the density of states of Cu-HCF structures with addition of 0, 4 and 8 $Cs^+$ ions. Vertical dotted line denotes Fermi level. As Figure 3-14 (a) shows, for perfect Cu-HCF the states from all four elements have small overlapping energy ranges at about -6 eV and near to the Fermi level. Even greater overlap is present in structures with 4 or 8 $Cs^+$ ions in these energy ranges. This is consistent with the increase in strength of the bond between the metals and cyanide. The same trend is also observed in the defected structure as the number of $Cs^+$ increases. These changes in the electronic DOS are consistent with the 2D charge density difference plots and give further evidence that $Cs^+$ incorporation increases the bond strength and stabilizes the structure. A recent experimental study from Moloney et al. indicates that the exchange of other alkali ions with $Cs^+$ in Cu-HCF increases the thermostability of Cu-HCF, which is consistent with these observations.[54]

The incorporation of the alkali ions into the structure changes the charge states of the Cu and Fe, as shown in Table 1-1. Wojdeł et al. indicates that during this process, low spin Fe first reduces from the +3 charge state to the +2 charge state, followed by the high spin elements in the structure. [37] In our cases, similarly, it is reasonable to expect the charge of low spin Fe to first decrease from +3 to +2. Only if needed for further charge balance will the charge of high spin Cu decrease from +2 to +1. This reduction allows Cu and Fe to eliminate unpaired electrons in d-orbitals, which impacts the magnetic properties of Cu-HCF. The DOS plots also validate this. Figure 3-15 shows the d-orbital configurations of Cu and Fe ions in both perfect and defected structures as a function of the number of incorporated alkali ions. Figure 3-15 (a) (b) (c) shows the configuration of perfect structures with

no $Cs^+$, 4 $Cs^+$ and 8 $Cs^+$, respectively. Figure 3-15 (d) (e) (f) shows the configuration of defected structures with no $Cs^+$, 4 $Cs^+$ and 8 $Cs^+$, respectively.

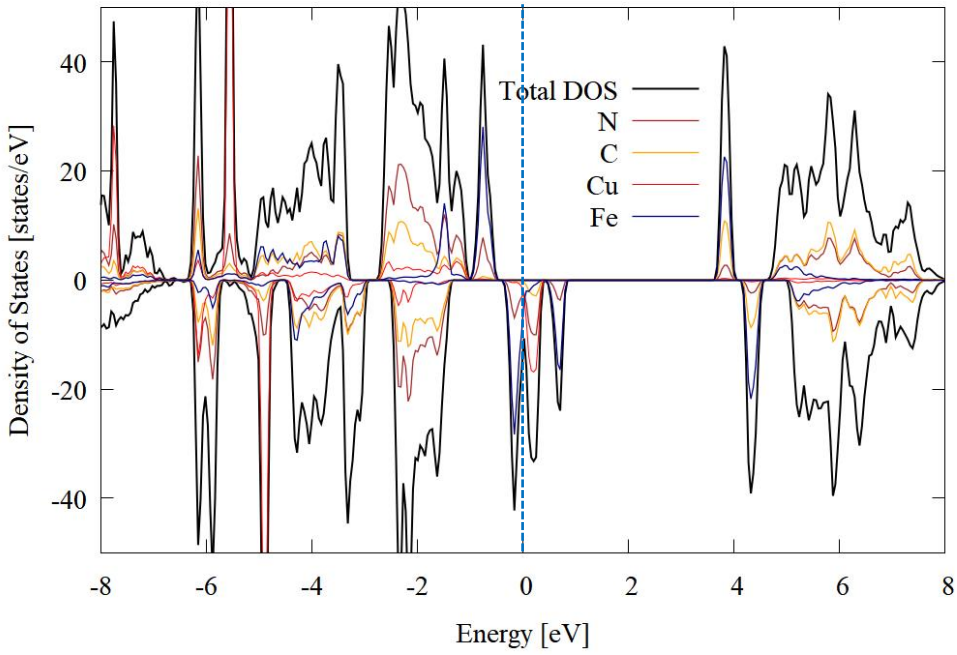


(a)

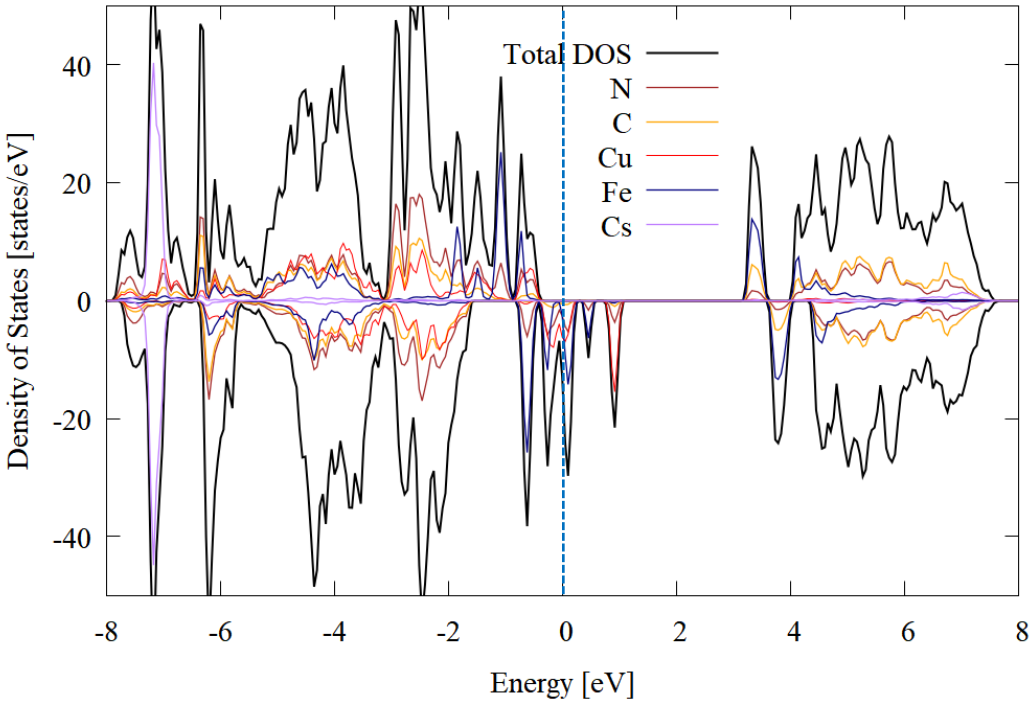


(b)

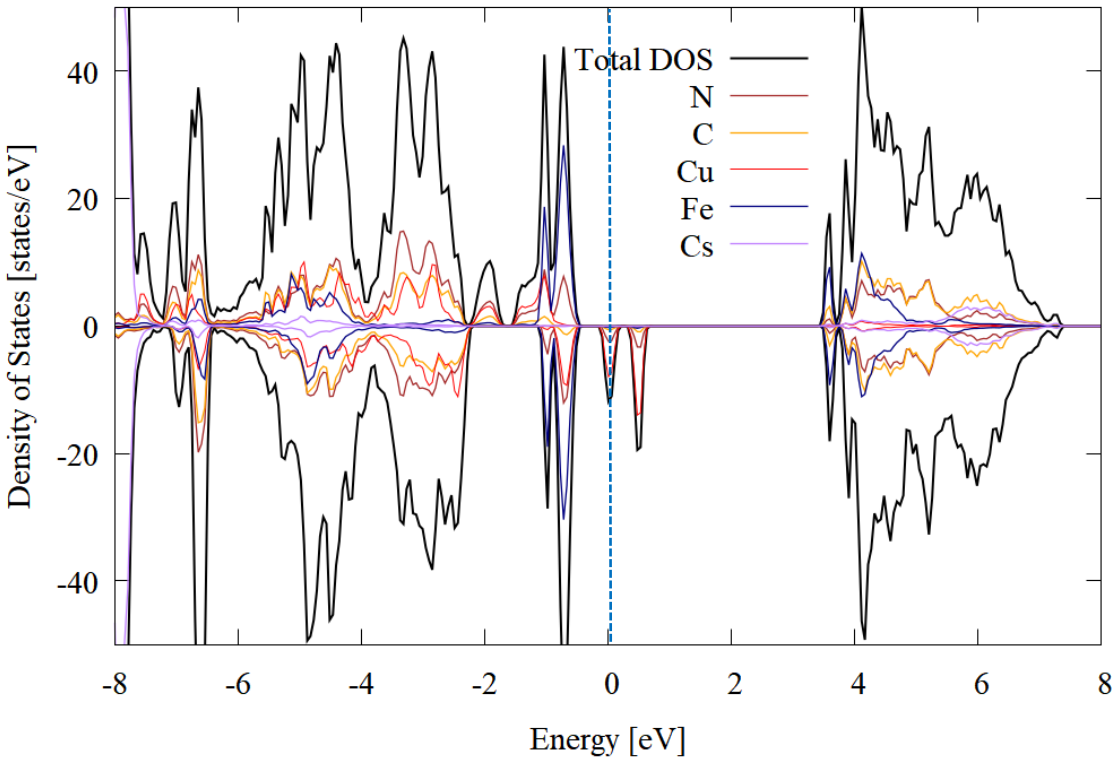
Total DOS
N
C
Cu
Fe
Cs
Density of States [states/eV]
Energy [eV]
40
20
0
-20
-40
-8
-6
-4
-2
0
2
4
6
8

(c)

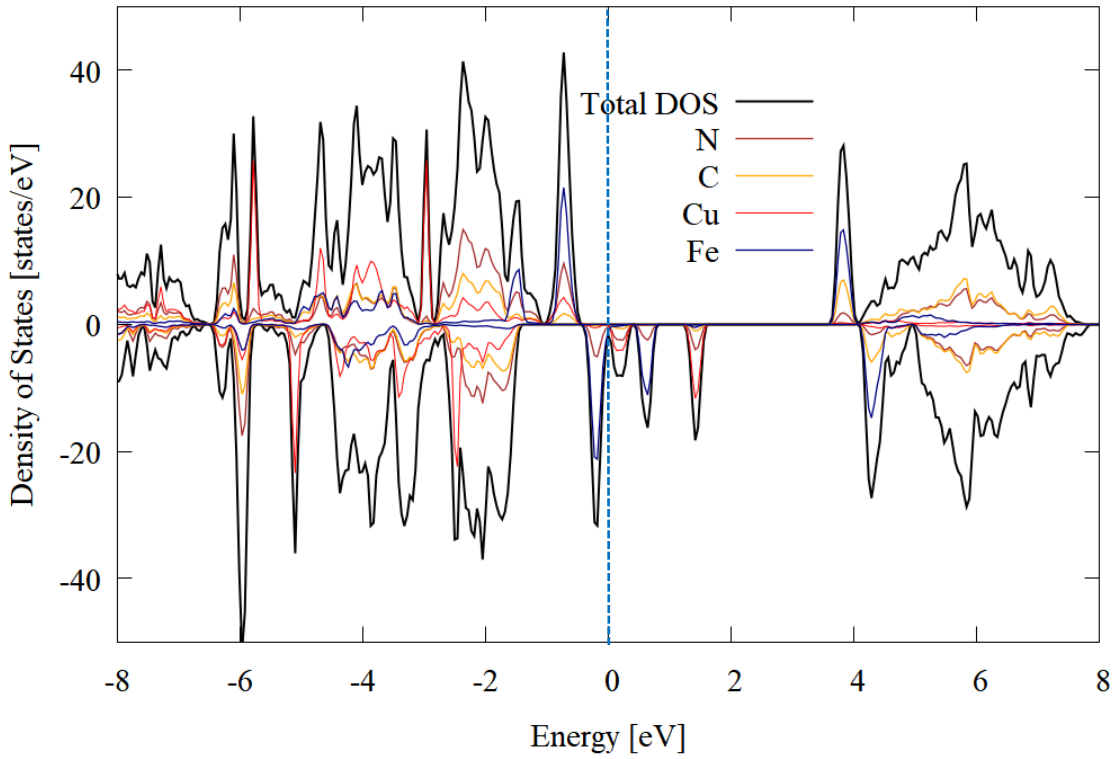
Total DOS
N
C
Cu
Fe
Density of States [states/eV]
Energy [eV]
40
20
0
-20
-40
-8
-6
-4
-2
0
2
4
6
8

(d)

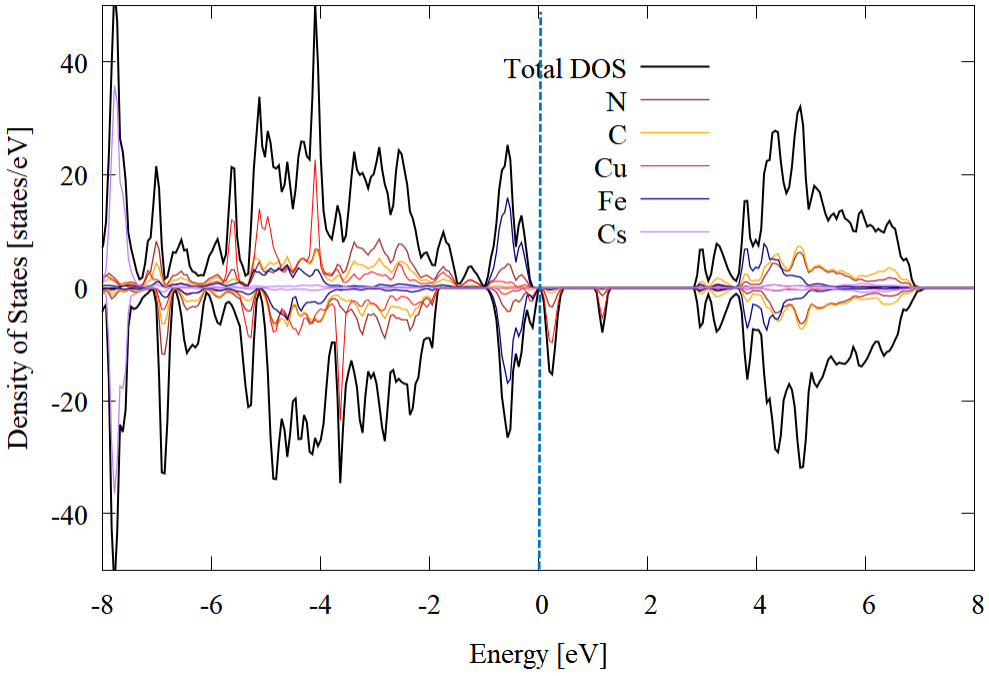


(e)

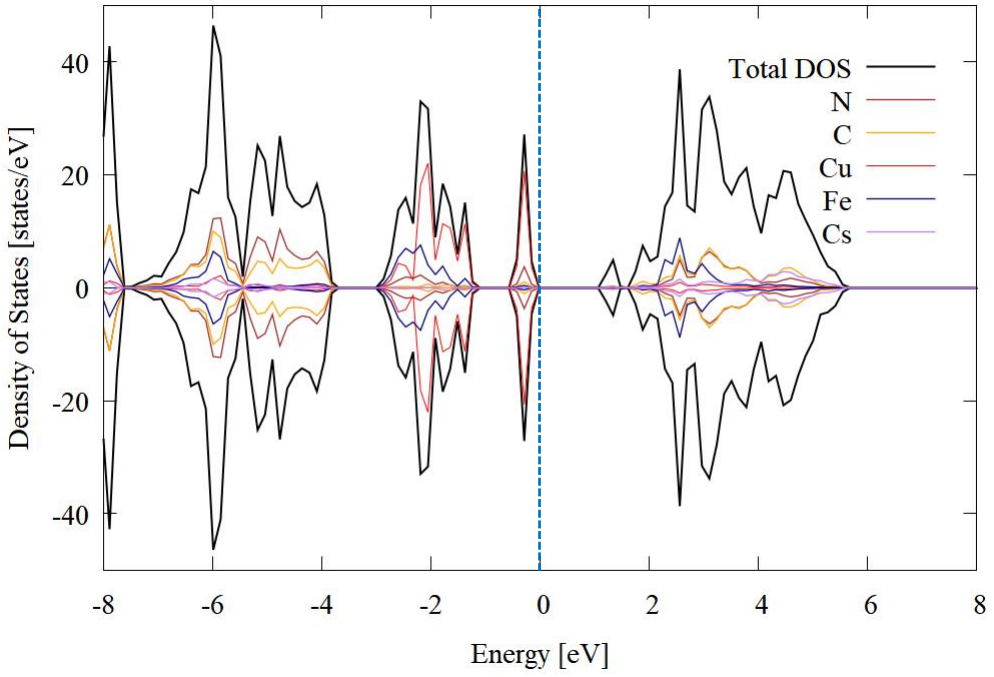


(f)

Figure 3-14. Density of states of perfect Cu-HCF structure with no $Cs^+$ ion. 4 $Cs^+$ ions. 8 $Cs^+$ ions and defected Cu-HCF with no $Cs^+$ ions. 4 $Cs^+$ ions. 8 $Cs^+$ ions.

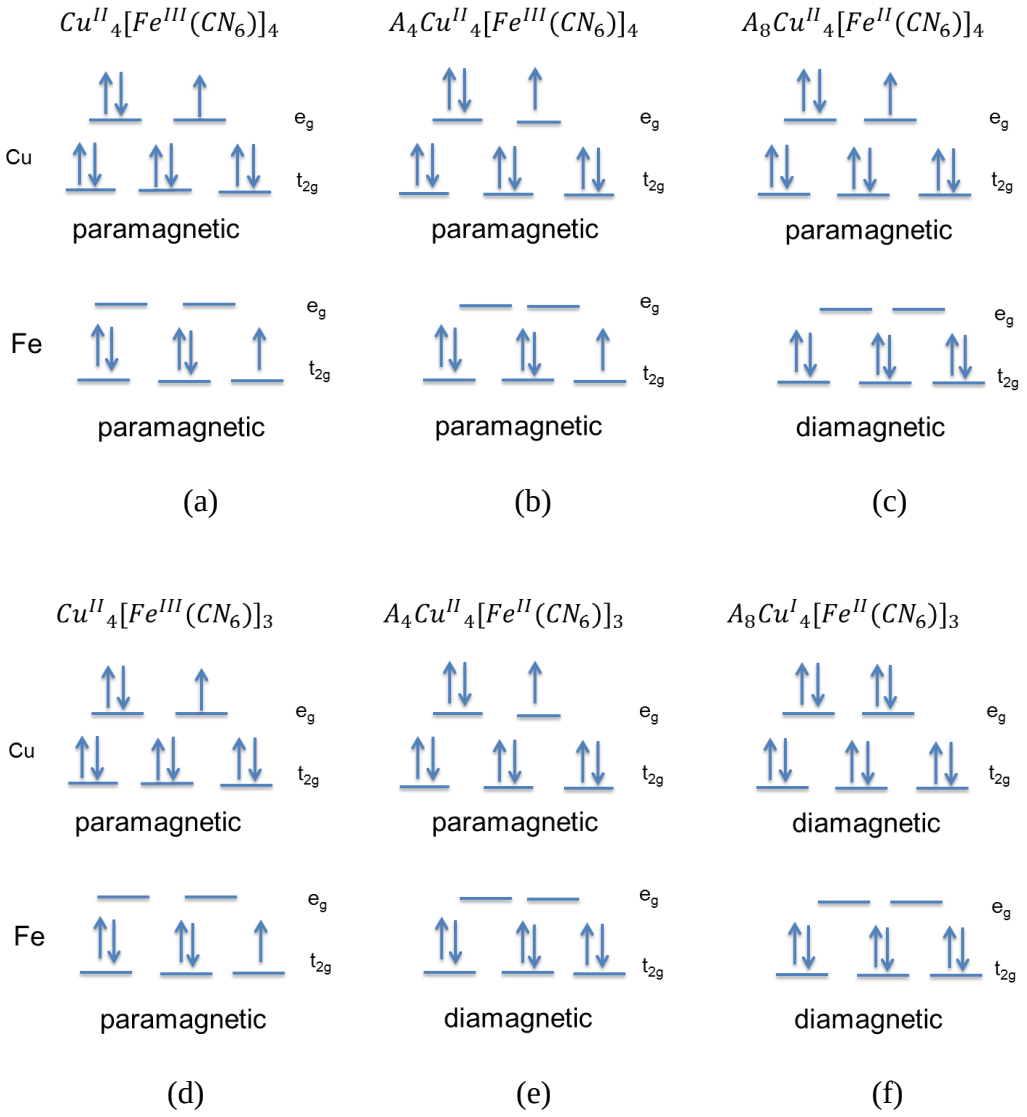


Figure 3-15. d-orbital configurations of Fe and Cu in perfect Cu-HCF and in defected Cu-HCF

In the perfect Cu-HCF structure without Cs+ or with 4 Cs+ ions, as shown in Figure 3-15 (a) and (b), both Fe and Cu have unpaired electrons which result in local magnetic moments, as is shown in Tables 3-2. This structure is paramagnetic for both Fe and Cu. These unpaired electrons in Cu and Fe are also evident from the differences in the spin up and spin down channels in the density of states plots shown in Figure 3-14 (a) and (b). In perfect Cu-HCF with 8 Cs+ ions, shown in Figure 3-15 (c), the reduction of Fe eliminates the unpaired electrons and only leaves an unpaired electron from Cu.

Thus, the local magnetic moment in Fe is eliminated, while Cu still has a non-zero magnetic moment, as is shown in Table 3-2. This means that the Fe become diamagnetic rather than paramagnetic, while the Cu remains paramagnetic. For the density of states plot with 8 Cs+ ions, Figure 3-14 (c), because of unpaired electrons, the Cu peak is still asymmetrical between the two spin channels in the energy range -8 eV to 2 eV, while the Fe peaks are symmetrical for all energies range because all of its electrons are perfectly paired. The small differences in the magnetic moment of crystallographically identical ions (up to about 0.03 $\mu_B$ in some cases) is a measure of the degree of convergence of the calculations.

In the defected structure without $Cs^+$ ions shown in Figure 3-15 (d), unpaired electrons in both Fe and Cu d-orbitals result in local magnetic moments, as listed in Table 3-2; these are also associated with the asymmetry between the two spin channels in the DOS peaks in the energy range -8 eV to 2 eV. As the number of alkali ions increases to 4, the Fe ions are reduced. As listed in Table 3-2, eliminating the unpaired electrons in Fe eliminates the local magnetic moment, as also evidenced by the symmetrical Fe peaks symmetrical in the DOS plot over the entire range of energies. Cu still has unpaired electrons resulting in a local magnetic moment and asymmetrical peaks in the range of -8 eV to 2 eV. When there are 8 $Cs^+$ ions, both Cu and Fe are reduced, with the result that neither has an unpaired electron. The result is that the magnetic moments of both Fe and Cu vanish as shown in Table 3-2 and the DOS plot is perfectly symmetrical.

The first Cu in Table 3-2 defected structure which is in the corner of the structure has a much higher magnetic moment than other Cu ions in the face center. The Cu-N bond length for this Cu ion is slightly longer than for the other Cu ions, indicative of lower covalency. The first Cu ion is more likely to have unpaired electrons alone and is less likely to share them with its neighbor, N. In the structure with 8 Cs+, the Cu-N bond for the first Cu ion is shorter than other Cu-N bonds which

indicates that it is less likely to have unpaired electrons. The shortening of the Cu-N bond can be explained by the distance between $Cs^+$ and CN-. The CN ligand connecting to the first Cu is further from the $Cs^+$ ions than the other CN ligand is from the other Cu ions. When Cs-CN interaction becomes weaker, a stronger Cu-CN interaction become possible; as a result, the Cu-N distance decreases.

In a recent study, Moloney et al. [54] show that the Cs absorption rate can be increased notably by magnetic dispersion of the aggregated Cu-HCF particles because the application of a magnetic field can drive the formation of a uniform and stable colloidal dispersion and increase the exposed surface area. They also believe that it is the intrinsic magnetic nature of Cu-HCF that makes the magnetic agitation work. [55] We indeed find there are magnetic moments in the Cu-HCF framework, even in the absence of alkali ions, which is consistent with the effectiveness of magnetic dispersion.

Table 3-2. Local magnetic moment in Bohr magnetons of Fe and Cu in perfect and defected Cu-HCF

| | | magnetic moment of Fe | | | | magnetic moment of Cu | | | |
|---|---|---|---|---|---|---|---|---|---|
| | | $Fe_1$ | $Fe_2$ | $Fe_3$ | $Fe_4$ | $Cu_1$ | $Cu_2$ | $Cu_3$ | $Cu_4$ |
| perfect | 0 Cs | 1.06 | 1.06 | 1.06 | 1.06 | 1.00 | 1.00 | 1.00 | 1.00 |
| | 4 Cs | 0.92 | 0.90 | 0.90 | 0.90 | 0.78 | 0.75 | 0.76 | 0.76 |
| | 8 Cs | 0.02 | 0.00 | 0.00 | 0.00 | 0.68 | 0.75 | 0.75 | 0.75 |
| defected | 0 Cs | 0.99 | 0.99 | 0.99 | | 1.02 | 0.66 | 0.67 | 0.67 |
| | 4 Cs | 0.01 | 0.02 | 0.02 | | 0.73 | 0.66 | 0.66 | 0.66 |
| | 8 Cs | 0.00 | 0.00 | 0.00 | | 0.00 | 0.00 | 0.00 | 0.00 |

## 3.4 Conclusions

A detailed DFT study of $Cs^+$ incorporation with Cu-HCF structure has been carried out. The influence on Cu-HCF lattice distortion, energetics, structure stabilities and electronic structures

caused by $Cs^+$ incorporation has been characterized. From DFT calculations, the essential question of why $Cs^+$ incorporation in Cu-HCF structure is favorable compared to $K^+$ and Na+ atoms was identified as being due to the much smaller lattice distortion caused by the $Cs^+$ in defected Cu-HCF compared to the other two alkali ions. Analysis of the alkali ion incorporation energy and ion exchange energy showed that $Cs^+$ incorporation is more thermodynamically favorable than $K^+$ and Na+. It was also found that $Cs^+$ reinforces the Cu-HCF structures by strengthening the metal-ligand bond. The increased overlap area of transition metal and ligand peaks as the number of $Cs^+$ being incorporated increases was also indicative of $Cs^+$ incorporation strengthening the metal-ligand connection. This is verified by experiment. Further, the densities of states also reflect the change of the magnetic moment of transition metals resulting from the reduction process happening in transition metals. All the calculations demonstrate that $Cs^+$ incorporation in Cu-HCF is favorable compared to other alkali ions such as $K^+$ and $Na^+$. The intrinsic magnetic properties of the empty Cu-HCF framework suggest that uniform and stable colloidal dispersions that can absorb more $Cs^+$ ions may be created by magnetic dispersion.

CHAPTER 4
INCORPORATION OF RADIOACTIVE CESIUM INTO HYDRATED COPPER HEXACYANOFERRATE BY DENSITY FUNCTIONAL THEORY CALCULATIONS

## 4.1 Background

Cu-HCF has proved to be a good candidate to sequester $Cs^+$ from aqueous environments. The thermodynamics of $Cs^+$ sequestration in non-aqueous environments were studied in Chapter 3. However, in the practical scenarios, Cu-HCF is usually defected with a large iron cyanide vacancy in the center and is hydrated. There are two different types of water molecules inside the framework: coordinated water molecules and zeolitic water molecules. [56] Zeolitic water molecules are free water molecules, unbonded to any neighboring atoms in the inorganic structure, though possibly bonding to each other. Coordinated water molecules are bonded to atoms in the inorganics structure, in this case to Cu ions in Cu-HCF framework, as Figure 4-1 shows (left : coordinated water; right: zeolitic water).

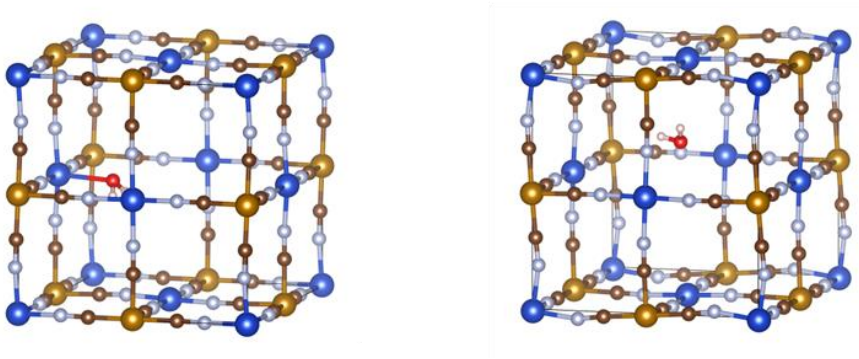

Figure 4-1. Coordinated water molecule and zeolitic water molecule in the defected Cu-HCF framework.

There is still limited work exploring how water molecules are distributed in Cu-HCF and how they can impact the Cs+ incorporation and Cs-Alkali exchange. A computational study by Mink et al. have studied the six water molecules Cu-HCF system. They determined the configurations of all the water molecules inside the Cu-HCF bulk. [57] However, no

thermodynamic analysis was used to explain these configurations or to characterize the alkali-water interaction inside the Cu-HCF. Xu et al. studied the electrochemical properties of hydrated Cu-HCF. [58] The structure of Cu-HCF in their study is the monoclinic structure which is far from our cubic structures. Neither of these works reported on how water molecules can impact $Cs^+$ ions incorporation. In this chapter, we conducted a systematic study of hydrated Cu-HCF using density functional theory calculations. Our study included determining the maximum number of water molecules that can be incorporated into the Cu-HCF framework and the distribution of coordinated water molecules and zeolitic water molecules within the framework. We also investigate the configuration of $(H_2O)_n$-$Cs^+$, $(H_2O)_n$-$K^+$, and $(H_2O)_n$-$Na^+$ complexes inside the Cu-HCF framework, where n represents the number of water molecules binding with alkali ions. Finally, we examined how water molecules affect the incorporation energies and exchange energies of alkali ions. Our study provides valuable thermodynamic insights into the alkali ion sequestration process in hydrated Cu-HCF, which is relevant to practical applications.

## 4.2 Methodology

### 4.2.1 Density Functional Theory Calculations

Relaxing structures with water molecules can be challenging, but there are some useful tips for the hydrated Cu-HCF system. First, it is important to switch off the symmetry when generating input file files because water molecules move randomly and do not follow specific symmetry because leaving the symmetry tag open in the input file can make it difficult to achieve convergence. Second, avoid setting a very low convergence criterion; 0.05 eV is generally sufficient [59] for such a complex system. Setting the convergent force too low due to water-water interactions may prevent relaxation from achieving convergence. Last, it is important to monitor the trend of the system force and total energy. Water molecules can tilt and move during relaxation, and many configurations may have the same or very similar system

energy. If the trend of the total energy or force curve fluctuates near a value and does not decrease further, it may indicate that convergence has been achieved. All of the calculations are based on the fixed cell shape. All other parameters are the same as Section 3.2.1.

### 4.2.2 Hydrated Cu-HCF System

To begin, we determine the maximum number of water molecules that can be incorporated into the Cu-HCF framework. This calculation is important to prevent the addition of an excessive number of water molecules to our system. Following this, we calculate the water-framework binding energy using the following equation:

$$E_{binding} = E_{hydrated\ framework} - E_{empty\ framework} - E_{nH_2O} \quad (4\text{-}1)$$

$E_{hydrated\ framework}$ is the energy of the Cu-HCF framework hydrated by n water molecules. $E_{empty\ framework}$ is the energy of Cu-HCF without any water molecules. $E_{nH_2O}$ is the energy of n water molecules. Through Equation 4-1, we can gain insight into the type of water molecule preferred by the framework and how they are distributed when multiple water molecules are present within the framework. This calculation is essential in establishing a reasonable configuration when incorporating alkali ions into the framework.

### 4.2.3 Alkali Ion Incorporation Energy and Exchange Energy

We initially place the alkali ions in the center of the framework as it has the largest space for the ions and accompanying water molecules. Then, we perform an ionic relaxation for the whole structure and let alkali ions move to the most favorable sites and calculate the ion incorporation energy by Equation 4-2:

$$E_{incorporation} = \left(\frac{1}{N}\right)\{E_f(N) - E_0 - NE_{ref(A)}\} \quad (4\text{-}2)$$

$E_f(N)$ is the energy of structure after insertion of the N alkali ions, A=$Cs^+$, $K^+$ or $Na^+$; $E_0$ is the energy of hydrated Cu-HCF without any alkali atoms. The structure and energy are then allowed

to equilibrate. $E_{ref}$ is the reference energy for the alkali atoms. The values for $Cs^+$ ions are compared with the corresponding values for $K^+$ and $Na^+$ calculated in the same way. For the physically realistic scenario of the alkali atom being in a hydrated environment, the reference states of alkali ions will be the difference in the energy of a "droplet" of n water molecules containing an alkali ion and a water droplet without an alkali atom: $E_{ref(A)} = \{[A(H_2O)_n]^+ - E(n_{H_2O})\}$. For n=0, this would simply correspond to the energy of a single alkali ion in vacuum.

For ion exchange energy, we use Equation 4-3:

$$E_{exchange}(N) = \left(E_{Cs}(N) - E_{K/Na}(N)\right) - N(E_{ref(Cs)} - E_{ref(K/Na)}) \quad (4\text{-}3)$$

$E_{Cs}(N)$ is the energy of the lattice with N $Cs^+$ ions; $E_{K/Na}(N)$ is the energy of the lattice with N $K^+$ or $Na^+$ ions; $E_{ref(Cs)}$, $E_{ref(K)}$ are the reference energies for $Cs^+$ and $K^+$ hydrated with n water molecules, respectively, as described above.

## 4.3 Results and Discussion

### 4.3.1 Maximum Number of Water Molecules in Cu-HCF Framework

First, we estimate theoretically the number of water molecules that could be accommodated in a single unit cell of the framework by setting the density of Cu-HCF box with water molecules to the density of pure water (1 $gcm^{-3}$). The volume of the box can be expressed as Equation 4-4:

$$V_{box} = V_{Cu-HCF} - 3V_{Fe_{atom}} - 4V_{Cu_{atom}} - 18V_{cynide} \quad (4\text{-}4)$$

$V_{box}$ is the volume of Cu-HCF framework without Cu Fe and cyanide ligands. $V_{Cu-HCF}$ is the volume of Cu-HCF framework with all the ions listed above. $V_{Fe_{atom}}$ $V_{Cu_{atom}}$ and $V_{cynide}$ are the volume of all the ions listed above. There are 3 Fe ions, 4 Cu ions and 18 cyanide ligands in one defected Cu-HCF conventional unit cell. By Equation 4-4, our calculated maximum number of water molecules is 27. This estimate is much larger than the value of 16, reported by the

previous experimental work. [60] To address this issue, we recall that water molecules tend to bind with each other to form droplets. We see this effect in the PBA, as illustrated in Figure 4-4.

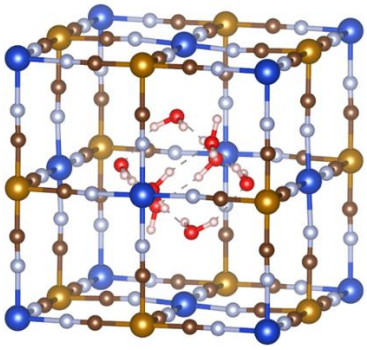

Figure 4-2. Water cage in the center of Cu-HCF framework.

Based on the configuration presented in Figure 4-2, it is reasonable to suppose that the full volume of the box is not actually available to the water. Instead, we will use the configuration presented in Figure 4-3, which involves a spherical droplet in the center, to calculate the volume and subsequently determine the number of water molecules present within the framework.

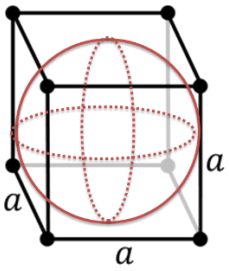


Figure 4-3. Water cage sphere in the center of Cu-HCF framework.

The diameter of the sphere should correspond to the length of the Cu-HCF lattice parameter. Using this configuration, we were able to determine that the maximum number of water molecules present within the Cu-HCF framework is 18, which is in good agreement with the experimental value of 16.

Using Equation 4-1, we calculated the binding energy between the Cu-HCF framework and water molecules. Initially, we incorporated a single water molecule into the framework, for which there are two scenarios: coordinated water and zeolitic water. The binding energy of the coordinated water molecule was lower than that of the zeolitic water molecule, indicating that coordinated water molecules are energetically favorable by the Cu-HCF framework. To determine if this conclusion holds for cases with more than one water molecule, we proceeded to add another water molecule to the system. For two water molecules, there were four different scenarios, as shown in Figure 4-4:

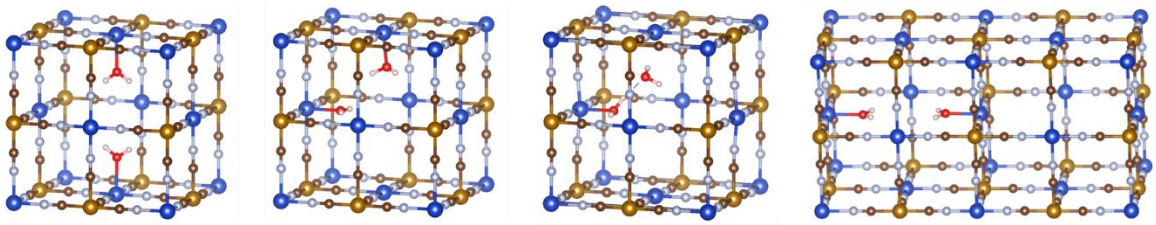

Figure 4-4. Various configurations of 2 water molecules system.

The first configuration has two water molecules far from each other and, because we have a single unit cell in periodic supercell, coordinated to the same Cu ion. The second configuration has two water molecules close to each other and coordinated to different Cu ions. The third configuration has one water molecule coordinated with Cu ion and has another zeolitic water molecule binding with the coordinated water molecule by a hydrogen bond. The first three configurations can be considered a corresponding to high overall concentrations of water, in which all of the unit cells have the same water configuration. The last configuration is a 1x2x1 supercell. There are two water molecules far from each other and coordinated to the different Cu ions. This can be considered as mimicking a lower overall concentration of water in the system;

calculations on unit cells larger than 1x2x1 are prohibitively expensive and are only considered for this one case. The normalized water-framework binding energies are shown in Table 4-1

Table 4-1. Normalized water-framework binding energies; number 1-4 corresponds to the configuration from left to right in Figure 4-4.

| Configurations | 1 | 2 | 3 | 4 |
|---|---|---|---|---|
| Water Binding Energy (eV) | -0.45 | -0.57 | -0.63 | -0.70 |

The fourth configuration has the most negative (most favorable) binding energy compared to other cases, indicating that it is the most energetically favorable configuration within the Cu-HCF framework. In this configuration, two copper water molecules are coordinated to different Cu ions and positioned far apart, eliminating any competition or repulsion between them. This arrangement allows for strong binding of the water molecules to the framework, resulting in a stable and energetically favorable state. The third configuration is the next lowest, with the lowest binding energy under high water concentration scenarios. In this arrangement, only one water molecule is coordinated with a Cu ion, being connected to the other zeolitic water molecule through a hydrogen bond. This configuration exhibits a favorable balance between coordination and hydrogen bonding, enhancing the stability of the system. Moving on, the second configuration has the second-highest binding energy: the close proximity of the two water molecules in this arrangement leads to repulsion between them but still far away from each other to form hydrogen bond, weakening their binding to the framework. Finally, the first configuration has the highest binding energy value, presumably arising from the competition between the two water molecules to coordinate with the same Cu ion. Since we are interested in the physical situation of a high-water concentration scenario, the third configuration is reasonable. We can conclude that their will only be one coordinated water molecule when there is more than one water molecule in Cu-HCF. Instead, zeolitic water molecules will first form and

bind with each other through hydrogen bonds to form a water cage sphere in the center of the framework, as shown in Figure 4-4. Coordinated water will only form when there are too many zeolitic water molecules, and there is not enough space for them to form. Figure 4-5 shows the 14 (left) and 18 (right) water molecule scenarios, which confirm our conclusions. Six water molecules are formed when there are too many zeolitic waters in the structure. From Figure 4-7 we find large lattice distortion due to the incorporation of too many water molecules.

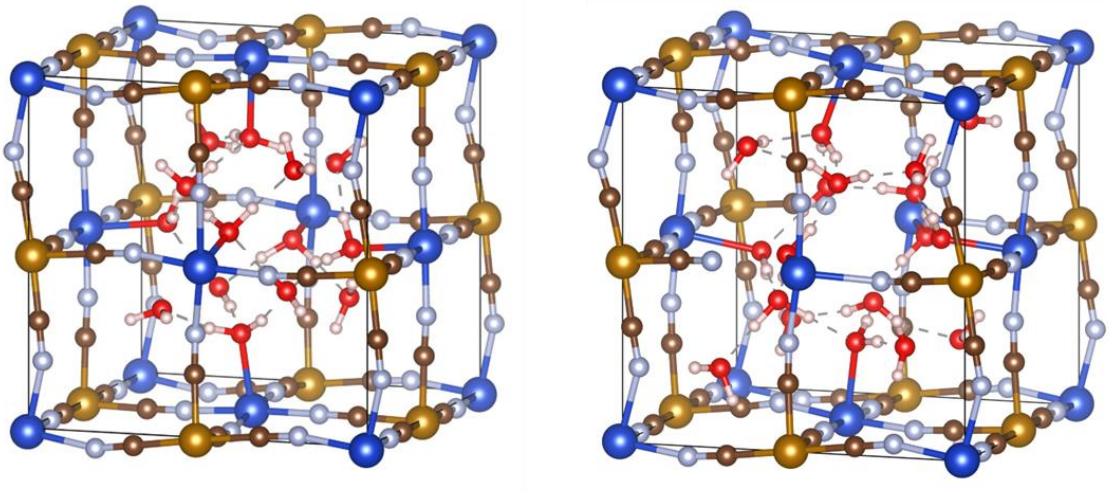

Figure 4-5. Relaxed structure of Cu-HCF with 14 water molecules and 18 water molecules.

### 4.3.2 Configuration of Alkali-Water Complex in Hydrated Cu-HCF

We incorporate alkali ions into the center of Cu-HCF to form a water-alkali complex inside the center of structure; a representative as the initial configuration, before structural relaxation, is shown in Figure 4-6 (left to right: Na-6 water K-6 water and Cs-6 water). in this configuration, zeolitic water molecules form a sphere around the alkali ion and there are no coordinated water molecules, which is in accord with our previous analysis of the distribution of the water. Moreover, this is possible because there is enough space in the center site to easily accommodate the alkali-water complex. We use 6 water molecules as this number is the

maximum number of water molecules in the first water-Na and water-K coordination shells and 10 water molecules which is the maximum number of water molecules in the first water-Cs coordination shell. [45]

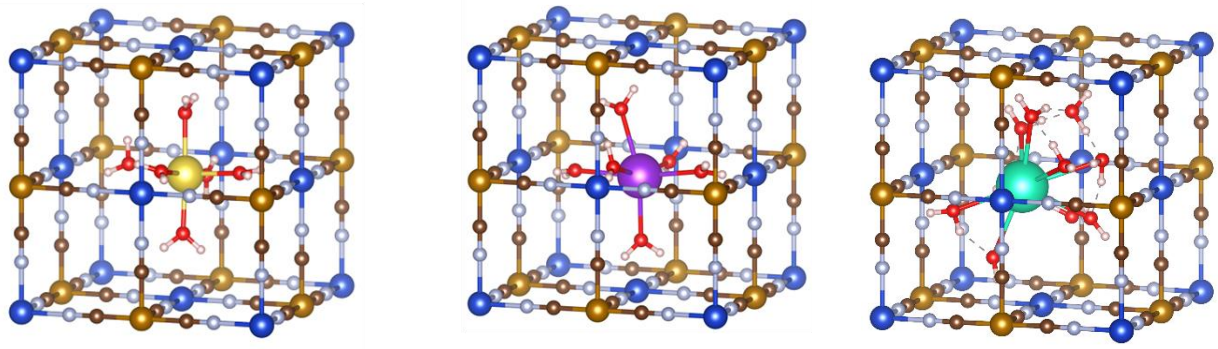

Figure 4-6. Initial configuration of water-alkali complex inside the Cu-HCF of Na-6 water K-6 water and Cs-6 water.

Then, we do ionic relaxation and allow all the ions move to find a final configuration. Figure 4-7 (left to right: Na-6 water K-6 water and Cs-6 water) shows the final configuration of the water-alkali complexes. $Na^+$ remains at the same site as initial configuration. However, $K^+$ and $Cs^+$ move to 8c sites, which agrees with the previous work [49] For $Na^+$ ion, the previous work [49] showed that it favored the 24d site at the face center of one of the small cubic in the whole conventional cell which is different from our configuration. The possible reason is that the work was done in the perfect Fe-HCF framework without a $Fe(CN)_6$ vacancy in the center of the cubic, and the results may also be different in the defected hydrated Cu-HCF. Also, the $Fe(CN)_6$ vacancy site is large enough for Na-water complex to accommodate. For the final configuration, $Na^+$ still coordinates with six water molecules because there is enough space. By contrast, $Cs^+$ is positioned at the corner of the cubic structure, leaving less space for water molecules to bind with it; However, three water molecules can still bind with $Cs^+$ on the edge of the 8c site. In contrast, $K^+$ ions are much smaller than $Cs^+$ ions, making it difficult for them to interact with

water molecules when they are in the 8c sites. Consequently, there are almost no water molecules binding with $K^+$ ions in the final configuration.

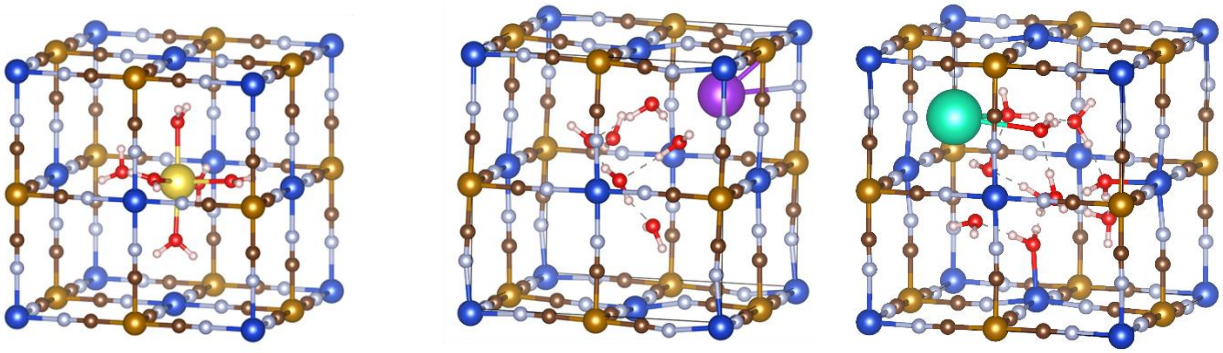

(a) (b) (c)

Figure 4-7. The final configuration of water-alkali complex inside the Cu-HCF of Na-6 water, K-6 water and Cs-6 water.

### 4.3.2 Alkali Ion Incorporation Energy in Hydrated Cu-HCF

In Chapter 3, we concluded that $Cs^+$ ions have the lowest incorporation energy into both perfect and defected Cu-HCF compared to other alkali ions. To determine whether this conclusion still holds in hydrated Cu-HCF, we calculated the ion incorporation energy for $Na^+$, $K^+$, and $Cs^+$. As a reference state for $Na^+$, $K^+$, and $Cs^+$, we surrounded each alkali ion with six water molecules to ensure that the number of water molecules around the alkali ions in the outside solvent is equivalent to the number of water molecules inside the Cu-HCF framework. Incorporating alkali ions into hydrated Cu-HCF requires only one extra step compared to non-hydrated Cu-HCF: forming a water-alkali bond inside the Cu-HCF framework. Bond formation results in a release of energy, which leads to a decrease in the system's energy. Therefore, we can predict that the presence of water inside the hydrated Cu-HCF should have a positive effect on alkali ion incorporation, as it lowers the incorporation energy. The difference in incorporation energy between the hydrated Cu-HCF and non-hydrated Cu-HCF system is the total binding energy between the water molecules and the alkali ions in the hydrated Cu-HCF. For instance, in

the $Na^+$ incorporation system, this energy difference corresponds to the binding energy between six water molecules and $Na^+$. Figure 4-8 shows the absolute value of binding energy between different number of water molecules and alkali ions in the empty simulation box.

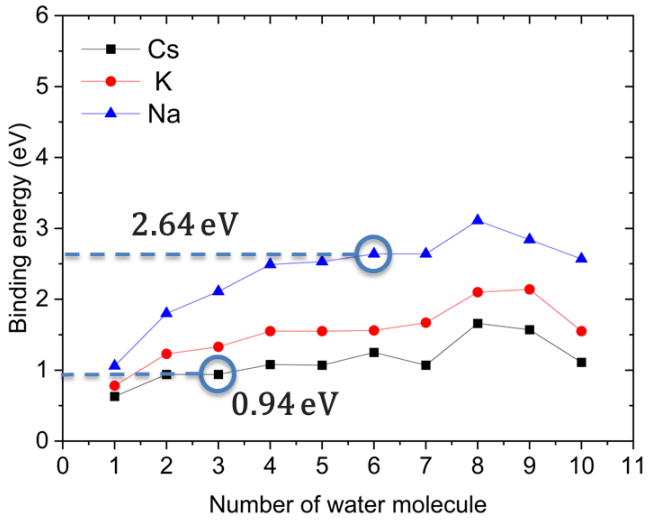


Figure 4-8. Absolute value of binding energy between different number of water molecules and different alkali ions.

The ion incorporation energy for all three different alkali ions in both hydrated and non-hydrated Cu-HCF is shown in Figure 4-9:

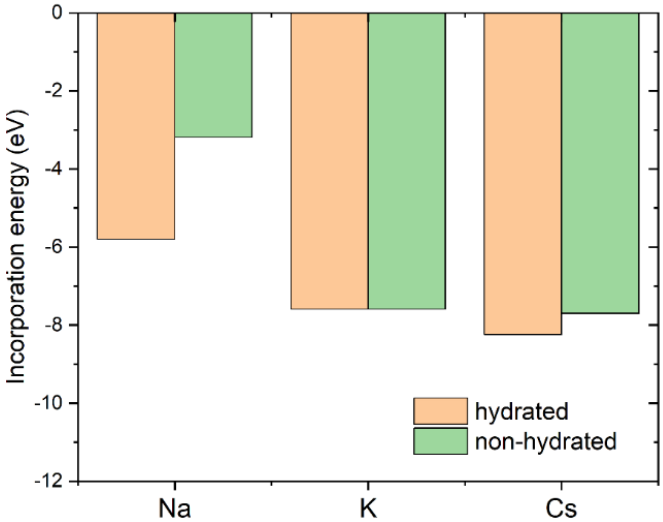


Figure 4-9. Ion incorporation energy for all three different alkali ions in both hydrated and non-hydrated Cu-HCF.

The difference in the incorporation energy between hydrated and non-hydrated Cu-HCF for $Na^+$ is 2.6 eV, which is almost the same as the binding energy between six water molecules, shown in Figure 4.10. As for $K^+$, as we noted earlier, water does not bind with it inside Cu-HCF; so, the incorporation energies are the same for the hydrated and non-hydrated Cu-HCF. In the case of $Cs^+$, three water molecules bind with it inside the Cu-HCF framework, and the energy difference should correspond to the total binding energy between the three water molecules and Cs which, from Figure 4.10, is 0.94 eV. However, our calculations show this difference to actually be 0.46 eV, which is not what we expected. The possible reason is that $Cs^+$ is larger than $K^+$ and $Na^+$. There might be some other interactions between $Cs^+$ and framework we need to address in the future.

### 4.3.4 Alkali Ion Exchange Energy in Hydrated Cu-HCF

The ion exchange energy of $Cs^+$-$Na^+$ and $Cs^+$-$K^+$ ions in the hydrated system involves two additional steps compared to the non-hydrated system. First, the host alkali ion breaks the bond with water molecules inside Cu-HCF and moves outside to form a bond with solvent water molecules. Second, the $Cs^+$ ions break the bond with water molecules in the solvent and incorporate into Cu-HCF, forming bonds with water molecules inside the structure. Taking $Cs^+$-$Na^+$ exchange as an example, the difference in incorporation energy between the hydrated and non-hydrated Cu-HCF systems is given by Equation 4-5:

$$E_{difference} = (E_{CuHCF\_Cs\_6H_2O} - E_{CuHCF\_Cs}) + (E_{CuHCF\_Na} - E_{CuHCF\_Na\_6H_2O}) \quad (4\text{-}5)$$

$E_{difference}$ is the ion exchange energy difference between hydrated and non-hydrated Cu-HCF systems. $E_{CuHCF\_Cs\_nH_2O}$ and $E_{CuHCF\_Na\_nH_2O}$ is the energy of hydrated Cu-HCF with $Cs^+$ or $Na^+$ ion and 6 water molecules inside the structure. $E_{CuHCF\_Cs}$ and $E_{CuHCF\_Na}$ is the energy of non-hydrated Cu-HCF with $Cs^+$ or $Na^+$ ion. In other words, this energy difference equals the

energy difference between $Cs^+$ hydration (negative value) and $Na^+$ dehydration (positive value) with water molecules, that is, the energy difference between water-$Cs^+$ binding and water-$Na^+$ binding. From Figure 4-8 we know that the absolute value of binding energy between water-$Na^+$ and water-$K^+$ is larger than the water-$Cs^+$. This means the exchange energy value difference between hydrated system and non-hydrated system should be positive. In other words, ion exchange in hydrated system is less favorable than in the non-hydrated system. Figure 4-10 shows the ion exchange energy value for $Cs^+$-$Na^+$ and $Cs^+$-$K^+$ in both hydrated and non-hydrated systems.

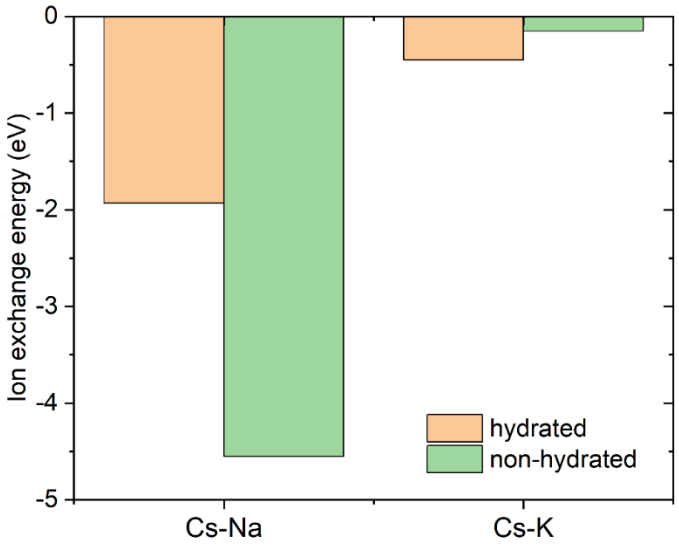


Figure 4-10. Ion exchange energy for $Cs^+$-$Na^+$ and $Cs^+$-$K^+$ in both hydrated and non-hydrated systems.

For $Cs^+$-$Na^+$ exchange, the ion exchange energy value is as predicted. The hydrated system has a more positive value than the non-hydrated system, which means that water molecules inside the Cu-HCF make $Cs^+$-$Na^+$ exchange less favorable. However, for $Cs^+$-$K^+$ exchange, the ion exchange energy for the hydrated system is more negative. This is because there are no water molecules binding with $K^+$ ion, but there are 3 water molecules binding with

$Cs^+$ ion. The whole process only involves $Cs^+$ forming a bond with water, but there is no $K^+$ breaking the bond with water molecules.

## 4.4 Conclusions

In this chapter, we have investigated the distribution of water molecules within the hydrated Cu-HCF framework and their impact on alkali ion incorporation energy and alkali ion exchange energy. Our theoretical calculations suggest that the maximum number of water molecules in the hydrated Cu-HCF is 18. Furthermore, we found that coordinated water is preferred when there is only one water molecule in the framework, whereas zeolitic water molecules are favored when there is more than one water molecule present. Coordinated water molecules will also form due to limited space for zeolitic water when the number of water molecules inside the framework is high. Our results also indicate that $K^+$ and $Cs^+$ ions tend to occupy the 8c sites, while $Na^+$ ions prefer the center of the framework after structural relaxation following alkali ion incorporation. Additionally, we found that water molecules decrease the alkali ion incorporation energy, making it more energetically favorable, and increase the ion exchange energy, making it less energetically favorable.

# CHAPTER 5
# DOPED LaMnO3 FOR WATER SPLITTING BY DENSITY FUNCTIONAL THEORY CALCULATIONS

## 5.1 Background

Perovskite oxides ($ABO_3$) are emerging as candidates for STCH applications. The perovskite structure is ubiquitous with many different A and B combinations and a variety of different crystallographic structures [61]. Moreover, perovskites can often accommodate a wide range of isovalent and aliovalent doping on both the A and B sublattices at significant concentrations, charge compensated by oxygen vacancies if required.[62]. Scheffe and coworkers have identified Sr-doped lanthanum manganate, $La_{1-x}Sr_xMnO_{3-x}$, as a candidate material for near-isothermal water splitting. Given the compositional richness of the perovskite system, it likely that there are other compositions that also have favorable properties. [14]

Emery et al.[63] used high-throughput DFT methods to screen 5329 perovskite compositions for water splitting applications. By applying stability and oxygen vacancy formation energy filters, they identified 383 candidates for further study. However, this study only considered pure perovskite compositions without any doping. Scheffe et al. have demonstrated that doping is a practical way to improve perovskite performance [13,14]. Gopalakrishnan et al. have also screened Ce-based A and B-sites doped perovskites and found that larger reduction entropy can improve STCH efficiency [64]. Doping can increase the number of B-sites elements that are reduced during oxygen vacancy generation, thereby increasing the reduction entropy.

Starting from the case of $A^{3+}B^{3+}O_3$, the work is motivated by three observations: (1) Monovalent alkali elements and divalent alkaline earth elements can be used to substitute on the A-sites of perovskites. Doping these elements onto the A-sites can increase the configurational entropy, which may benefit the reduction reaction. Such aliovalent doping can

increase the capacity of oxygen off-stoichiometry during the reduction process. For example, pure $LaMnO_3$ can only accommodate one oxygen vacancy for every two formula units, with $Mn^{3+}$ reduced to $Mn^{2+}$. When alkali or alkaline earth elements are doped onto the A-sites, more oxygen vacancies can be formed because there are some $Mn^{4+}$ on the B-sites; the reduction from 4+ to 2+ in Mn results in a greater reduction in entropy than the reduction from 3+ to 2+[64]. Doping also changes the coordination environment for the oxygen vacancies, which can impact the oxygen vacancy formation energy. This suggests that it may be possible to control the energetics of oxygen vacancy formation by doping with different elements.

(2) Group III elements such as Ga, Al, and In can substitute on the B sites of perovskites. Previous studies have shown that Ga and Al doping into B-sites of several Mn-based A-sites substituted perovskites can improve the peak $H_2$ production rate [65]. Therefore, we expect that single dopants on B-sites with these group III elements can also make a difference. Although these group III elements have the same oxidation state as Mn, they can still increase the configurational entropy, which may lead to increased oxygen off-stoichiometry. We did not consider the other 3+ lanthanides due to their small size. We also examined two +2 elements, Mg and Zn, on the B sites as they can enhance reduction by creating higher valence B-sites elements. Similar to A-site substitution, this substitution may increase the configurational entropy and oxygen off-stoichiometry capacity, which has not been systematically explored yet.

(3) While previous studies have made predictions about the stability of the compositions they have investigated, they have not identified the specific temperature and oxygen partial pressure ranges in which these compositions remain stable.

Therefore, this study aims to investigate doping on the A and B lattices starting from the $LaMnO_3$ composition. To identify compositions with potential interest for splitting, we apply

two criteria. Firstly, candidate compositions must exhibit stability over the temperature range of room temperature to 1500˚C, with particular emphasis on high-temperature thermodynamic stability due to rapid decomposition kinetics. We are less concerned with thermodynamic stability at low temperatures, as many thermodynamically metastable compositions may be kinetically stable. The second criterion is that candidate compositions must have oxygen vacancy formation energies within the range of 2.5 eV to 4 eV. The lower bound is sufficient for water splitting, while the number of oxygen vacancies produced if the formation energy is above 4 eV may be impractical for water splitting. We investigated LaMnO3 doped with K, Rb, Cs, Mg, Ca, Sr, and Ba on the A sites, as well as Mg, Zn, Al, Ga, and In on the B sites. Our results show that LaMnO3 A-site substituted with Mg, Ca, Sr, and Ba and B-site substituted with Al, Ga, and In meet these two criteria, making them potential candidates for solar-thermal water splitting applications.

## 5.2 Methodology

### 5.2.1 Density Functional Theory (DFT) Calculations

The phase stability and the oxygen vacancy formation energy are calculated using density functional theory (DFT) in the Vienna ab initio Simulation Package (VASP) [18,19] with projector augmented waves (PAW) pseudopotentials [41,42]. The Fitted Elemental-phase Reference Energies (FERE) are used to calculate heats of formation and in defect formation energy calculations [22]. The generalized gradient approximation (GGA) is chosen to approximate the exchange–correlation energy with the Perdew–Burke–Ernzerhoff (PBE) functional [43]. The following PAW datasets of the VASP distribution 4.6 distribution were used, “Mn, O_s, Li_sv, Na_pv, K_sv, Rb_sv, Mg_pv, Ca_pv, Sr_sv, Ba_sv, Al, Ga_d, In_d, Zn”. The GGA + U method [66] is applied to the transition metal Mn with U-J = 3.0 eV for the *d*-orbital electrons. For lanthanum, we used the PAW dataset “La” of the VASP 5.4 distribution and determined the

FERE as -3.75 eV with U-J = 2.0 eV for the *f*- and 1.5 eV for the *d*-electrons. After convergence tests, we use a cutoff energy to be 340 eV and a 4 × 4 × 4 Monkhorst–Pack k-point mesh for all the calculations [67]. Spin polarization is also included in our calculations. We considered both Ferromagnetic (FM, black) and Anti-Ferromagnetic configurations (AFM, blue) and found that the results are very close to each other, as is illustrated in Figure 5-1.

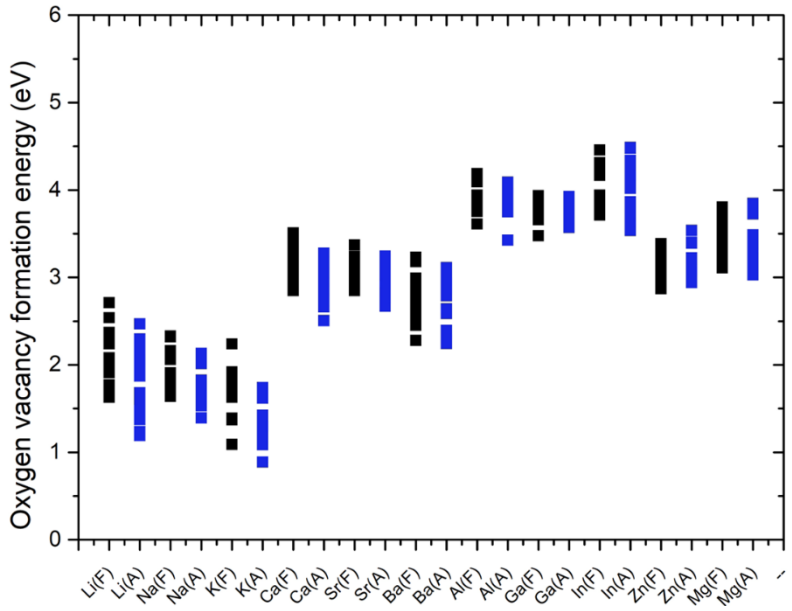


Figure 5-1. Oxygen vacancy formation energy for FM and AFM configurations.

### 5.2.2 Bulk Calculations

We determine the ground state structure of $LaMnO_3$ from among the following space groups: Pnma (62, orthorhombic), $Pm\bar{3}m$ (221, cubic), $R\bar{3}c$ (167, trigonal) and $P6_3/mmc$ (194, hexagonal). A 2x2x2 supercell is created for the cubic structure (7.9Å x 7.9Å x 7.9Å, 40 atoms), a 2x1x1 supercell (11Å x 5.9Å x 7.8 Å, 40 atoms) for the orthorhombic, a 1x1x1 supercell (30 atoms) for the trigonal, and a 2x2x1 supercell (6.8Å x 6.8Å x 12.4Å, 40 atoms) for the hexagonal structure. Figure 5-2 shows DFT total energy per LaMnO3 formula unit of three different structures relative to the orthorhombic structure. Green atoms are La, purple atoms are Mn and

red atoms are O. As Figure 5-2 shows, the Pnma orthorhombic structure has the lowest energy which is marked with black dash line and will be used for all subsequent calculations.

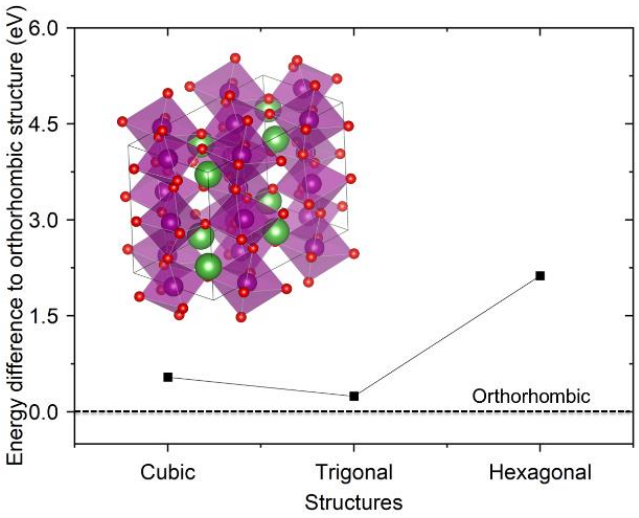


Figure 5-2. DFT total energy per $LaMnO_3$ formula unit of three different structures relative to the lowest energy, orthorhombic structure

### 5.2.3 Structure of substituted Systems

Based on Scheffe et al.' s experimental substitution for $La_{1-2x}Sr_{2x}MnO_{3-x}$ of 2x=0.35, and on the 20-atom Pnma unit cell, we use a 2x1x1 supercell (11Å x 5.9Å x 7.8 Å, 40 atoms), in which we substitute 3 out of 8 La atoms with group I and group II elements or 3 out of 8 Mn atoms with group III elements or other +2 elements, to give 2x=0.375. Relaxation of all atomic positions and supercell dimensions is performed after the substituted structures are created.

### 5.2.4 Stability Analysis

To determine the stability of substituted $LaMnO_3$, we need to determine DFT total energies for all the binary and ternary compounds to which the specific composition could decompose. We take these values from the materials database from National Renewable Energy Laboratory (NREL) as they use the same DFT functional, cutoffs and meshing as used for our doping calculations. The stability of the substituted quaternary phases $A_xS_wB_yO_z$ is analyzed in

terms of the enthalpies of formation:

$$x\Delta\mu_A + w\Delta\mu_S + y\Delta\mu_B + z\Delta\mu_O = \Delta H_f(A_xS_wB_yO_z) \quad (5\text{-}1)$$

In this equation, $\Delta\boldsymbol{\mu}$ is the change of chemical potential for every element in $A_xS_wB_yO_z$**.** This equation represents the thermodynamic equilibrium condition between the compound and its elemental constituents. The requirement that the alloy structure be stable against decomposition is that [22]

$$l_i\Delta\mu_A + m_i\Delta\mu_S + n_i\Delta\mu_B + q_i\Delta\mu_O \leq \Delta H_f(A_{l_i}S_{m_i}B_{n_i}O_{q_i}) \quad (5\text{-}2)$$

Using these equations, the range of oxygen chemical potential values as which the doped system is stable is determined. The oxygen chemical potential is given by

$$\Delta\mu_O = \frac{1}{2}\left[H_0 + 3.5k_B(T - T_0) - TS_0 - 3.5k_B\ln\left(\frac{T}{T_0}\right)\right] + \frac{1}{2}k_BTIn\left(\frac{P}{P_0}\right) \quad (5\text{-}3)$$

Equation 5-3 generated by the ideal gas law in which the entropy of oxygen has been considered. We use the tabulated values for the $O_2$ standard [68], $H_0 = 8.7KJ\ mol^{-1}$, $S_0 = 0.21KJ\ mol^{-1}K^{-1}$ , $T_0 = 298K$, $P_0 = 1\ atm$, $k_B$ is Boltzmann constant. T and P are the temperature and oxygen partial pressure. Equation 3 can then be used to determine the domain of temperatures and oxygen partial pressures in which the system is stable. [69] We are ignoring the entropy to the solid components. The finite temperature impacts on the stability analysis have been reported before [22] and it did not have significant impact on the result. Also, the entropy impact can be largely cancelled out when we compete between two different phases.

### 5.2.5 Oxygen Vacancy Formation Energy Calculation

For substituted structures, an oxygen vacancy is created to calculate the vacancy formation energy. The first nearest-neighbor atoms to the vacancy or substitutional site are randomly displaced (~0.1 Å) to break the underlying site symmetry and thereby, ensuring that non-symmetric configurations of the defects are properly captured. [23] Various physical configurations

of substituted sites and sites with unique oxygen vacancies are considered, as discussed below. In all cases the structure is full optimized. The 2x1x1 supercell is used to calculate vacancy formation energy.

## 5.3 Results and Discussions

### 5.3.1 Doped Perovskites

We create doped systems based on the orthorhombic $LaMnO_3$ structure with 40 atoms in the supercell. For La sites, we substitute with group I (Li, Na, K, Rb) and group II (Mg, Ca, Sr, Ba) elements. For Mn sites, we substitute with group III (Al, Ga, In) and group II (Zn, Mg) elements. Since we substitute 3 of the 8 La or 8 Mn sites the supercell, there are 8!/5!3! = 56 possible different arrangements of La and dopant. Fortunately, many of these are crystallographically identical in the orthorhombic structure. Crystallographic analysis, confirmed by single point calculations, shows that there are actually only 5 distinct arrangements of the 3 dopants for both La-sites and Mn-sites. These are illustrated in Figure 5-3. A1-A5 shows 5 distinct A-sites substituted configurations and B1-B5 shows 5 distinct B-sites substituted configurations. For clarity, only A atoms is shown for A-sites substituted configurations and only B atoms is shown for B-sites substituted configurations. The normalized dopants substitution energies of these five different arrangements are shown in Figure 5-4 (Sr, Li for A-sites and Al, In for B-sites) which is following the equation:

$$E_{sub} = (1/3)[E_{substituted\_structure} - E_{unsubsituted\_structure} + 3 \times (\mu_{previous\ lattice\ atom} - \mu_{dopant})] \quad (5\text{-}4)$$

where, $E_{sub}$ is the substitution energy, $E_{substituted\_structure}$ is the final energy after substitution, $E_{unsubsituted\_structure}$ is the initial structure without ion substitution, $\mu_{previous\ lattice\ atom} - \mu_{dopant}$ is the chemical potential difference between the dopants and the previous lattice atom. For both Sr and Li A-sites substituted structure. In both cases, the

difference between the highest and the lowest energy configurations is less than 0.25 eV per $LaMnO_3$ formula. Since we have already captured all the distinct configurations by symmetry in figure 5-3, we do not need a larger supercell to capture any other new configurations.

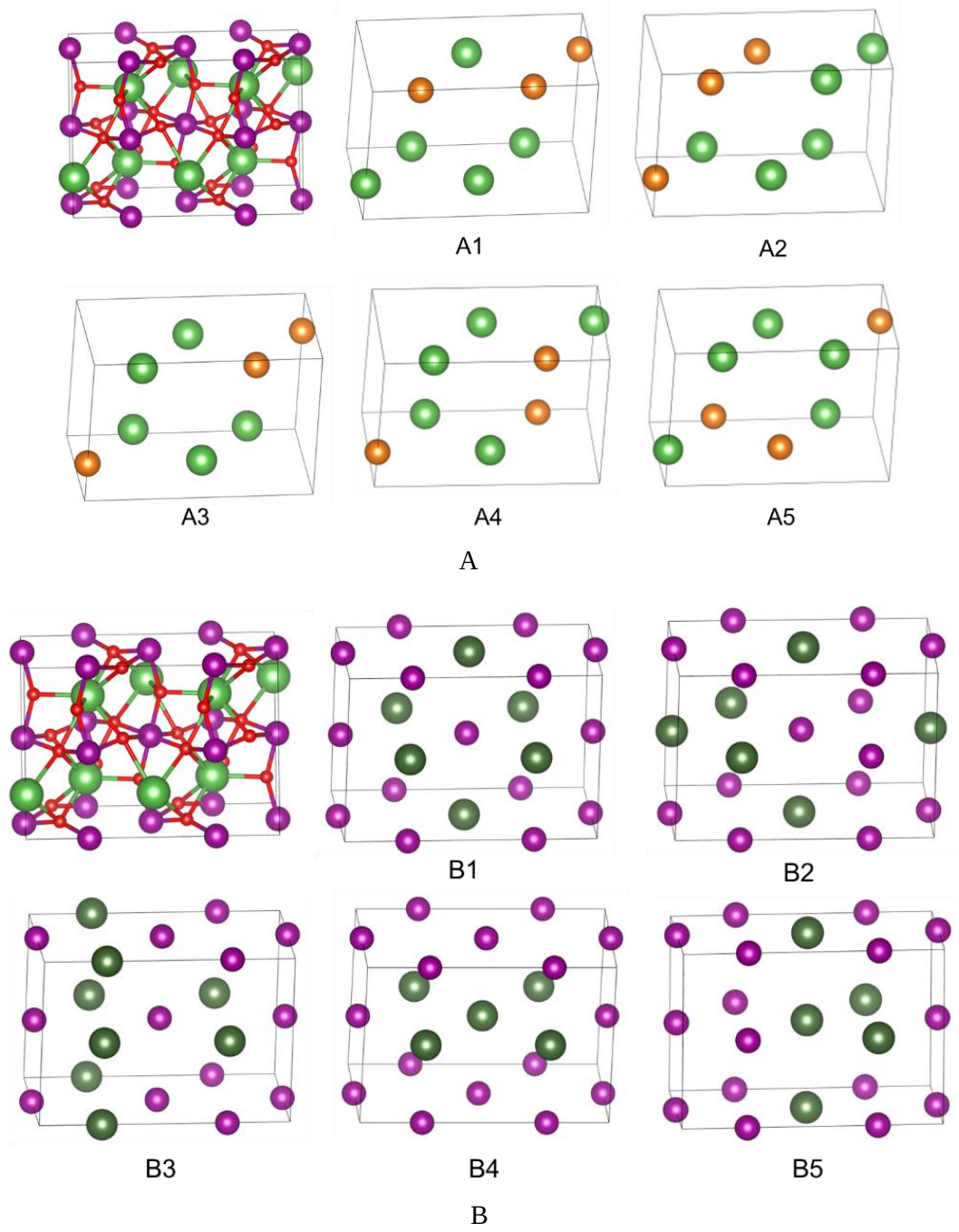


Figure 5-3. Original La(A)-sites and Mn(B)-sites in orthorhombic supercell and crystallographically distinct arrangements for A and B substitutions.

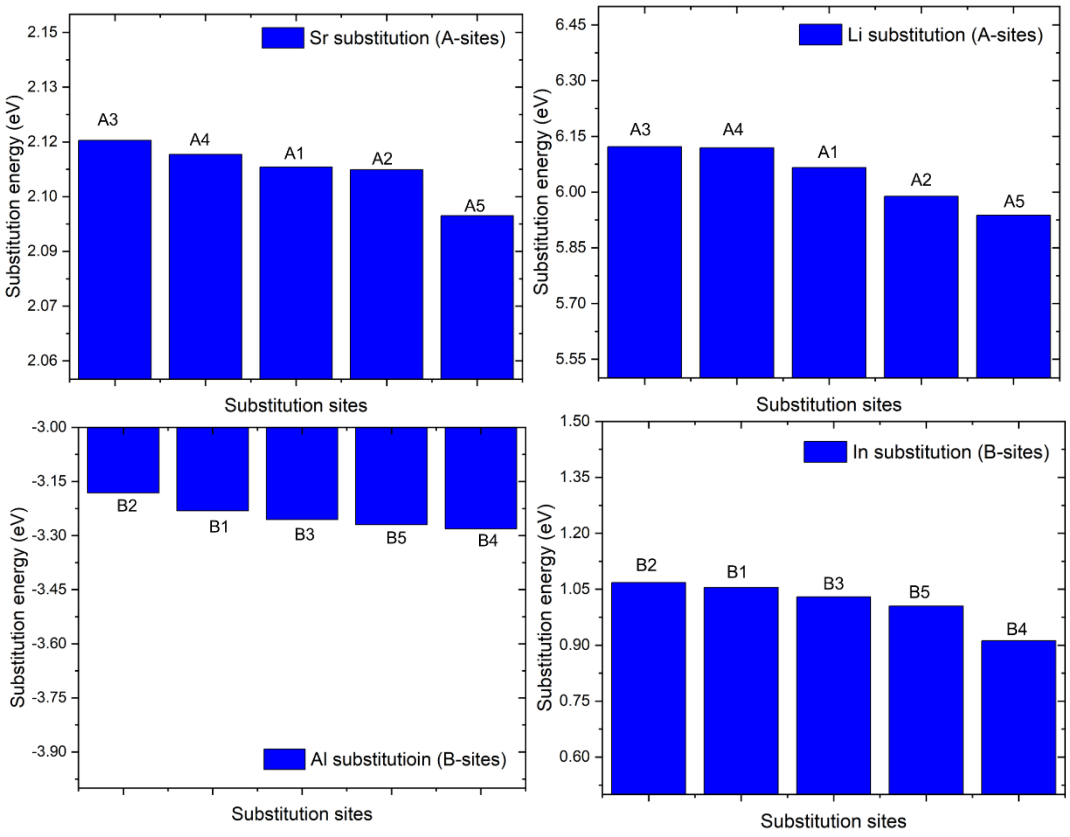


Figure 5-4. Substitution energy for Sr, Li and Al, In at various combinations of sites in $LaMnO_3$.

To evaluate the impact of different configurations on oxygen vacancy formation energy values, we calculate vacancy formation energies of the five unique configurations of the dopants and for all the unique oxygen sites around these dopants for Sr and Li substitution on the A site. As Figure 5-5 shows, for each of the five configurations of cation dopants, there is a relatively wide range of values of the oxygen formation energy. However, these ranges are reasonably similar for all five cation configurations. Moreover, since our aim is to merely identify candidate compositions with defect formation energies in the window of 2.5 to 4.0 eV, we conclude that we do not need to calculate the oxygen vacancy formation energy based for all of the different cation configurations. The lowest energy and highest energy configurations may reflect the most ideal conditions or the worst conditions, respectively. We will choose the configuration with the

middle value of substitution energy to perform all subsequent calculations, as this will represent the average level of stability and oxygen vacancy formation energy results under different conditions. Thus, for the other A-substitution, we just choose one configuration A1, for which the oxygen formation energies are marked red in Figure 5-5 to represent all other configurations in the following stability analysis and oxygen vacancy formation energy. For all the B-substitution, we just choose one configuration B3, for which the oxygen formation energies are marked red in Figure 5-5. For the case of Li, while there are some points in the range of 2.5-4.0 eV, most are below 2.5 eV, meaning that this is not a good candidate material for water splitting. For Al and In, although some of the points are higher than 4.0 eV, however, they others are still between 2.5-4.0 eV which means we can still take them into our consideration.

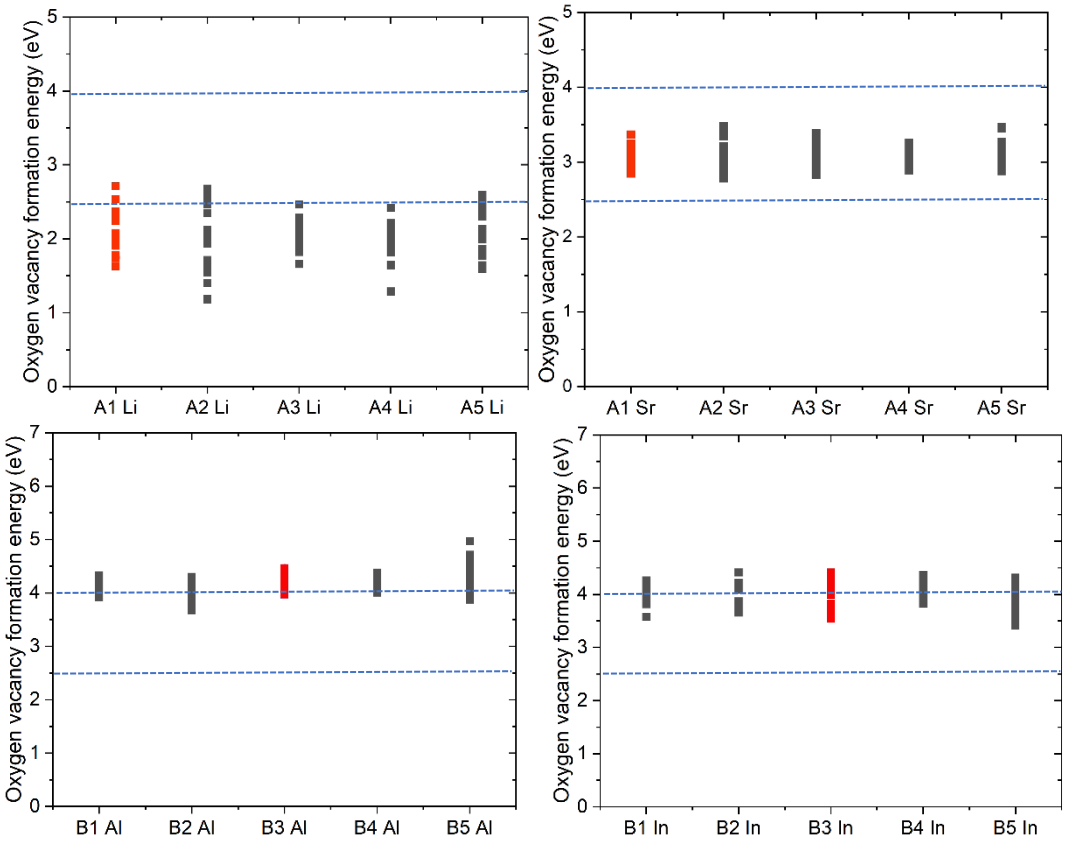


Figure 5-5. Oxygen vacancy formation energy under unique five configurations for Li, Sr, Al and In substituted structures.

### 5.3.2 Binary Phase Stability

We first validate our methodology for phase stability by performing stability analysis for a binary material and a ternary material before finally moving to the quaternary substituted compositions. For the binary compositions, we select manganese oxides as our starting point. In two dimensions, the Eq. 5-1 yields relationships $\Delta\mu_O$ and $\Delta\mu_{Mn}$ relationships for the various oxides phase diagram in Figure. 5-6:

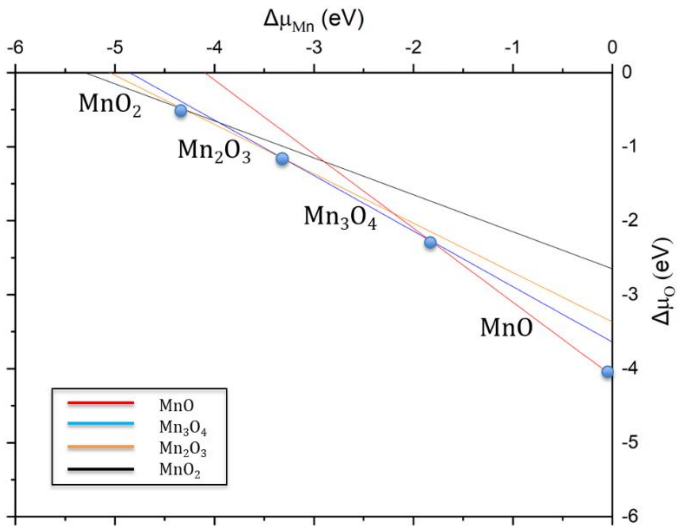


Figure 5-6. Phase diagram of Mn oxides in $\Delta\mu_O$ and $\Delta\mu_{Mn}$ space.

Thus, different Mn oxides are stable within different range of $\Delta\mu_O$. Applying Eq. 5-3, for each $\Delta\mu_O$ value, we can plot the relationship between temperature and oxygen partial pressure. This results in a phase diagram in oxygen partial pressure (P) and temperature (T) space [69]. Figure 5-7 (a) show the resulting phase diagram. We can compare the predicted stability line between Mn and MnO with the published Ellingham diagram. [70]. Figure 5-7 (b) shows our predicted P-T value and Ellingham values. As we expect, for high temperatures and low oxygen partial pressures, metallic Mn is stable. As the temperature decreases and/or the oxygen partial pressure increases, the manganese is progressively oxidized to form MnO, $Mn_3O_4$, $Mn_2O_3$ and

finally $MnO_2$. The predicted temperature and pressure of the oxidation of Mn to MnO can be compared to the well-established Ellingham diagram. The difference between the DFT calculations and the experimental Ellingham diagram is around 50 K, which can be explained by the known limitations in the accuracy of DFT calculations, typically up to a few tens of meV energy. We cannot find a higher oxygen partial pressure because the highest partial pressure value in the Ellingham diagram is somewhere between $10^{-12}$ and $10^{-10}$ atm. Figure 5-7 (c) shows the error between our predicted value and Ellingham values.

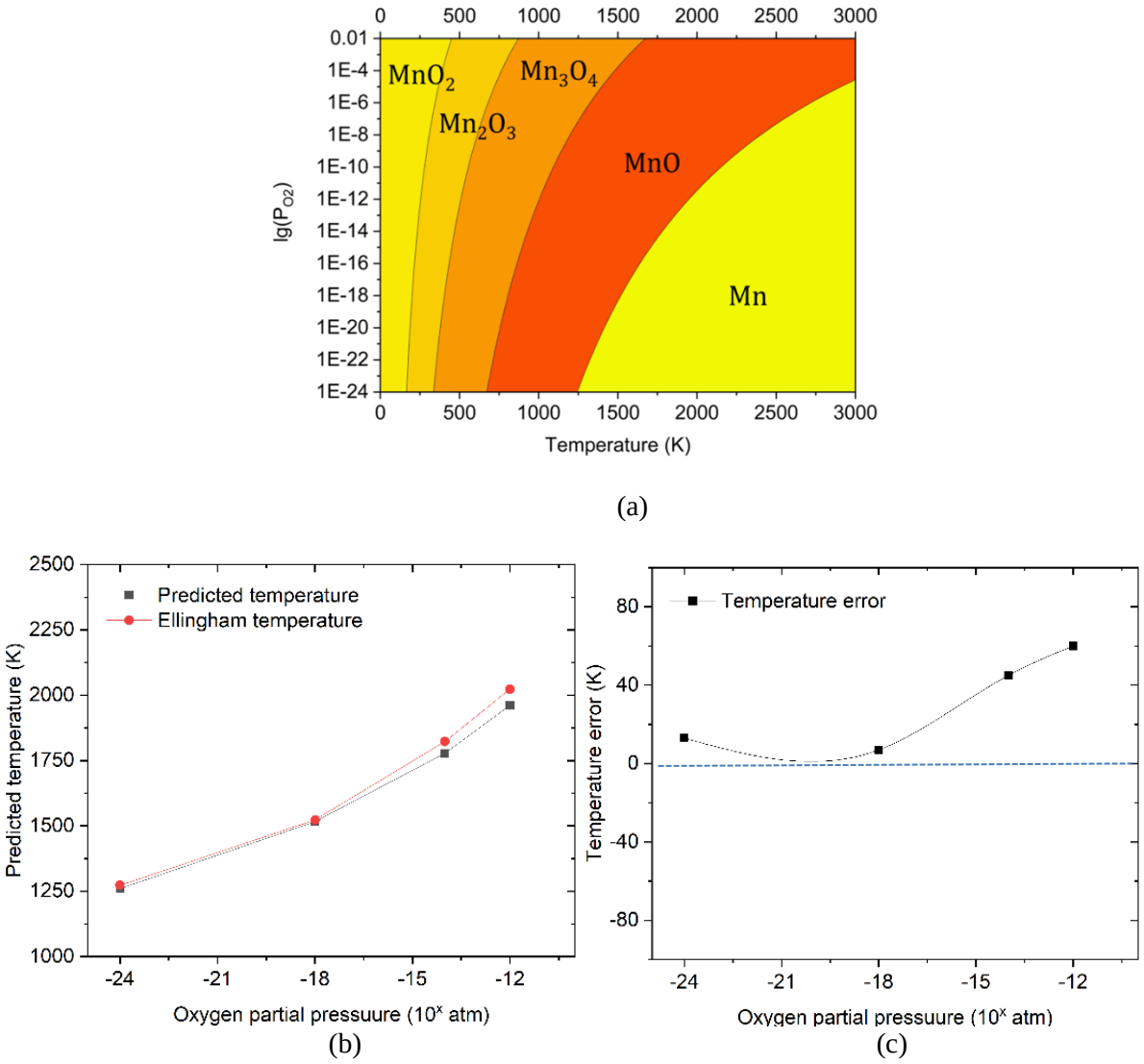


Figure 5-7. predicted phase diagram in P and T space, the Ellingham P-T value and the error between predicted value and Ellingham values

From the trend in Figure 5-7 (c), we expect the error between DFT predicted values and experimental values to range from 0-50 K as the pressure increases. With equation 5-1, we can get $\Delta\mu_O$= -4.837 eV under $10^{-12}$ atm oxygen partial pressure based on the Ellingham predicted temperature and $\Delta\mu_O$= -4.680 eV based on our predicted temperature range. The error is about 0.153 eV which is reasonable compared to the error given by FERE method which is 0.05 eV/atom. [22] We do not need to concern about the error trends in Figure 5-7 (c) that the error may be crazy large when we increase the oxygen partial pressure to be as high as $10^{-6}$ to $10^{-4}$ atm. The reason is that DFT is a 0 K method and all the calculations here are in MnO which will not change DFT error at all. The temperature error between our predicted value and Ellingham value will be about 60 K when we transfer 0.153 eV $\Delta\mu_O$ difference to temperature difference under $10^{-4}$ atm. Based on this, we are confident that our methodology can give good prediction on stable temperature window of a given system.

### 5.3.3 Ternary Phase Stability

The approach to analyzing the ternary system is identical to that of the binary system, but in three dimensions of chemical potential space. However, using Eq. 1 we can determine $\Delta\mu_O$ in terms of $\Delta\mu_{La}$ and $\Delta\mu_{Mn}$, thereby reducing the three dimensions to two dimensions of chemical potentials space. This makes it easier to visualize and to analyze. The resulting phase diagram in $\Delta\mu_{La}$ and $\Delta\mu_{Mn}$ space in Figure 5-8 (a) show the stable $LaMnO_3$ phase as well as other neighboring phases. The stable $LaMnO_3$ phase will be in the range of $\Delta\mu_O$ =-2.959 eV to -0.391 eV. Again, we can transform from $\Delta\mu_O$ space to $pO_2$ and T space, enabling us to identify the stable $LaMnO_3$ region as a function of temperature and partial pressure. Figure 5-8 (b) shows the range of stability of $LaMnO_3$ in P and T space. In the $p_{O2}$ range of $10^{-3}$ -$10^{-6}$ atm, which is applicable to water splitting, $LaMnO_3$ is the stable phase from ~250 K to more than 2000 K. This

lower limit is not a concern since although $LaMnO_3$ may be thermodynamically unstable at low temperatures it is likely kinetically stable. This finding is in accord with the previous study which demonstrated stability up to the highest temperature explored, which was 1800 K. [71]

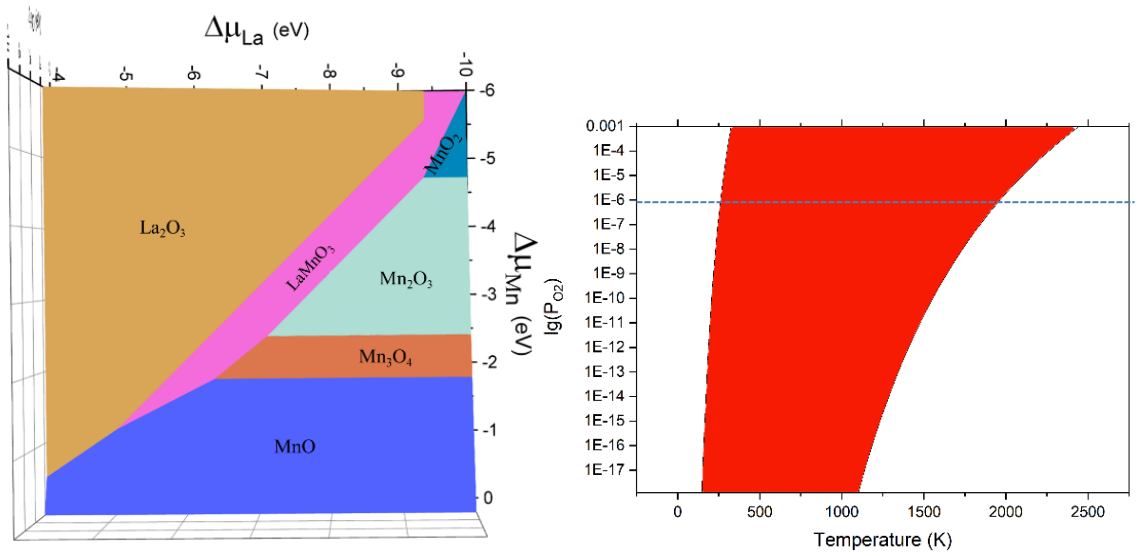


(a) (b)

Figure 5-8. Phase diagram of La-Mn-O ternary system projected in $\Delta\mu_{Mn}$ and $\Delta\mu_{La}$ space and stability region of $LaMnO_3$ in oxygen partial pressure and temperature space.

### 5.3.5 Quaternary Phase Stability

We follow the same approach to the quaternary La-A′-Mn-O and La-Mn-B′-O phase stability analysis where A′ and B′ are substituted on the A and B sites respectively. The 4-dimensional phase diagram cannot be visualized 2D. However, we can still determine the range of $\Delta\mu_O$ value that for which the substituted $LaMnO_3$ is stable by Equations 5-1 and 5-2 and then transfer that to P, T space by Equation 5-3 to identify the stable temperature window. Figure 5-9 shows the P-T phase diagram of Sr substituted and Al substituted $LaMnO_3$. Sr substitution case is on the left site and Al substitution case is on the right site.

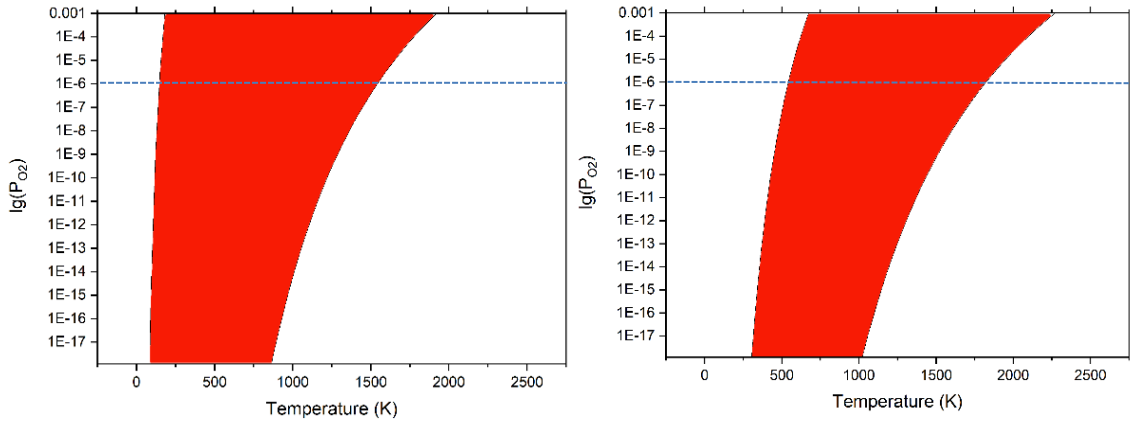


Figure 5-9. Stability region of substituted $LaMnO_3$ in oxygen partial pressure and temperature space

The black bars in Figure 5-10 show the temperature window predicted under $10^{-4}$ atm (experimental condition in reduction process) oxygen partial pressure to give stable substituted phases.

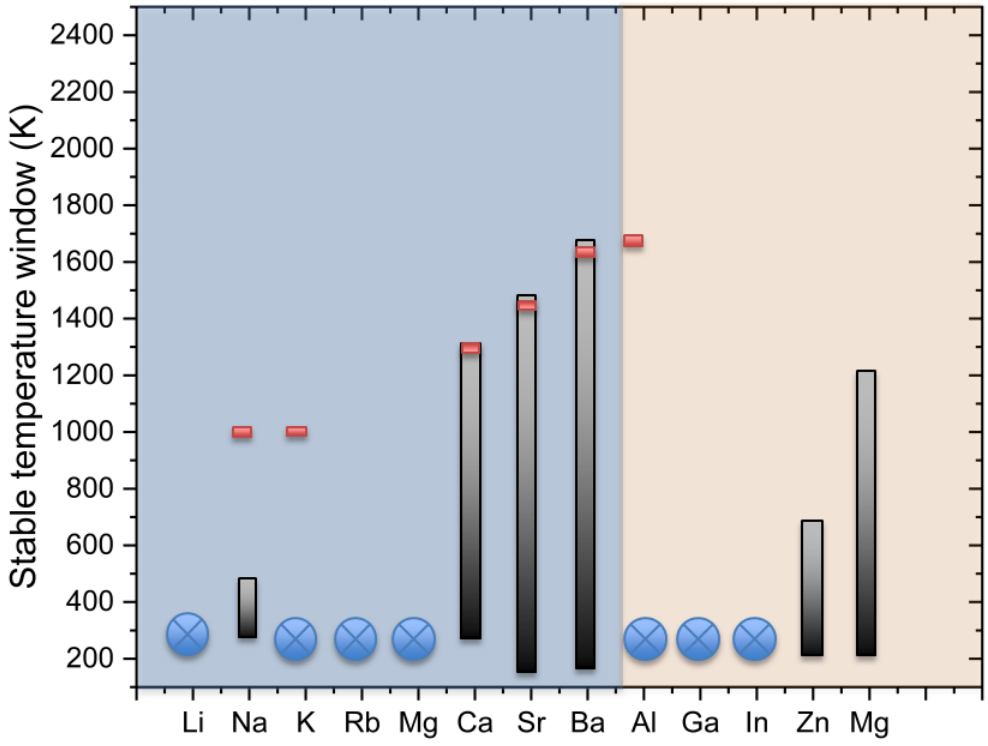


Figure 5-10. Predicted temperature window under $10^{-4}$ atm oxygen partial pressure of substituted $LaMnO_3$ compared to their working temperatures in previous literature [12,72–75]

Left part with blue background is the composition with A-sites substitution and the other orange part is the composition with B-sites substitution; Black bars the predicted stability window and short red bar are experimental working temperatures. Compositions indicated by blue circles are predicted to be unstable. The blue circle denotes compositions that are not predicted to be stable. The orange bars denote temperature ranges over which these materials have been shown experimentally to be stable. It can be safely presumed that these materials are also stable at lower temperatures. Moreover, the experiments were not designed to determine the upper stability temperature, so it is likely that they are stable up to somewhat high temperatures also, although the precise limits are not known. Thus, the actual range of stability may be much wider. The computational results are consistent with the experimental results for the Ca, Sr and Ba substituted systems. However, in four cases there is qualitative disagreement in that the experiments predict stability at 1000 K or more whereas the calculations predicts either a much lower maximum stability temperature (Na), or that the quaternary will be unstable (K, Al, Ga). Possible reasons for this disagreement may be:

(1) Some of the substituted structure recorded by previous literature is not for water splitting applications and their working oxygen partial pressure is at 1 atm which is much higher than what we used in the water splitting application. As can be seen from Fig. 5-8b, the upper limit of the stability range decreases markedly with decreasing partial pressure.

(2) PBE level DFT calculations have well-documented limits to their precision. To probe the discrepancy in terms of the precision of the DFT results, we consider the degree of instability of these systems, specifically how far they lie above the convex stability hull. It is well-established that DFT is not perfect in predicting stability. For example, there are a large

number of compositions and structures in the Materials Project database that lie above the convex hull yet are experimentally observed. This may indicate either that the materials are metastable or that the DFT calculations have limited precision. As a result, it has been taken as a rule of thumb that structures with energies of less than ~70 meV/atom above the convex hull may be experimentally relevant.[76] Therefore, to ensure that we do not miss any possible candidates, all compositions with DFT energies that is70 meV and less higher than the convex hull energy will be kept. Using that correction, we re-examine those structures that were found to be unstable

Table 5-1. Total energy per atom difference between our calculated value and theoretical highest value that make the phase stable.

| | Al | Ga | In | Li | K | Rb | Mg |
|---|---|---|---|---|---|---|---|
| Calculated total energy per atom (eV) | -7.944 | -7.671 | -7.581 | -7.383 | -7.326 | -7.276 | -7.499 |
| Convex hull (eV) | -7.945 | -7.680 | -7.5854 | -7.3999 | -7.327 | -7.310 | -7.575 |
| Energy difference (meV) | 1.0 | 9.0 | 4.4 | 17 | 1.0 | 34 | 76 |
| Stable T with convex hull energy (K) | 550-1800 | 650-1200 | 250-2000 | 200-250 | 300-650 | 250-650 | 250-850 |

As Table 5-1 shows, for four of the seven cases predicted to be unstable, most of the DFT calculations predict the structures to lies less than 20 meV above the convex hull. Taking this error into consideration by adjusting the energy to lie precisely on the convex hull, we recalculate the stable temperature window for these predicted to be unstable and compared them with previous works, as shown in Figure 5-11. This now shows temperate ranges of stability for Al and Ga in Figure 5-11, which now bring the DFT analysis to consistency with experiment for nearly all compositions. For all the group I substituted compositions, they have low upper stability temperatures and are be ruled out. Most of group II and III substituted structures result in upper stability temperatures as high as 1300-2000 K. For Ga and Al case, the lowest stable temperature seems to be as high as 500 K. However, the kinetics at these temperatures can be

expected to be relatively slow; thus, it is still worthwhile to analyze them further. Overall, we will keep Ca, Sr, Ba, (A-sites) Al, Ga In and Mg (B-sites) doped compositions for the following oxygen vacancy formation energy calculations.

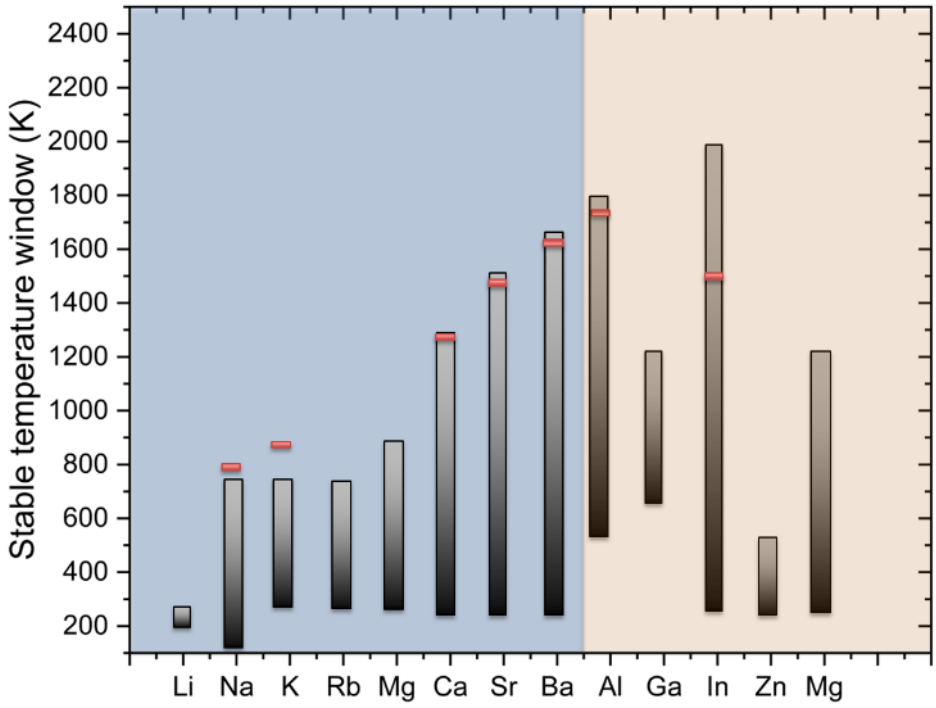


Figure 5-11. Predicted temperature window of substituted $LaMnO_3$ in our work compared to their working temperature in previous literatures after considering the DFT error.

### 5.3.6 Oxygen Vacancy Formation Energy

As demonstrated in Figure 5-5, different dopant arrangements yield similar ranges of oxygen vacancy formation energy. Therefore, it is unnecessary to calculate the oxygen vacancy formation energy for all configurations of all substituted compositions. For all oxygen vacancy formation calculations, configuration A1 will be used for A-site substituted structures, while configuration B3 will be used for B-site substituted structures. We have determined the oxygen vacancy formation energy for all the substituted compositions that we found to be stable in the temperature and pressure range of interest; that is, all the group II element substituted structures and Al, Ga, In Mg substituted structures are analyzed. All the unique oxygen positions for each

of the substituted compositions are considered. For A-sites substitution, that is 16 unique oxygen vacancy configurations for all elements substituted structures. For B-sites substituted structures, there are 12 unique configurations for each element substituted structures. Filtered by the stability criteria, Figure 5-12 shows the vacancy formation energy value for all the potentially stable A and B sites substituted in LaMnO3. Blue background: A-sites substituted compositions, orange background: B-sites substituted compositions. Elements on x-axis means different elements based substituted structures. Blue dash line: 2.5-4.0 eV window; Orange dash line: oxygen vacancy formation energy in pure orthorhombic $LaMnO_3$.

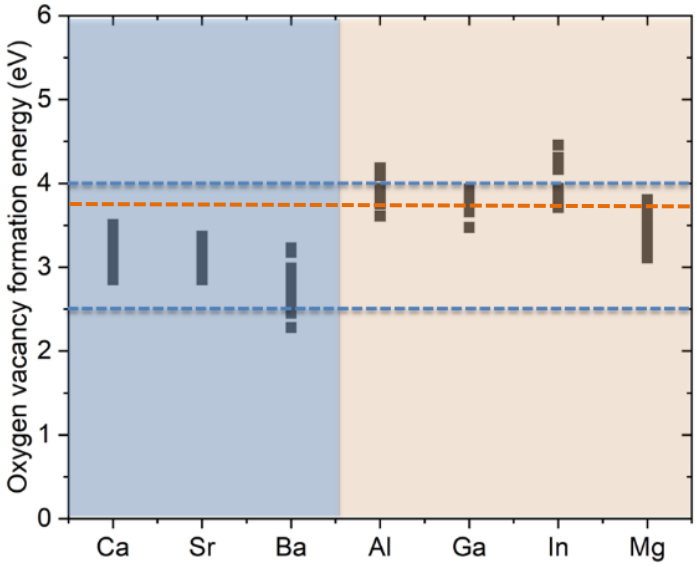


Figure 5-12. Oxygen vacancy formation energy of substituted $LaMnO_3$

Overall, all the of these compositions can produce oxygen vacancy formation energy from 2.5-4.0 eV and can be considered as potential candidates for water splitting applications. From Figure 5-12, we see that the that the 3+ substitutions (Al, Ga and In) have higher oxygen formation energies than the 2+ ions (Ca, Sr, Ba and Mg) To explore whether this trend is general, we also calculated oxygen vacancy formation energies for the unstable structures also, see Figure 5-13. The ratio of $Mn^{3+}$ and $Mn^{4+}$ is given in Figure 5-13 (a). Figure 5-13 (b) shows the oxygen

vacancy formation energy versus the valency of dopants. In figure 5-13 (b), lowest means the lowest oxygen vacancy formation energy among all the compositions under the same valency of dopant; mean indicates mean value of oxygen vacancy formation energy among all the compositions under the same valency of dopant; highest means the highest oxygen vacancy formation energy among all the compositions under the same valency of dopant. All the connection lines are for visual guide.

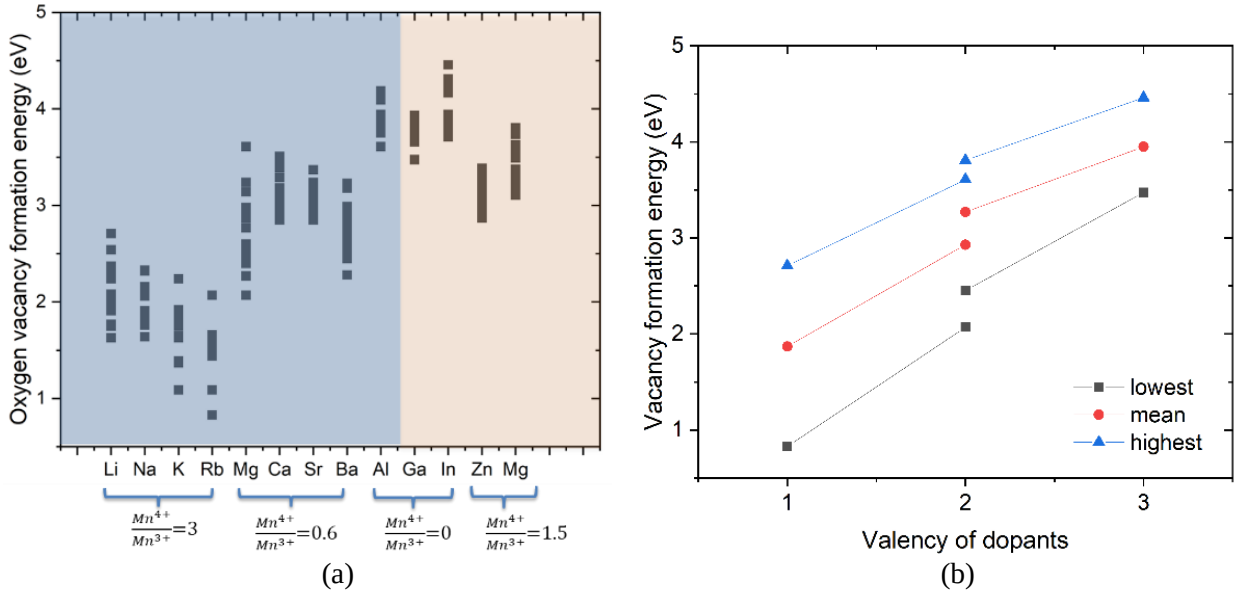


Figure 5-13. Oxygen vacancy formation energy in all substituted compositions and the oxygen vacancy formation energy versus the valency of dopants

There are two different points for 2+ states on Figure 5-13 (b) which reflects both A (lower point) and B (upper point) sites substitution. From Figure 5-13 we see the general trend that the oxygen formation energy increases when moving from valence of the substituting atom of 1+ to 2+ to 3+. There are higher $Mn^{4+}/Mn^{3+}$ values in composition with lower dopant's oxidation states. In other words, the trend is that the oxygen vacancy formation energy increases as the dopant's oxidation state decreases. The electronegativity difference between alkali ions and O is larger than between alkaline earth or 3+ ions and O. The bond strength should follow

this trend and lead to higher oxygen vacancy formation energy in alkali substituted compositions. However, we do not observe this trend in our results, which means we cannot explain our trend by different dopants around oxygen ions in this manner. However, this trend can be explained by considering the electron orbital configurations of Mn d-orbitals, as shown in Figure 5-14.

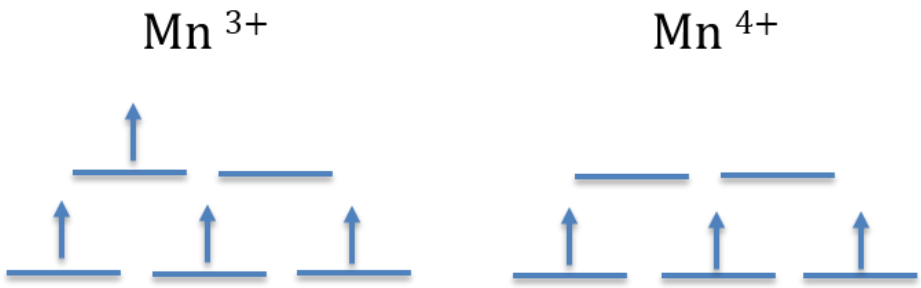


Figure 5-14. Electron orbital configurations of Mn d-orbital.

$Mn^{3+}$ has a half-filled $t_{2g}$ orbital and a single unpaired electron in the $e_g$ orbital. This is not a stable configuration because of the one electron in $e_g$ orbital. By forming a bond with oxygen and sharing the electrons, there will be a half filled $e_g$ orbital which is more stable than the previous unpaired configuration. By contrast, $Mn^{4+}$, has a half-filled $t_{2g}$ orbital and an empty eg orbital, which, is already a relatively stable configuration. This stable configuration will be broken when it shares electrons with oxygen to yield an unpaired electron in the $e_g$ orbital. As a result, the $Mn^{3+}$ will form a stronger bond with oxygen than $Mn^{4+}$. Thus lower a $Mn^{4+}/Mn^{3+}$ ratio results in a higher oxygen vacancy formation energy.

We also found that oxygen vacancy formation energy for different oxygen positions is different, even in the same substituted composition. This is closely related to the coordination environment of oxygen vacancy sites. If the difference in the electronegativity of the oxygen and the cations to which it coordinates is larger, the bond will be stronger yielding a higher oxygen vacancy formation energy. An example of this can be seen from group II elements A-sites

substituted structures; Figure 5-13 (a) shows that Ca and Sr substituted structures have a narrower range in oxygen vacancy formation energy values than Ba and Mg substituted structures. This is because the electronegativity of Ca (1.00) and Sr (0.95) is closer to the value of La (1.10). No matter how the coordination environment of O changes, the change of bond strength in Ca and Sr substituted structure will be similar to that in the pure system. The differences in the electronegativities of Mg (1.31) and Ba (0.89) from that of La are larger and the bond strength between La-O and Ba-O or Mg-O will vary m than in Ca and Sr case. Thus, the O vacancy formation energy will be more sensitive to the coordination environment and there is a wider range of formation energies. The configuration in Figure 5-15 (Red: oxygen; purple: manganese; dark smaller green: La; bright larger green: Ba.) also illustrates our points. We picked up two different oxygen positions in Ba substituted structure.

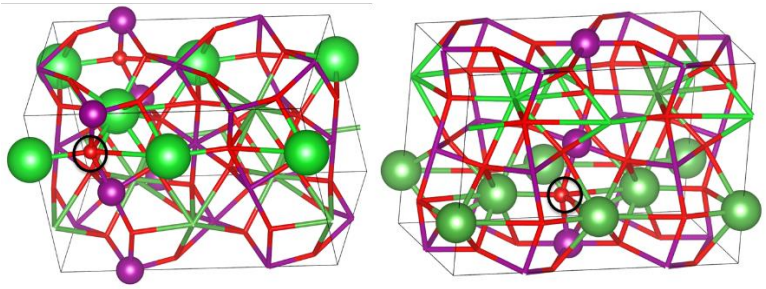

(a) (b)

Figure 5-15. Oxygen sites with different coordination environments in Ba substituted structure.

In Figure 5-15 (a), oxygen has 4 Ba and 2 Mn as its neighbors. In Figure 5-15 (b), oxygen has 4 La and 2 Mn as its neighbor. The electronegativity of Ba is much smaller than La which means the bond strength between Ba and O is much stronger than between La and O. The oxygen in Figure 5-15 (a) has 4 O-Ba bonds and 2 O-Mn bonds so that more energy is needed to create an oxygen vacancy. Indeed, the oxygen vacancy formation energy is only 2.45 eV for the configuration in Figure 5-15 (b) but is 3.24 eV for the configuration in Figure 5-15 (a). The size

of the dopants may also play a role in this part. Ca and Sr are slightly smaller and slightly larger than La; Mg and Ba are much smaller and much larger than the La. The larger the size difference between the dopants and La, the larger variance in oxygen vacancy formation energy is. This trend is the same as what we find in electronegativity. As a result, the electronegativity and size differences may act in concert to determine the variance in oxygen vacancy formation energy.

## 5.4 Conclusions

In this chapter, applying density functional theory calculations, we screened substituted $LaMnO_3$ for water splitting applications. Stability analysis and oxygen vacancy formation energy were considered as criteria to select candidates from all different substituted compounds. In determining the temperature and pressure range of stability, we applied thermodynamic analysis and the ideal gas law to predict the stable temperature range for all the compositions. In our analysis, Ca, Sr, and Ba A-site substitutions and Al Ga, In, and Mg B-site substitutions result in temperature stability up to ~2000 K; the compositions were therefore used for further analysis. In vacancy formation energy calculations, we find all of these compositions produce oxygen vacancy formation energy in 2.5-5.0 eV. We found that the value of oxygen vacancy formation energy is related to the coordination environments and the oxidation states of substituted elements. That is, the deviation of oxygen vacancy formation energy between different vacancy sites under the same substituted structure decreases as the decreasing of difference in electronegativity between La and other neighbors of oxygen. Also, the oxygen vacancy formation energy increases as the increasing of the valence of substituted elements. These interesting findings can be doping strategies for controlling the vacancy formation energy in perovskite materials in water splitting or other different applications.

# CHAPTER 6
# DOPED PYROCHLORE MATERIALS FOR WATER SPLITTING BY DENSITY FUNCTIONAL THEORY CALCULATIONS

## 6.1 Background

The appeal of the perovskites for water splitting applications, among others, is the wide range of compositions that are available and the ease of doping. However, perovskites are not the only class of materials that have this potential. We will thus extend our analysis to pyrochlore structures, $A_2B_2O_7$. Pyrochlore is a cubic structured phase with the structural formula $^{VIII}A_2{}^{VI}B_2{}^{IV}X_6{}^{IV}Y$ and space group Fd−3 m (No. 227), which is distinguished from fluorite ($AX_2$) by two unique cation sites and vacancies on one-eighth of the anion sites; both cations and anion vacancies adopt an ordered arrangement. A-site cations are eightfold coordinated and, as a consequence of the anion vacancies, the coordination of the B-site is reduced from eightfold to sixfold. The pyrochlore structure is chemically flexible and possesses the capacity to incorporate a wide range of elements. The likelihood of pyrochlore formation is affected by the ionic radii of the A- and B-site cations (typically $r_A$=0.087–0.151 nm and $r_B$=0.040–0.078 nm) and their ratio ($r_A/r_B$).[77] This class of materials is chosen as fertile ground for possible third generation candidate solar -thermal materials for several reasons: (i) the pyrochlores can be considered as defect-fluorite structures, resembling $CeO_{2-x}$; (ii) the pyrochlore structure has a vacant site that would be occupied by an oxygen atom in the fluorite structure. The presence of this vacant site can be expected to enhance oxygen diffusion; (iii) as ternary oxides, they have similar chemical diversity as the perovskites with the A site generally being a large 3+ ion and the B site being a smaller 4+ ion. The incorporation of multivalent atoms allows the tuning of the off-stoichiometry in a manner analogous to that in the perovskites. In this chapter, we will apply the same methodology as used in Chapter 5 to screen various pyrochlore compositions.

## 6.2 Methodology

### 6.2.1 Density Functional Theory (DFT) Calculations

We used the same DFT parameters as discussed in Section 5.2.1. However, the FERE values for lanthanides have only been determined for La and Ce. We have fitted the FERE value for them and will discuss them in detail in Section 6.3.1.

### 6.2.2 Pyrochlore Structure

Figure 6-1 ($Eu_2Ti_2O_7$ as an example; purple atoms: Eu; light blue atoms: Ti; red atoms: oxygen) shows the conventional unit cell of pyrochlore which contains 8 formula units and a total of 88 atoms. This relatively large unit cell means that it would be computational expensive. To save computational cost, we can use a Niggli-Reduced Cell of 22 atoms (two formula units) to do all the following calculations, as shown in Figure 6-2 (purple atoms: Eu; light blue atoms: Ti; red atoms: oxygen)

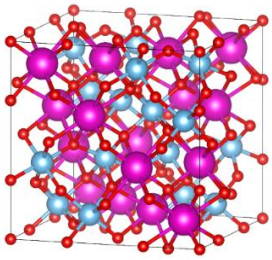

Figure 6-1. Pyrochlore conventional unit cell

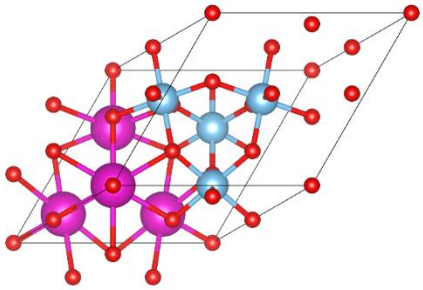

Figure 6-2. Pyrochlore Niggli-Reduced Cell.

We dope the various pyrochlore compositions with Li Na K Rb Mg Ca Sr Ba In on the A sites because it has been shown that the conductivity can be enhanced by doping on the A-site through doping and change was seen by altering the B-site.[78] This implies that only A sites substitution actually impacts oxygen vacancy diffusion. There are 4 A-sites in the primitive cell, but they are crystallographically identical. In our studies, we sill substitute one of these for A atoms, corresponding to 25% substitution.

### 6.2.3 Stability analysis

Unlike La and Ce, the FERE values for lanthanide elements such as Eu, Gd, Sm, and Nd are not available. Therefore, we need to first fit FERE values for these elements. In addition, the NREL database does not include compounds based on these lanthanides. To address this issue, we searched through the Materials Project database [51] to find the structure of all possible compounds based on these lanthanides. We used the same DFT settings as in the Materials Project to calculate their total energy per atom and performed a stability analysis.

### 6.2.4 Oxygen Vacancy Formation Energy Calculations

We consider all unique oxygen positions based on a substituted primitive cell. Oxygen vacancies are created on these sites, and we calculate the oxygen vacancy formation energy using the same criteria of 2.5-4.0 eV as in Chapter 5. We compare this value with the formation energy calculated for the primitive cell without any atom substitution to study the impact of dopants on oxygen vacancy formation energy.

## 6.3 Results and Discussion

### 6.3.1 FERE Fitting of Lanthanide Elements

The first step to fit the FERE value of lanthanides, taking Gd as an example, is to find all the common compounds based on the Gd and find their experimental enthalpies of formation. Assuming the FERE value for Gd is $\Delta\mu_{Gd}^{FERE}$ and taking $Gd_2O_3$ as an example, the error between

experimental enthalpy of formation and our calculated enthalpy of formation with $\Delta\mu_{Gd}^{FERE}$ can be expressed using equation 6-1:

$$\text{Error}=\Delta H^{exp}{}_{/atom}-[E_{DFT/atom}-\frac{(2\times\Delta\mu_{Gd}^{FERE}+3\times\Delta\mu_{O}^{FERE})}{5}] \quad (6\text{-}1)$$

$\Delta H^{exp}{}_{/atom}$ is the experimental enthalpy of formation per atom. $E_{DFT/atom}$ is the calculated DFT total energy per atom for the compound. $\Delta\mu_{Gd}^{FERE}$ is the FERE value for Gd. $\Delta\mu_{O}^{FERE}$ is the FERE value of oxygen which is already known as -4.76 eV. Our objective is to find a $\Delta\mu_{Gd}^{FERE}$ value that can minimize the root of mean square error (RMSE) across all the enthalpy of formation of common compound based on Gd. We found that the $\text{RMSE}_{\text{minimum}} = 0.032$ eV when $\Delta\mu_{\text{Gd}}^{\text{FERE}}$ = -13.00 eV. Table 6-1 shows the experimental enthalpy of formation and calculated value for all the common compound based on Gd. The difference (error) and RMSE between experimental data and calculated data are also listed.

Table 6-1. Experimental enthalpy of formation, calculated enthalpy of formation, the difference between experimental data and calculated data, RMSE for Gd-based compounds.

| System | Exp ΔH (eV) | ΔH calculated with fitted $\Delta\mu_{Gd}$ (eV) | Difference (eV) | RMSE (eV) |
|---|---|---|---|---|
| $Gd_2O_3$ | -3.7717 | -3.7958 | -0.024 | 0.031 |
| $GdCl_3$ | -2.6117 | -2.5618 | 0.050 | |
| GdAs | -1.6064 | -1.5817 | 0.025 | |
| GdOCl | -3.3821 | -3.4001 | -0.018 | |

With the same methodology, we can fit the FERE value for Nd, Eu and Sm. Table 6-2 to 6-4 shows the experimental enthalpy of formation and calculated value for all the common compound based on Nd, Eu and Sm, the difference (error) and RMSE between experimental data and calculated data. Table 6-5 shows the FERE value for these lanthanides.

Table 6-2. Experimental enthalpy of formation, calculated enthalpy of formation, the difference between experimental data and calculated data, RMSE for Nd-based compounds.

| System | Exp ΔH (eV) | ΔH calculated with fitted $\Delta\mu_{Nd}$ (eV) | Difference (eV) | RMSE (eV) |
|---|---|---|---|---|
| $Nd_2O_3$ | -3.7474 | -3.655 | -0.092 | 0.138 |
| $NdF_3$ | -4.2933 | -4.342 | -0.049 | |
| $NdCl_2$ | -2.3561 | -2.636 | -0.280 | |
| $NdCl_3$ | -2.6972 | -2.591 | 0.106 | |
| $Nd_2S_3$ | -2.4625 | -2.378 | 0.085 | |
| NdOCl | -3.4547 | -3.369 | 0.085 | |

Table 6-3. Experimental enthalpy of formation, calculated enthalpy of formation, the difference between experimental data and calculated data, RMSE for Eu-based compounds.

| System | Exp ΔH (eV) | ΔH calculated with fitted $\Delta\mu_{Eu}$ (eV) | Difference (eV) | RMSE (eV) |
|---|---|---|---|---|
| EuO | -3.068 | -3.339 | -0.271 | 0.210 |
| $Eu_2O_3$ | -3.446 | -3.182 | 0.264 | |
| $EuCl_2$ | -2.847 | -2.892 | -0.045 | |
| $EuCl_3$ | -2.425 | -2.242 | 0.184 | |

Table 6-4. Experimental enthalpy of formation, calculated enthalpy of formation, the difference between experimental data and calculated data, RMSE for Sm-based compounds.

| System | Exp ΔH (eV) | ΔH calculated with fitted $\Delta\mu_{Sm}$ (eV) | Difference (eV) | RMSE (eV) |
|---|---|---|---|---|
| $Sm_2O_3$ | -3.7787 | -3.8908 | -0.012 | 0.308 |
| $SmF_3$ | -4.6068 | -4.6733 | -0.004 | |
| SmAs | -1.5598 | -1.6977 | -0.013 | |
| SmOCl | -3.4270 | -3.4595 | 0.051 | |

Table 6-5. Fitted FERE values, $\Delta\mu^{FERE}$, for Gd Nd Eu and Sm

| Elements | Gd | Nd | Eu | Sm |
|---|---|---|---|---|
| FERE values (eV) | -13.00 | -6.59 | -8.80 | -3.55 |

### 6.3.2 Stability Analysis

We have screened all the pyrochlore compositions in Table 6-6. For $Eu_2Ti_2O_7$, due to charge balance concerns, we opted to substitute group III elements exclusively on the Eu sites. As the highest oxidation state for Ti is 4+, it limits our ability to substitute $Eu^{3+}$ ions with +1 and +2 oxidation states on the A-sites. Including such ions would result in an insufficient number of

positive charges to offset the overall negative charge. Considering that Al and Ga are too small to fit in the A-sites, our doping choice in this scenario is limited to In. For all other pyrochlore compositions, we substituted Li Na K Rb Mg Ca Sr Ba on the A sites. The temperature stability ranges of all the compositions are in Table 6-6. As discussed in Chapter 5, 70 meV error from GGA-PBE level of calculation is considered for each composition.

Table 6-6. Stability analysis of selected substituted pyrochlores in Kelvin.

| Structure: | Li | Na | K | Rb | Mg | Ca | Sr | Ba |
|---|---|---|---|---|---|---|---|---|
| $Eu_2Mo_2O_7$ | 250-2500 | 250-2500 | 250-2500 | 250-2500 | 250-2500 | 250-2500 | 250-2500 | 250-2500 |
| $Eu_2Mn_2O_7$ | 500-2500 | 250-2500 | 250-2500 | 250-2500 | 250-2500 | 500-2500 | 250-2500 | 500-2500 |
| $Ce_2Ti_2O_7$ | 500-2000 | 500-2000 | 500-2000 | 500-2000 | 500-2000 | 500-2000 | 500-2000 | 500-2000 |
| $Nd_2Mo_2O_7$ | 1000-1500 | 1000-1500 | >1750 | >2000 | >1750 | >1750 | 1000-1500 | >1750 |
| $Gd_2Mo_2O_7$ | >1750 | >1750 | >1750 | >1750 | >1750 | >1750 | 1250-1275 | >1750 |
| **Structure:** | **In** | | | | | | | |
| $Eu_2Ti_2O_7$ | 250-2000 | | | | | | | |

As in Chapter 5, the green shading in the diagram indicates compositions that are predicted to be stable within a favorable temperature range for water splitting application. The orange area indicates the predicted stable temperature range may be suitable for water splitting application. The red area, which includes a temperature range, suggests that the composition is predicted to be stable but not suitable for water splitting. Finally, the pure red area, without any temperature range, indicates that the composition is not predicted to be stable. In addition to those highlighted in green, the composition marked with orange background indicates that they have not been experimentally observed yet. Composition with red background indicates that it has been reported to be unstable experimentally [79]. The composition with green background indicates that they have been synthesized in the lab before [80].

### 6.3.3 Oxygen Vacancy Formation Energy Calculations

We screened oxygen vacancy formation energy for all the green and yellow marked compositions in Table 6-6. The results for oxygen vacancy formation energies are in Figure 6-3.

Blue dash line shows energy criteria 2.5-4.0 eV. Orange dash line shows oxygen vacancy formation energy in unsubstituted compounds. Notice that there are different scales in the various panels. As before, the 2.5 to 4.0 eV target range is delineated by the blue dashed lines; the orange dashed line is the oxygen formation energy in the pure system.

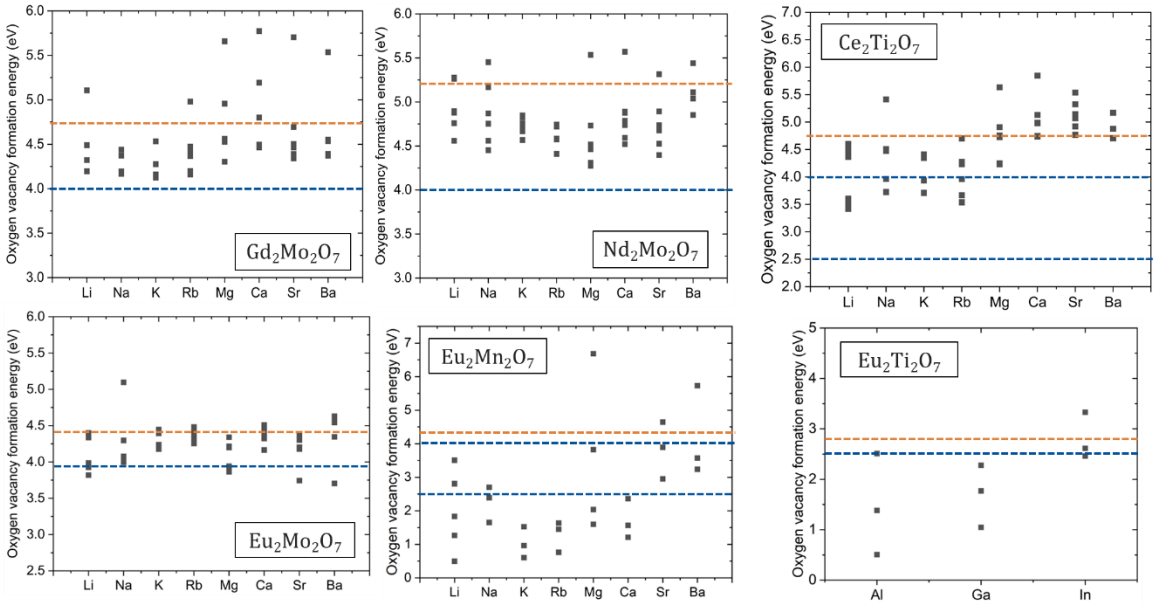


Figure 6-3. oxygen vacancy energy for selected pyrochlore compounds.

According to Figure 6-3, substituting atoms can reduce the vacancy formation energy relative to the pure system. The oxygen vacancy formation energy in $Nd_2Mo_2O_7$ is too high, making it difficult to generate oxygen vacancies during the water splitting reduction process. Although oxygen vacancy formation energy in $Gd_2Mo_2O_7$ and $Eu_2Mo_2O_7$ are above 4.0 eV. There are still many points very close to 4.0 eV which means we can still keep them as potential candidates. Regarding $Ce_2Ti_2O_7$, compositions with Li, Na, or K substitution appear to be good candidates. As for $Eu_2Mn_2O_7$, compositions with substitution of Li, Na, Mg, Sr, and Ba are potential candidates. In the case of $Eu_2Ti_2O_7$, although we have also calculated compositions with Al and Ga substitution, the sizes of Al and Ga are too small to fit in the A-sites, so we can

rule them out. Substitution with In results in an oxygen vacancy formation energy within the target range and can be considered as a candidate. Since $Eu_2Mo_2O_7$ have not been experimental observed and $Ce_2Ti_2O_7$ is reported to be unstable [79], we can propose $Eu_2Ti_2O_7$ and $Gd_2Mo_2O_7$ for experimental study [80].

## 6.4 Conclusion

In this chapter, we conducted a screening of stability and oxygen vacancy formation energy in several pyrochlore materials. We fitted the FERE value for Gd, Nd, Eu, and Sm and used these values for stability analysis. Based on the stability analysis, we identified six pyrochlore compositions and selected them for oxygen vacancy formation energy calculations. After the vacancy formation energy calculations, we determined that $Gd_2Mo_2O_7$ with Li, Na, or K substitution, and $Eu_2Ti_2O_7$ with In substitution are potential candidates for water splitting applications.

# CHAPTER 7
# SUMMARY AND CONCLUSIONS

This dissertation investigates several materials for new clean energy applications. First, DFT simulations are used to understand selectively $Cs^+$ ions sequestration by both non-hydrated and hydrated Cu-HCF. This helps us to have a solid understanding of why $Cs^+$ is favored by Cu-HCF against other alkali ions such as $K^+$ and $Na^+$, indicating a path for the use of HCF to sequester $Cs^+$ from nuclear waste. Second, DFT simulations are employed to identify substituted perovskite and pyrochlore materials suitable for water splitting applications. These simulations utilize stability and oxygen vacancy formation energy filters to assess the potential of different candidates. As a result, several promising materials are identified as contenders for water splitting applications.

In Chapter 3, The influence on Cu-HCF lattice distortion, energetics, structure stabilities and electronic structures caused by Cs+ incorporation has been characterized. From DFT calculations, there is much smaller lattice distortion caused by the $Cs^+$ in defected Cu-HCF compared to the other two alkali ions. Analysis of the alkali ion incorporation energy and ion exchange energy showed that $Cs^+$ incorporation is more thermodynamically favorable than $K^+$ and $Na^+$. It was also found that $Cs^+$ reinforces the Cu-HCF structures by strengthening the metal-ligand bond. The increased overlap area of transition metal and ligand peaks as the number of $Cs^+$ being incorporated increases was also indicative of $Cs^+$ incorporation strengthening the metal-ligand connection. This is verified by experiment. Further, the densities of states also reflect the change of the magnetic moment of transition metals resulting from the reduction process happening in transition metals. All the calculations demonstrate that $Cs^+$ incorporation in Cu-HCF is favorable compared to other alkali ions such as $K^+$ and $Na^+$. The intrinsic magnetic

properties of the empty Cu-HCF framework suggest that uniform and stable colloidal dispersions that can absorb more $Cs^+$ ions may be created by magnetic dispersion.

In Chapter 4, we have investigated the distribution of water molecules within the hydrated Cu-HCF framework and their impact on alkali ion incorporation energy and alkali ion exchange energy. Our theoretical calculations suggest that the maximum number of water molecules in the hydrated Cu-HCF is 18. Furthermore, we found that coordinated water is preferred when there is only one water molecule in the framework, whereas zeolitic water molecules are favored when there is more than one water molecule present. Coordinated water molecules will also form due to limited space for zeolitic water when the number of water molecules inside the framework is high. Our results also indicate that $K^+$ and $Cs^+$ ions tend to occupy the 8c sites, while $Na^+$ ions prefer the center of the framework after structural relaxation following alkali ion incorporation. Additionally, we found that water molecules decrease the alkali ion incorporation energy, making it more energetically favorable, and increase the ion exchange energy, making it less energetically favorable.

In Chapter 5, applying density functional theory calculations, we screened substituted $LaMnO_3$ for water splitting applications. Stability analysis and oxygen vacancy formation energy were considered as criteria to select candidates from all different substituted compounds. In our stability analysis, Ca, Sr, and Ba A-site substitutions and Al Ga, In, and Mg B-site substitutions result in temperature stability up to ~2000 K; the compositions were therefore used for further analysis. In vacancy formation energy calculations, we find all of these compositions produce oxygen vacancy formation energy in 2.5-5.0 eV. We found that the value of oxygen vacancy formation energy is related to the coordination environments and the oxidation states of substituted elements. That is, the deviation of oxygen vacancy formation energy between

different vacancy sites under the same substituted structure decreases as the decreasing of difference in electronegativity between La and other neighbors of oxygen. Also, the oxygen vacancy formation energy increases as the increasing of the valence of substituted elements. These interesting findings can be doping strategies for controlling the vacancy formation energy in perovskite materials in water splitting or other different applications.

In Chapter 6, we conducted a screening of stability and oxygen vacancy formation energy in several pyrochlore materials. We fitted the FERE value for Gd, Nd, Eu, and Sm and used these values for stability analysis. Based on the stability analysis, we identified six pyrochlore compositions and selected them for oxygen vacancy formation energy calculations. After the vacancy formation energy calculations, we determined that $Gd_2Mo_2O_7$ with Li, Na, or K substitution, and $Eu_2Ti_2O_7$ with In substitution are potential candidates for water splitting applications.

LIST OF REFERENCES


(1) Gawlik, L.; Mokrzycki, E. Paliwa Kopalne w Krajowej Energetyce-Problemy i Wyzwania. **2017**, 20–24.

(2) Alwaeli, M.; Mannheim, V. Investigation into the Current State of Nuclear Energy and Nuclear Waste Management—A State-of-the-Art Review. *Energies (Basel)* **2022**, *15* (12), 4275. https://doi.org/10.3390/en15124275.

(3) Chan, C. Radioactive Waste Management: An International Perspective. *International Atomic Energy Agency Bulletin* **1992**, *34:3*, 7–15.

(4) *Fukushima Daiichi: ANS Committee Report*.

(5) Tachikawa, H.; Haga, K.; Yamada, K. Mechanism of K + , Cs + Ion Exchange in Nickel Ferrocyanide: A Density Functional Theory Study. *Comput Theor Chem* **2017**, *1115*, 175–178. https://doi.org/10.1016/j.comptc.2017.06.009.

(6) Delchet, C.; Tokarev, A.; Dumail, X.; Toquer, G.; Barré, Y.; Guari, Y.; Guerin, C.; Larionova, J.; Grandjean, A. Extraction of Radioactive Cesium Using Innovative Functionalized Porous Materials. *RSC Adv* **2012**, *2* (13), 5707. https://doi.org/10.1039/c2ra00012a.

(7) Causse, J.; Tokarev, A.; Ravaux, J.; Moloney, M.; Barré, Y.; Grandjean, A. Facile One-Pot Synthesis of Copper Hexacyanoferrate Nanoparticle Functionalised Silica Monoliths for the Selective Entrapment of $^{137}$ Cs. *J. Mater. Chem. A* **2014**, *2* (25), 9461–9464. https://doi.org/10.1039/C4TA01266F.

(8) Tao, Q.; Zhang, X.; Huang, D.; Huang, G.; Fan, J.; Peng, H.; Dai, Y.; Prabaharan, K. Copper Hexacyanoferrate Nanoparticle-Decorated Biochar Produced from Pomelo Peel for Cesium Removal from Aqueous Solution. *J Radioanal Nucl Chem* **2019**, *322* (2), 791–799. https://doi.org/10.1007/s10967-019-06709-0.

(9) Didi, Y.; Said, B.; Micolle, M.; Cacciaguerra, T.; Cot, D.; Geneste, A.; Fajula, F.; Galarneau, A. Nanocrystals FAU-X Monoliths as Highly Efficient Microreactors for Cesium Capture in Continuous Flow. *Microporous and Mesoporous Materials* **2019**, *285*, 185–194. https://doi.org/10.1016/j.micromeso.2019.05.012.

(10) Sigfusson, T. I. Pathways to Hydrogen as an Energy Carrier. *Philosophical Transactions of the Royal Society A: Mathematical, Physical and Engineering Sciences* **2007**, *365* (1853), 1025–1042. https://doi.org/10.1098/rsta.2006.1960.

(11) Cho, H.-S.; Kodama, T.; Gokon, N.; Bellan, S.; Kim, J.-K. Development of Synthesis and Fabrication Process for Mn-CeO2 Foam via Two-Step Water-Splitting Cycle Hydrogen Production. *Energies (Basel)* **2021**, *14* (21), 6919. https://doi.org/10.3390/en14216919.

(12) Takacs, M.; Hoes, M.; Caduff, M.; Cooper, T.; Scheffe, J. R.; Steinfeld, A. Oxygen Nonstoichiometry, Defect Equilibria, and Thermodynamic Characterization of LaMnO3 Perovskites with Ca/Sr A-Site and Al B-Site Doping. *Acta Mater* **2016**, *103*, 700–710. https://doi.org/10.1016/j.actamat.2015.10.026.

(13) Scheffe, J. R.; Steinfeld, A. Oxygen Exchange Materials for Solar Thermochemical Splitting of H2O and CO2: A Review. *Materials Today* **2014**, *17* (7), 341–348. https://doi.org/10.1016/j.mattod.2014.04.025.

(14) Scheffe, J. R.; Weibel, D.; Steinfeld, A. Lanthanum–Strontium–Manganese Perovskites as Redox Materials for Solar Thermochemical Splitting of $H_2O$ and $CO_2$. *Energy & Fuels* **2013**, *27* (8), 4250–4257. https://doi.org/10.1021/ef301923h.

(15) Scheffe, J. R.; Jacot, R.; Patzke, G. R.; Steinfeld, A. Synthesis, Characterization, and Thermochemical Redox Performance of $Hf^{4+}$, $Zr^{4+}$, and $Sc^{3+}$ Doped Ceria for Splitting $CO_2$. *The Journal of Physical Chemistry C* **2013**, *117* (46), 24104–24114. https://doi.org/10.1021/jp4050572.

(16) Louie, S. G.; Chan, Y.-H.; da Jornada, F. H.; Li, Z.; Qiu, D. Y. Discovering and Understanding Materials through Computation. *Nat Mater* **2021**, *20* (6), 728–735. https://doi.org/10.1038/s41563-021-01015-1.

(17) Hohenberg, P.; Kohn, W. Inhomogeneous Electron Gas. *Physical Review* **1964**, *136* (3B), B864–B871. https://doi.org/10.1103/PhysRev.136.B864.

(18) Kresse, G.; Hafner, J. *Ab Initio* Molecular Dynamics for Liquid Metals. *Phys Rev B* **1993**, *47* (1), 558–561. https://doi.org/10.1103/PhysRevB.47.558.

(19) Kresse, G.; Furthmüller, J. Efficiency of Ab-Initio Total Energy Calculations for Metals and Semiconductors Using a Plane-Wave Basis Set. *Comput Mater Sci* **1996**, *6* (1), 15–50. https://doi.org/10.1016/0927-0256(96)00008-0.

(20) Lany, S. Semiconductor Thermochemistry in Density Functional Calculations. *Phys Rev B* **2008**, *78* (24), 245207. https://doi.org/10.1103/PhysRevB.78.245207.

(21) Chevrier, V. L.; Ong, S. P.; Armiento, R.; Chan, M. K. Y.; Ceder, G. Hybrid Density Functional Calculations of Redox Potentials and Formation Energies of Transition Metal Compounds. *Phys Rev B* **2010**, *82* (7), 075122. https://doi.org/10.1103/PhysRevB.82.075122.

(22) Stevanović, V.; Lany, S.; Zhang, X.; Zunger, A. Correcting Density Functional Theory for Accurate Predictions of Compound Enthalpies of Formation: Fitted Elemental-Phase Reference Energies. *Phys Rev B* **2012**, *85* (11), 115104. https://doi.org/10.1103/PhysRevB.85.115104.

(23) Goyal, A.; Gorai, P.; Peng, H.; Lany, S.; Stevanović, V. A Computational Framework for Automation of Point Defect Calculations. *Comput Mater Sci* **2017**, *130*, 1–9. https://doi.org/10.1016/j.commatsci.2016.12.040.

(24) Chen, L.-H.; Li, Y.; Su, B.-L. Hierarchy in Materials for Maximized Efficiency. *Natl Sci Rev* **2020**, *7* (11), 1626–1630. https://doi.org/10.1093/nsr/nwaa251.

(25) zur Loye, H.-C.; Besmann, T.; Amoroso, J.; Brinkman, K.; Grandjean, A.; Henager, C. H.; Hu, S.; Misture, S. T.; Phillpot, S. R.; Shustova, N. B.; Wang, H.; Koch, R. J.; Morrison, G.; Dolgopolova, E. Hierarchical Materials as Tailored Nuclear Waste Forms: A Perspective. *Chemistry of Materials* **2018**, *30* (14), 4475–4488. https://doi.org/10.1021/acs.chemmater.8b00766.

(26) Sangvanich, T.; Sukwarotwat, V.; Wiacek, R. J.; Grudzien, R. M.; Fryxell, G. E.; Addleman, R. S.; Timchalk, C.; Yantasee, W. Selective Capture of Cesium and Thallium from Natural Waters and Simulated Wastes with Copper Ferrocyanide Functionalized Mesoporous Silica. *J Hazard Mater* **2010**, *182* (1–3), 225–231. https://doi.org/10.1016/j.jhazmat.2010.06.019.

(27) Loos-Neskovic, C.; Ayrault, S.; Badillo, V.; Jimenez, B.; Garnier, E.; Fedoroff, M.; Jones, D. J.; Merinov, B. Structure of Copper-Potassium Hexacyanoferrate (II) and Sorption Mechanisms of Cesium. *J Solid State Chem* **2004**, *177* (6), 1817–1828. https://doi.org/10.1016/j.jssc.2004.01.018.

(28) Ayers, J. B.; Waggoner, W. H. Synthesis and Properties of Two Series of Heavy Metal Hexacyanoferrates. *Journal of Inorganic and Nuclear Chemistry* **1971**, *33* (3), 721–733. https://doi.org/10.1016/0022-1902(71)80470-0.

(29) Ismail, I. M.; El-Sourougy, M. R.; Moneim, N. A.; Aly, H. F. Preparation, Characterization, and Utilization of Potassium Nickel Hexacyanoferrate for the Separation of Cesium and Cobalt from Contaminated Waste Water. *J Radioanal Nucl Chem* **1998**, *237* (1–2), 97–103. https://doi.org/10.1007/BF02386669.

(30) Szöke, S.; Pátzay, G.; Weiser, L. Development of Selective Cobalt and Cesium Removal from the Evaporator Concentrates of the PWR Paks. *Radiochim Acta* **2003**, *91* (4), 229–232. https://doi.org/10.1524/ract.91.4.229.19973.

(31) Chen, R.; Tanaka, H.; Kawamoto, T.; Asai, M.; Fukushima, C.; Kurihara, M.; Ishizaki, M.; Watanabe, M.; Arisaka, M.; Nankawa, T. Thermodynamics and Mechanism Studies on Electrochemical Removal of Cesium Ions from Aqueous Solution Using a Nanoparticle Film of Copper Hexacyanoferrate. *ACS Appl Mater Interfaces* **2013**, *5* (24), 12984–12990. https://doi.org/10.1021/am403748b.

(32) Chen, R.; Tanaka, H.; Kawamoto, T.; Asai, M.; Fukushima, C.; Na, H.; Kurihara, M.; Watanabe, M.; Arisaka, M.; Nankawa, T. Selective Removal of Cesium Ions from Wastewater Using Copper Hexacyanoferrate Nanofilms in an Electrochemical System. *Electrochim Acta* **2013**, *87*, 119–125. https://doi.org/10.1016/j.electacta.2012.08.124.

(33) Nilchi, A.; Saberi, R.; Moradi, M.; Azizpour, H.; Zarghami, R. Adsorption of Cesium on Copper Hexacyanoferrate–PAN Composite Ion Exchanger from Aqueous Solution. *Chemical Engineering Journal* **2011**, *172* (1), 572–580. https://doi.org/10.1016/j.cej.2011.06.011.

(34) Chen, R.; Tanaka, H.; Kawamoto, T.; Asai, M.; Fukushima, C.; Kurihara, M.; Watanabe, M.; Arisaka, M.; Nankawa, T. Preparation of a Film of Copper Hexacyanoferrate Nanoparticles for Electrochemical Removal of Cesium from Radioactive Wastewater. *Electrochem commun* **2012**, *25*, 23–25. https://doi.org/10.1016/j.elecom.2012.09.012.

(35) Ganzerli Valentini, M. T.; Stella, R.; Maggi, L.; Ciceri, G. Copper Hexacyanoferate(II) and (III) as Trace Cesium Adsorbers from Natural Waters. *Journal of Radioanalytical and Nuclear Chemistry Articles* **1987**, *114* (1), 105–112. https://doi.org/10.1007/BF02048881.

(36) Milonji, S.; Bispo, I.; Fedoroff, M.; Loos-Neskovic, C.; Vidal-Madjar, C. Sorption of Cesium on Copper Hexacyanoferrate/Polymer/Silica Composites in Batch and Dynamic Conditions. *J Radioanal Nucl Chem* **2002**, *252* (3), 497–501. https://doi.org/10.1023/A:1015846502676.

(37) Wojdeł, J. C.; Moreira, I. de P. R.; Bromley, S. T.; Illas, F. Prediction of Half-Metallic Conductivity in Prussian Blue Derivatives. *J Mater Chem* **2009**, *19* (14), 2032. https://doi.org/10.1039/b813788a.

(38) Wang, B.; Han, Y.; Wang, X.; Bahlawane, N.; Pan, H.; Yan, M.; Jiang, Y. Prussian Blue Analogs for Rechargeable Batteries. *iScience* **2018**, *3*, 110–133. https://doi.org/10.1016/j.isci.2018.04.008.

(39) Ma, F.; Li, Q.; Wang, T.; Zhang, H.; Wu, G. Energy Storage Materials Derived from Prussian Blue Analogues. *Sci Bull (Beijing)* **2017**, *62* (5), 358–368. https://doi.org/10.1016/j.scib.2017.01.030.

(40) Xu, Y.; Zheng, S.; Tang, H.; Guo, X.; Xue, H.; Pang, H. Prussian Blue and Its Derivatives as Electrode Materials for Electrochemical Energy Storage. *Energy Storage Mater* **2017**, *9*, 11–30. https://doi.org/10.1016/j.ensm.2017.06.002.

(41) Kresse, G.; Joubert, D. From Ultrasoft Pseudopotentials to the Projector Augmented-Wave Method. *Phys Rev B* **1999**, *59* (3), 1758–1775. https://doi.org/10.1103/PhysRevB.59.1758.

(42) Blöchl, P. E. Projector Augmented-Wave Method. *Phys Rev B* **1994**, *50* (24), 17953–17979. https://doi.org/10.1103/PhysRevB.50.17953.

(43) Itaya, K.; Uchida, I.; Neff, V. D. Electrochemistry of Polynuclear Transition Metal Cyanides: Prussian Blue and Its Analogues. *Acc Chem Res* **1986**, *19* (6), 162–168. https://doi.org/10.1021/ar00126a001.

(44) Targholi, E.; Mousavi-Khoshdel, S. M.; Rahmanifara, M.; Yahya, M. Z. A. Cu- and Fe-Hexacyanoferrate as Cathode Materials for Potassium Ion Battery: A First-Principles Study. *Chem Phys Lett* **2017**, *687*, 244–249. https://doi.org/10.1016/j.cplett.2017.09.029.

(45) Mähler, J.; Persson, I. A Study of the Hydration of the Alkali Metal Ions in Aqueous Solution. *Inorg Chem* **2012**, *51* (1), 425–438. https://doi.org/10.1021/ic2018693.

(46) Pandey, S.; Jia, Z.; Demaske, B.; Ejegbavwo, O. A.; Setyawan, W.; Henager, C. H.; Shustova, N.; Phillpot, S. R. Sequestration of Radionuclides in Metal–Organic Frameworks from Density Functional Theory Calculations. *The Journal of Physical Chemistry C* **2019**, *123* (44), 26842–26855. https://doi.org/10.1021/acs.jpcc.9b08256.

(47) Jiang, P.; Shao, H.; Chen, L.; Feng, J.; Liu, Z. Ion-Selective Copper Hexacyanoferrate with an Open-Framework Structure Enables High-Voltage Aqueous Mixed-Ion Batteries. *J Mater Chem A Mater* **2017**, *5* (32), 16740–16747. https://doi.org/10.1039/C7TA04172A.

(48) *atomic radius*. https://www.ausetute.com.au/trendar.html (accessed 2023-04-27).

(49) Ling, C.; Chen, J.; Mizuno, F. First-Principles Study of Alkali and Alkaline Earth Ion Intercalation in Iron Hexacyanoferrate: The Important Role of Ionic Radius. *The Journal of Physical Chemistry C* **2013**, *117* (41), 21158–21165. https://doi.org/10.1021/jp4078689.

(50) Wessells, C. D.; Huggins, R. A.; Cui, Y. Copper Hexacyanoferrate Battery Electrodes with Long Cycle Life and High Power. *Nat Commun* **2011**, *2* (1), 550. https://doi.org/10.1038/ncomms1563.

(51) *materials project*. https:// materialsproject.org/materials/mp-601952 (accessed 2023-04-27).

(52) Åkerblom, I. E.; Ojwang, D. O.; Grins, J.; Svensson, G. A Thermogravimetric Study of Thermal Dehydration of Copper Hexacyanoferrate by Means of Model-Free Kinetic Analysis. *J Therm Anal Calorim* **2017**, *129* (2), 721–731. https://doi.org/10.1007/s10973-017-6280-x.

(53) Adak, S.; Daemen, L. L.; Hartl, M.; Williams, D.; Summerhill, J.; Nakotte, H. Thermal Expansion in 3d-Metal Prussian Blue Analogs—A Survey Study. *J Solid State Chem* **2011**, *184* (11), 2854–2861. https://doi.org/10.1016/j.jssc.2011.08.030.

(54) Moloney, M. P.; Massoni, N.; Grandjean, A. Tuning the Thermal Stability of Copper(II) Hexacyanoferrate(II) Nanoparticles. *J Therm Anal Calorim* **2021**, *145* (5), 2353–2362. https://doi.org/10.1007/s10973-020-09823-4.

(55) Moloney, M. P.; Cabaud, C.; Massoni, N.; Stafford, S.; Gun'ko, Y. K.; Venkatesan, M.; Grandjean, A. Searching for the Nano Effect in Cu-HCF (II) Particles to Improve Cs Sorption Efficiency: Highlighting the Use of Intrinsic Magnetism. *Colloids Surf A Physicochem Eng Asp* **2019**, *582*, 123758. https://doi.org/10.1016/j.colsurfa.2019.123758.

(56) Avila, M.; Reguera, L.; Rodríguez-Hernández, J.; Balmaseda, J.; Reguera, E. Porous Framework of T2[Fe(CN)6]·xH2O with T=Co, Ni, Cu, Zn, and H2 Storage. *J Solid State Chem* **2008**, *181* (11), 2899–2907. https://doi.org/10.1016/j.jssc.2008.07.030.

(57) Mink, J.; Stirling, A.; Ojwang, D. O.; Svensson, G.; Mihály, J.; Németh, C.; Drees, M.; Hajba, L. Vibrational Properties and Bonding Analysis of Copper Hexacyanoferrate Complexes in Solid State. *Appl Spectrosc Rev* **2019**, *54* (5), 369–424. https://doi.org/10.1080/05704928.2018.1459659.

(58) Xu, Y.; Wan, J.; Huang, L.; Xu, J.; Ou, M.; Liu, Y.; Sun, X.; Li, S.; Fang, C.; Li, Q.; Han, J.; Huang, Y.; Zhao, Y. Dual Redox-Active Copper Hexacyanoferrate Nanosheets as Cathode Materials for Advanced Sodium-Ion Batteries. *Energy Storage Mater* **2020**, *33*, 432–441. https://doi.org/10.1016/j.ensm.2020.08.008.

(59) Cattermull, J.; Sada, K.; Hurlbutt, K.; Cassidy, S. J.; Pasta, M.; Goodwin, A. L. *Revealing the Structural Complexity of Prussian Blue Analogues: The Case of K 2 Cu[Fe(CN) 6 ]*.

(60) Ojwang, D. O.; Grins, J.; Wardecki, D.; Valvo, M.; Renman, V.; Häggström, L.; Ericsson, T.; Gustafsson, T.; Mahmoud, A.; Hermann, R. P.; Svensson, G. Structure Characterization and Properties of K-Containing Copper Hexacyanoferrate. *Inorg Chem* **2016**, *55* (12), 5924–5934. https://doi.org/10.1021/acs.inorgchem.6b00227.

(61) Richard J. D. Tilley. *Perovskites: Structure-Property Relationships*.

(62) Muhich, C. L.; Ehrhart, B. D.; Al-Shankiti, I.; Ward, B. J.; Musgrave, C. B.; Weimer, A. W. A Review and Perspective of Efficient Hydrogen Generation via Solar Thermal Water Splitting. *Wiley Interdiscip Rev Energy Environ* **2016**, *5* (3), 261–287. https://doi.org/10.1002/wene.174.

(63) Emery, A. A.; Saal, J. E.; Kirklin, S.; Hegde, V. I.; Wolverton, C. High-Throughput Computational Screening of Perovskites for Thermochemical Water Splitting Applications. *Chemistry of Materials* **2016**, *28* (16), 5621–5634. https://doi.org/10.1021/acs.chemmater.6b01182.

(64) Sai Gautam, G.; Stechel, E. B.; Carter, E. A. Exploring Ca–Ce–M–O (M = 3d Transition Metal) Oxide Perovskites for Solar Thermochemical Applications. *Chemistry of Materials* **2020**, *32* (23), 9964–9982. https://doi.org/10.1021/acs.chemmater.0c02912.

(65) Şanlı, S. B.; Pişkin, B. Effect of B-Site Al Substitution on Hydrogen Production of La0.4Sr0.6Mn1-XAlx (X=0.4, 0.5 and 0.6) Perovskite Oxides. *Int J Hydrogen Energy* **2022**, *47* (45), 19411–19421. https://doi.org/10.1016/j.ijhydene.2021.12.047.

(66) Dudarev, S. L.; Botton, G. A.; Savrasov, S. Y.; Humphreys, C. J.; Sutton, A. P. Electron-Energy-Loss Spectra and the Structural Stability of Nickel Oxide: An LSDA+U Study. *Phys Rev B* **1998**, *57* (3), 1505–1509. https://doi.org/10.1103/PhysRevB.57.1505.

(67) Monkhorst, H. J.; Pack, J. D. Special Points for Brillouin-Zone Integrations. *Phys Rev B* **1976**, *13* (12), 5188–5192. https://doi.org/10.1103/PhysRevB.13.5188.

(68) *Handbook of Chemistry and Physics: A Ready-Reference Book of Chemical and Physical Data*.

(69) Osorio-Guillén, J.; Lany, S.; Barabash, S. V.; Zunger, A. Magnetism without Magnetic Ions: Percolation, Exchange, and Formation Energies of Magnetism-Promoting Intrinsic Defects in CaO. *Phys Rev Lett* **2006**, *96* (10), 107203. https://doi.org/10.1103/PhysRevLett.96.107203.

(70) Transactions and Communications. *Journal of the Society of Chemical Industry* **1944**, *63* (5), 125–160. https://doi.org/10.1002/jctb.5000630501.

(71) Piskunov, S.; Heifets, E.; Jacob, T.; Kotomin, E. A.; Ellis, D. E.; Spohr, E. Electronic structure and thermodynamic stability of LaMnO3 and $La_{1-x}Sr_xMnO_3$ (001) surfaces: Ab initio calculations. *Phys Rev B* **2008**, *78* (12), 121406. https://doi.org/10.1103/PhysRevB.78.121406.

(72) Demont, A.; Abanades, S. Solar Thermochemical Conversion of $CO_2$ into Fuel via Two-Step Redox Cycling of Non-Stoichiometric Mn-Containing Perovskite Oxides. *J Mater Chem A Mater* **2015**, *3* (7), 3536–3546. https://doi.org/10.1039/C4TA06655C.

(73) Wang, L.; Al-Mamun, M.; Zhong, Y. L.; Jiang, L.; Liu, P.; Wang, Y.; Yang, H. G.; Zhao, H. $Ca^{2+}$ and $Ga^{3+}$ Doped $LaMnO_3$ Perovskite as a Highly Efficient and Stable Catalyst for Two-Step Thermochemical Water Splitting. *Sustain Energy Fuels* **2017**, *1* (5), 1013–1017. https://doi.org/10.1039/C6SE00097E.

(74) Yang, L.; Hu, J.; Tian, G.; Zhu, J.; Song, Q.; Wang, H.; Zhang, C. Efficient Catalysts of K and Ce Co-Doped $LaMnO_3$ for $NO_x$–Soot Simultaneous Removal and Reaction Kinetics. *ACS Omega* **2021**, *6* (30), 19836–19845. https://doi.org/10.1021/acsomega.1c02565.

(75) Jiang, S.; Ding, W.; Zhao, K.; Huang, Z.; Wei, G.; Feng, Y.; Lv, Y.; He, F. Enhanced Chemical Looping Oxidative Coupling of Methane by Na-Doped LaMnO3 Redox Catalysts. *Fuel* **2021**, *299*, 120932. https://doi.org/10.1016/j.fuel.2021.120932.

(76) Bartel, C. J.; Weimer, A. W.; Lany, S.; Musgrave, C. B.; Holder, A. M. The Role of Decomposition Reactions in Assessing First-Principles Predictions of Solid Stability. *NPJ Comput Mater* **2019**, *5* (1), 4. https://doi.org/10.1038/s41524-018-0143-2.

(77) Sun, S.-K.; Bailey, D. J.; Gardner, L. J.; Hyatt, N. C. Ceramic-Based Stabilization/Solidification of Radioactive Waste. In *Low Carbon Stabilization and Solidification of Hazardous Wastes*; Elsevier, 2022; pp 449–468. https://doi.org/10.1016/B978-0-12-824004-5.00021-9.

(78) Anokhina, I. A.; Animitsa, I. E.; Voronin, V. I.; Vykhodets, V. B.; Kurennykh, T. E.; Molchanova, N. G.; Vylkov, A. I.; Dedyukhin, A. E.; Zaikov, Y. P. The Structure and Electrical Properties of Lithium Doped Pyrochlore Gd2Zr2O7. *Ceram Int* **2021**, *47* (2), 1949–1961. https://doi.org/10.1016/j.ceramint.2020.09.025.

(79) Hulbert, B. S.; McCormack, S. J.; Tseng, K.-P.; Kriven, W. M. Thermal Expansion and Phase Transformation in the Rare Earth Di-Titanate ( $R_2Ti_2O_7$ ) System. *Acta Crystallogr B Struct Sci Cryst Eng Mater* **2021**, *77* (3), 397–407. https://doi.org/10.1107/S2052520621004479.

(80) Moritomo, Y.; Xu, Sh.; Machida, A.; Katsufuji, T.; Nishibori, E.; Takata, M.; Sakata, M.; Cheong, S.-W. Chemical Pressure Control of Exchange Interaction in Mo Pyrochlore. *Phys Rev B* **2001**, *63* (14), 144425. https://doi.org/10.1103/PhysRevB.63.144425.

# BIOGRAPHICAL SKETCH

Ximeng Wang was born in Luoyang, Henan Province and grown up in Xiamen Fujian province, China. He received his Bachelor of Science degree in functional materials from Dalian University of Technology, Dalian in 2017. He selected modeling the defects formation on grain boundaries in copper by structural unit model as the topic of his Bachelor of Science degree thesis in that spring, where he was introduced to computational materials science. He joined the Department of Materials Science and Engineering at University of Florida, in August 2017 and began his Ph.D. under supervision of Prof. Simon R. Phillpot in January 2019. He received a Master of Science degree in materials science and engineering in May 2019. He primarily worked on DOE project for identifying perovskite and pyrochlore materials for water splitting application and Energy Frontier Research Center (EFRC) project for understanding sequestration of Cs by Cu-HCF frameworks in his doctoral research. In August 2023, he graduated from UF with a Ph.D. in materials science and engineering. In his free time, Ximeng enjoys photography, playing the piano and playing badminton.